Mesoscopic transport in 2D materials and heterostructures

Papadopoulos, Nikos

DOI

[10.4233/uuid:216d5572-d287-4aa7-8b9c-37c211e6ed98](#)

Publication date

2019

Document Version

Final published version

Citation (APA)

Important note

To cite this publication, please use the final published version (if applicable).
Please check the document version above.

MESOSCOPIC TRANSPORT IN 2D MATERIALS AND HETEROSTRUCTURES

MESOSCOPIC TRANSPORT IN 2D MATERIALS AND HETEROSTRUCTURES

Dissertation

for the purpose of obtaining the degree of doctor at Delft University of Technology by the authority of the Rector Magnificus Prof. Dr. Ir. T. H. J. J. van der Hagen, Chair of the Board for Doctorates, to be defended publicly on Monday 15 July 2019 at 12:30 o'clock

by

Nikos PAPADOPOULOS

Master of Science in Materials Physics and Technology,
Aristotle university, Thessaloniki, Greece,
born in Thessaloniki, Greece.

The dissertation has been approved by

promotor: prof. dr. G. A. Steele
promotor: prof. dr. H. S. J. van der Zant

Composition of the doctoral committee:

Rector Magnificus,	Chairman
Prof. dr. G. A. Steele,	Technische Universiteit Delft
Prof. dr. H. S. J. van der Zant,	Technische Universiteit Delft

Independent committee:

Prof. dr. M. A. Morgenstern,	RWTH Aachen University
Prof. dr. P. G. Steeneken	Technische Universiteit Delft
Prof. dr. J. Ye	University of Groningen
Prof. dr. F. Grozema	Technische Universiteit Delft
Dr. R. Frisenda	Instituto de Ciencia de Materiales de Madrid

An electronic version of this dissertation is available at
http://repository.tudelft.nl/.

To my teachers in science and in life.

CONTENTS

SUMMARY

This thesis presents an experimental work on electronic transport in two-dimensional (2D) van der Waals systems. The variety of the physics of the chapters reflects the exploratory character of the Ph.D. study and demonstrates the versatility and the unique properties of some of the members of the vast group of van der Waals materials. In the experiments we explore the fundamental properties of carriers and states in 2D materials via electrical transport.

The first three chapters include experimental work on planar transport in multi-terminal devices from transition metal dichalcogenides (2H-MoS_2) and trichalogenides (TiS_3). In the fist chapter, we study how intravalley spin relaxation and the phase coherence affects weak localization in boron nitride encapsulated MoS_2. In TiS_3 we explore its electronic properties and in order to avoid disorder induced localization, we protect the devices with hexagonal boron nitride. An improvement in the quality of the transport and signatures of charge-density-wave transition are observed. Lastly, multi-terminal transport in 1T/1T′-MoS_2 and its carrier transport mechanism are investigated, with special emphasis on how to establish low-temperature electrical contacts to 2H-MoS_2.

The next part of the thesis shifts to vertical transport in van der Waals heterostructures. Firstly, we use WS_2 as tunneling barrier between monolayer graphene and metal contact. We observe sequential tunneling through localized states. By studying the ground and excited states, we gain information about their spatial sizes and the magnetic moments of these states. Lastly, we explore heterostructures of graphene on WSe_2 and potential effects on the band structure due to the dielectric environment and the proximity induced spin-orbit coupling.

SAMENVATTING

Dit proefschrift presenteert een experimenteel onderzoek naar elektronen transport in tweedimensionale (2D) van der Waals-systemen. De verscheidenheid van de fysica van de hoofdstukken weerspiegelt het verkennende karakter van mijn promotie onderzoek en demonstreren de veelzijdigheid en de unieke eigenschappen van enkele leden van de grote groep van van der Waals materialen. In de experimenten verkennen we de fundamentele eigenschappen van ladingsdragers en elektronische toestanden in 2D-materialen via elektronen transport.

De eerste drie hoofdstukken bevatten experimenteel werk in vlak transport in multi-terminal apparaten van overgangsmetaal dichalcogenide (2H-MoS_2) en trichalogenide (TiS_3). In het eerste hoofdstuk bestuderen we hoe intravalley spin-relaxatie en de fase-coherentie in met boornitride ingekapselde MoS_2 structuren de zwakke lokalisatie beïn-vloeden. We verkennende elektronische eigenschappen van TiS_3 en om lokalisatie door wanorde te vermijden, beschermen we deze structuren met hexagonaal boornitride. We zien een verbetering in de kwaliteit van het transport en de kenmerken van een ladingsdichtheidsgolf-overgang. Ten slotte voeren we multi-terminal transport metingen uit in 1T/1T′-MoS_2 en onderzoeken we het onderliggende transport mechanisme van de ladingsdragers met nadruk op het realiseren van lage temperatuur geschikte elektrische aansluitingen met 2H-Mo_2.

Het volgende deel van het proefschrift verschuift naar verticaal transport in van der Waals heterostructuren. Ten eerste gebruiken we WS_2 als tunnelingbarrière tussen een monolaag grafeen en een metaalcontact. We observeren opeenvolgende tunneling door gelokaliseerde toestanden. Door de grond en aangeslagen toestanden te bestuderen, krijgen we informatie over hun ruimtelijke afmetingen en de magnetische momenten van deze toestanden. Ten slotte verkennen we heterostructuren van grafeen op WSe_2 en potentiële effecten op de elektronische bandstructuur als gevolg van de diëlektrische omgeving en de door nabijheid geïnduceerde spin-baankoppeling.

1

INTRODUCTION

1.1. A BRIEF HISTORICAL OVERVIEW OF TWO-DIMENSIONAL MATERIALS

No one could expect that the discovery of graphene in 2004 [1] would provide so much playground for physicists, chemist and even artists. Although there were many attempts to isolate individual layers of van der Waals materials during the 1980s via intercalation techniques [2], in the beginning of the new century A. Geim's and P. Kim's group from Manchester and Columbia university, respectively, worked towards thinning down layers of graphite. While P. Kim's group relied on thinning down graphite via scribing an AFM-based (atomic force microscopy) tip of graphite (nanopencil), the group of Manchester succeeded in obtaining thinner flakes by using a simpler method, based on scotch tape cleavage. The sticky tape method is commonly used by physicists for the preparation of surfaces of HOPG (highly oriented pyrolytic graphite) for calibration of scanning tunneling microscopy systems [3].

The explosion of research related to graphene took place after the Nobel price award to K. Novoselov and A. Geim. As a result of the unique properties of graphene which include relativistic Dirac dispersion, pseudospin due to sublattice symmetry, Berry phase of π, Klein tunneling, large Young's modulus, universal optical absorption and many more, the rate of publications was enormous [4]. Until recently companies like IBM and Samsung were investigating intensively properties of graphene devices, as well as large scale growth for transistors in processors. Nevertheless, the low ON/OFF ratio of transistors as a result of the lack of a considerable bandgap in graphene, terminated dreams of replacing silicon with graphene in processors. Nowadays, graphene is a promising candidate for interconnects due to the large electrical and thermal conductivity [5].

We should mention that already in 2005 other van der Waals crystals had been exfoliated and devices were fabricated with these new members of the 2D family [6]. A few years later the first two-dimensional transistor (n-type) based on MoS_2 was fabricated [7]. Although the electron mobilities were low, the ON/OFF ratio was far larger due to the band gap of ~2 eV. The properties of 2D semiconductors make them promising for

1
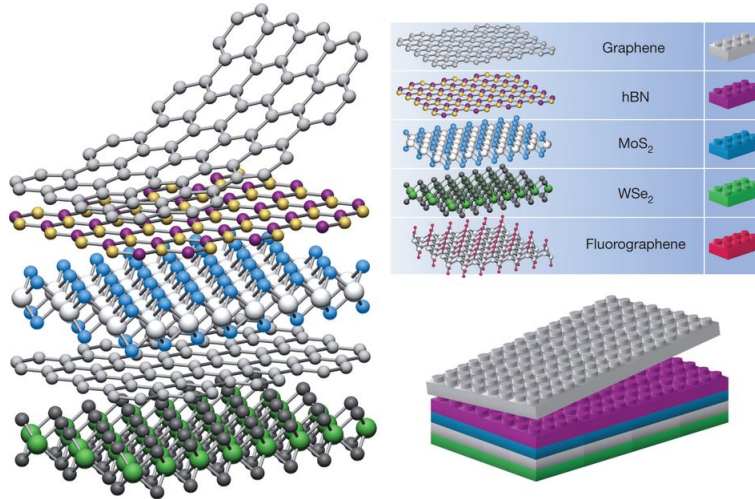
Figure 1.1: Heterostructures based on van der Waals materials. Layers of different van der Waals materials (graphene, h-BN, WSe$_2$ etc.) can be stacked together like Lego bricks to form artificial materials. Unlike conventional covalent-bonded materials that require molecular beam epitaxy (MBE) to form heterostructures, van der Waals heterostructures do not require such tools as they can be formed mechanically. Adapted from [9].

continuing scaling of transistors' dimensions and the proven end of Moore's law [8]. Nevertheless, disorder from substrate and contacts are major problems to all devices that are fabricated from 2D materials, which limit significantly their mobility.

Since ultrathin van der Waals materials can be consider as 'double surfaces', they interact strongly with the environment; this can be beneficial as one can fabricate all types of sensors, but it can also be a bottleneck if one desires low disorder. Extrinsic disorder can come from everywhere. Firstly, silicon oxide (SiO$_2$) that is the most common substrate has a lot of charge traps due to the presence of dangling bonds and a high roughness. Secondly, disorder can be induced by surface adsorbates and during the device processing with lithography, resists, annealing, baking, and chemical treatments more defects can be created in these sensitive atomically thin layers. Carrier mobility of graphene on SiO$_2$ is in the order of 500-30,000 cm^{2}V^{-1}s^{-1} at low temperatures, while for MoS$_2$ or other TMDC (transition metal dichalcogenides) semiconductors the mobility is a few cm^{2}V^{-1}s^{-1} at room temperature. At low temperatures disorder can induce Anderson localization and the material to behave as insulator.

The universe of 2D materials is large. So far, we have mentioned only semimetals and semiconductors. There are 2D materials that are insulators (e.g. h-BN, talc, mica), semiconductors (e.g. MoS$_2$, WSe$_2$, black phosphorus, InSe, As$_2$S$_3$), topological semimetals (1T'-WTe$_2$, MoTe$_2$), superconductors (e.g. NbSe$_2$, FeSe(Te), BSCCO), magnetic materials (e.g. CrI$_3$, CrCl$_3$, Fe$_3$GeTe$_2$), anisotropic materials (e.g. black phosphorus, TiS$_3$) and many more categories. All these individual layers can be combined and stacked on top of each other creating artificial materials with unique properties [9, 10].

One of the most valuable materials is hexagonal boron nitride (h-BN), which is an insulator. Due to the absence of dangling bonds, and the ultraflat surfaces, it is the perfect environment for electronics with graphene and other 2D materials [11, 12]. With boron nitride substrates there are less electron-hole puddles and one can access lower energies at the chemical potential of graphene close to the Dirac point. Mobilities in graphene boosted to hundreds of thousands of $cm^2V^{-1}s^{-1}$. Moreover, the small lattice mismatch between graphene and h-BN was the reason of the Moire based superlattices that form when graphene is placed on top of h-BN. The period of the superlattice is rotation dependent and can be controlled. Such a property can result in the opening of a small bandgap, thereby creating secondary Dirac cones in graphene or 'Hofstadter butterfly' physics and broken symmetry states [13–15].

Although disorder from the substrate has been eliminated, the top surface of graphene is still exposed to chemicals and polymers. Since van der Waals bonding is the way that a flake adheres to the substrate, one can use the same force to pick-up flakes. The Columbia group showed that boron nitride can be used to pick-up and sandwich graphene [16]. Through this innovative procedure, quality is further improved and the interfaces are ultra-clean apart from regions with bubbles from water and residues. Moreover, the problem of contacts was solved by the formation of one-dimensional edge contacts. Such devices exhibit mobilities in excess of 1,000,000 $cm^2V^{-1}s^{-1}$ in good quality graphene, and mean free paths of a few microns [17]. One more step to reduce extrinsic disorder is the use of graphite gates in combination the h-BN so any influence of charged impurities from the substrate and the individual layers, can be eliminated.

Later on, the same technique has been used to assemble similar heterostructures based on MoS_2, WSe2 black phosphorus and other 2D semiconductors [18–20]. It was the beginning of devices that consisted completely from 2D materials. Unlike graphene, semiconductors are more challenging to form ohmic electrical contacts, and the problem of the Schottky barriers hindered advancements on devices based on these materials. Many groups worked on solving this issue [21].

Although the issue of the Schottky barriers, as well as the low quality of 2D semiconductors hindered experiments on quantum transport, optical experiments, photodetectors and LEDs (Light Emitting Diodes) were pursued by many research groups. Photodetectors are less prone to extrinsic disorder and Schotty barriers allow to investigate properties of the photodetectors. Spectroscopic techniques can probe properties of excitons and do not require fabrication of devices; the excitonic properties of semiconducting TMDCs and their combinations came into spotlight [23].

From all the 2D semiconductors, TMDCs have been studied mostly. This fact is because of two reasons. Fistly, TMDCs exhibit a layer dependent bandgap at optical frequencies, that is indirect in bulk and direct in a monolayer [24]. The second reason is the unique band structure of TMDCs where the spin of the carriers is coupled to the valley degree of freedom as a result of the spin-orbit coupling (SOC) in combination with broken inversion symmetry [25]. In transport experiments the consequences of such a band structure result in Ising superconductivity, and the Berry curvature of the bands is responsible for topological currents, while the spin-valley Hall effect or coupling of a magnetic field to the valley magnetic moment results in the valley Zeeman effect. In optical experiments circular polarized light can excite carriers on specific valleys, based on

1
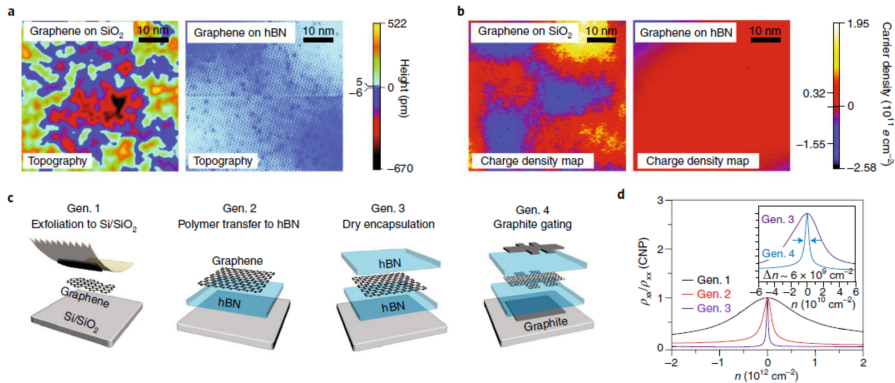
Figure 1.2: Minimizing extrinsic disorder in graphene. (a) Topography (a) and Charge density (b) maps of graphene on SiO$_2$ and h-BN.(c) Different types of graphene devices based the degree of disorder. Generation 1 devices consist of graphene on SiO$_2$, second generation take advantage of polymers to transfer graphene on h-BN. In generation 3, devices are fully encapsulated with h-BN and assembled via dry-transfer techniques. Finally, in the fourth generation graphite is used as top and bottom gates to reduce even further disorder. (d) Longitudinal resistance as function of carrier density of devices based on the gen. 1-4 schemes. The reduction of the disorder is reflected on the decreased broadening of the Dirac peak. Fully encapsulated with bottom and top h-BN dielectrics and graphite gates devices exhibit the lowest disorder. Image adapted from [22].

the chirallity of the light, which is promising for quantum information processing. The new field that has emerged is called valleytronics [26].

As mentioned above, 2D materials are sensitive to their environment. When a 2D material is placed on top of a substrate with a specific property, it can inherit that property. To elaborate further, graphene on TMDCs or transition metals, can acquire spin-orbit coupling as a result of orbital hybridization [27], similar to proximity induced superconductivity in normal thin films. Through interface engineering, one can achieve different types of SOC, and modify the band structure of graphene or other 2D materials accordingly. Another example of such engineering is the proximity induced superconductivity [28] or the magnetic proximity effect [29]. Such properties can be used for the realization of Majorana bound states and topological states in 2D heterostructures [30].

Lastly, I end by mentioning the emergence of the field of twistronics. As mentioned above stacked 2D materials can be rotated with respect to each other. Earlier reports on tunneling between two graphene layers separated with ultrathin boron nitride took advantage of this property to investigate momentum conservation during tunneling of carriers [31]. In 2018 it was discovered that artificially misaligned bilayer graphene at an angle of 1.05 ^{o} becomes superconducting and a Mott insulator due to the formation of a flat band at the charge neutrality point [32, 33] in agreement with the theoretical predictions [34]. This discovery was reproduced quickly by other groups [35, 36] and very soon expanded to other 2D systems [37]. The condensed matter research is not the same as twisting a material can result in altering its properties dramatically. Who can say that 'magic angles' cannot make boron nitride conducting or quench the superconductivity

1
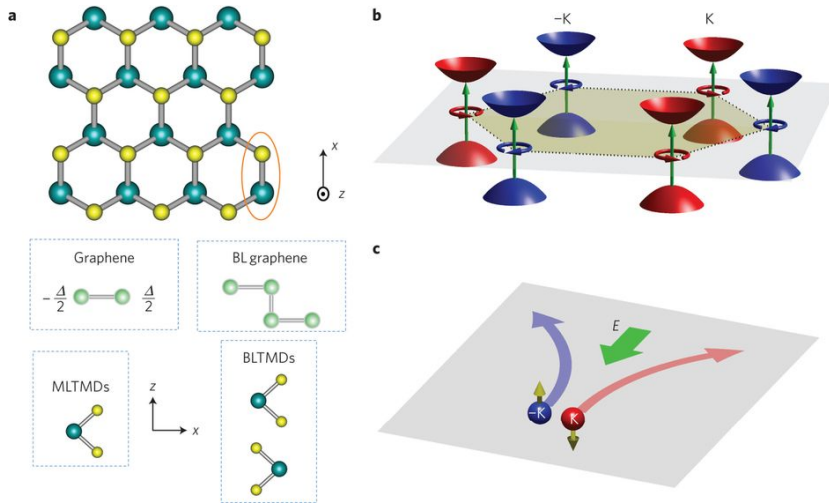
Figure 1.3: Structural and spin-valley properties of TMDCs. (a) Top view of the hexagonal lattice of TMDCs with blue spheres the transition metal atoms and yellow spheres the chalcogen atoms (upper panel). The bottom panels show side view of the structure of monolayer and bilayer graphene and TMDCs. Monolayer graphene has a broken inversion symmetry if the onsite energies of the A and B sublattice are different, while monolayer TMDCs have a structural inversion symmetry. The bilayer counterparts have a restored inversion symmetry that can break under the application of an electric field. (b) Hexagonal Brillouin zone of a monolayer TMDC, with the six lower bands at the its corners. States from different valleys have different spin orientation. This property results in valley contrasting optical selection rules, where σ^+ (σ^-) polarized light (circular arrow) couples and excites $e-h$ pairs from the K (K^-) valley. (c) Due to the opposite Berry curvature in the K, K^- valleys, an in-plane electric field deflects carriers from the two valleys in transverse and opposite directions, building a voltage perpendicular to the electric-field. This effect is called the valley Hall effect. Adapted from [25].

1

of NbSe$_2$? It is certain that the precision of the rotation that is required is not easy to handle and fabrication of such devices can be challenging. Nevertheless, it can be the way that scientific questions on topics like high temperature superconductivity and correlated physics can be better understood, as well as to be the way towards new platforms of electronics. Research on 2D materials might slow down, but a new discovery can ignite research onto a whole new scientific field and sometimes one needs to think simple and use simple methods, like adhesive tape, to change the world.

1.2. OUTLINE OF THIS THESIS

As the title states, this thesis reports studies on transport with 2D materials and their heterostructures. Such experiments can provide information about the electronic properties of the system. One can distinguish between insulators and metals from the dependence of the sheet resistance on the temperature. By applying a perpendicular magnetic field and measuring the transverse voltage or Hall voltage one can get information about the carrier density and the Hall mobility. At very low temperature, carriers behave more like quantum particles and their wave character can affect the resistance of the material due to interference effects. In the latter, effects like weak localization and universal quantum fluctuations take place because of the interference at time reversed paths and point defects, respectively. At very high magnetic fields the carrier trajectories form circular orbits and the carriers enter the quantum Hall regime, where they move along the edges, while the bulk is insulating (i.e, this is the first example of a topological insulator). Another example that we investigate is 'reading' the density of states of a material via tunneling techniques by utilizing ultrathin barriers; a method that provides direct measurement and visualization of gaps and states in the electronic spectrum.

All the above effects might seem somewhat non-correlated, but beyond the common aspect of experimenting with 2D materials, there are common aspects. For example, in many of the chapters we will see that electron-electron interactions play an important role. In chapter two they are the source of dephasing and possibly the intravalley spin-relaxation, while in chapter three electron-electron interactions cause the charge-density-wave formation due to a Peierls transition in TiS$_3$ or in chapter 5 where they affect the hopping of the electrons. Another example that is common in many of the experiments is disorder, which is at the origin of weak localization in MoS$_2$, localized states in WS$_2$, and Efros-Shklovskii variable-range-hopping in 1T/1T'-MoS$_2$.

This thesis includes five chapters (chapter 3 to 7) of experimental work that belong to the mesoscopic transport field. The first three chapters report experiment on planar transport using two- and four-terminal measurement techniques. In these chapters the resistance (or conductance) is studied as a function of carrier density, temperature and/or magnetic field. The other two chapters show another type of transport in 2D heterostructures, namely that of carrier tunneling through ultrathin barriers in vertical heterojuctions. The next chapter (chapter 2) introduces the experimental methods and techniques that were used for the studies presented in this thesis.

In chapter three, we study the effect of weak localization in bilayer MoS$_2$ encapsulated with boron nitride. In TMDCs the presence of weak localization indicates low to medium disorder, while weak antilocalization appears when the material has very high

Table 1.1: 2D materials and their usage in the experiments that are described in this thesis.

Material	Type	Usage	Chapter
$2H\text{-}MoS_2$	semiconductor	active layer	3
TiS_3	semiconductor/CDW	active layer	4
$1T/1T' MoS_2$	metal/semiconductor	active layer	5
graphene	semimetal	electrode	6,7
h-BN	insulator	substrate,tunneling barrier	3,4,6,7
WSe_2	semiconductor	substrate	7
WS_2	semiconductor	tunneling barrier	6

density of defects or if very large external fields are applied [38]. Weak localization and weak antilocalization are phase coherent effects and depend strongly on the spin state of the carriers. By studying weak localization in bilayer MoS_2 we get information about the spin relaxation and the phase coherence of the electrons.

The encapsulation with boron nitride when applied to other systems, can further highlight the intrinsic properties of the electronic system by minimizing extrinsic disorder. We apply this technique to TiS_3 (chapter 4), which is a semiconductor and, at low temperatures predictions, and earlier experiments have indicated that it undergoes a charge density wave transition. In this work, devices of TiS_3 sheets show metallic behavior and do not show disorder induced localization like in samples on SiO_2 substrates. Furthermore, to investigate the density and the mobility of the electrons, Hall measurements were performed, while at low temperatures non-linear transport elucidates the characteristics of the CDW phase.

Electrical contacts in MoS_2 is a bottleneck until now and complicated techniques need to be applied for ohmic contacts. A new contacting technique is based on the use of a different phase of MoS_2, that of $1T/1T'\text{-}MoS_2$. It can be obtained partially though chemical doping methods that result in a mix of phases from 1T 1T' and $2H\text{-}MoS_2$. $1T/1T'\text{-}MoS_2/2H\text{-}MoS_2$ heterojunctions showed promising results if used for contacts in $1T/1T'\text{-}2H MoS_2$ [39]. By performing multi-terminal measurements we gain information about the transport mechanism and the contact resistance of $1T/1T'\text{-}MoS_2$. Chapter five deals with this research topic.

Chapter six shows tunneling through localized states in WS_2 barriers. Using monolayer graphene between a back-gate and a WS_2 sheet, we study the individual states in the gap of WS_2 that lead to Coulomb blockade effects in the transport measurements. Sequential carrier tunneling though quantum dot like states from defects in the WS_2 is studied under an applied perpendicular magnetic field. By studying the ground state we gain information on the magnetic moment of these states and their spatial sizes.

Finally, in chapter seven we study the Landau level (LL) spectrum of monolayer graphene on WSe_2 using tunneling measurements through boron nitride. From LL spectroscopy we investigate about the electronic structure of graphene on WSe_2. The Fermi velocity of the carriers as well as the gaps of the LLs are obtained.

All the experiments above make use of different 2D materials in various roles. MoS_2 and TiS_3 are used as the active channel in the multi-terminal devices, while boron ni-

1

tride acts as top and bottom dielectric. For the tunneling experiments, the structures are more complicated and thin boron nitride and WS_2 are used as tunneling barriers with graphene as electrode. Table 1.1 shows the list of the materials with different classifications (i.e. insulator, semiconductor etc.) and their use in the different Chapters.

2

EXPERIMENTAL TECHNIQUES AND METHODS

In this chapter we introduce the processes and the techniques that were used for the realization of the experiments in this thesis. We explain the procedures and the tricks of the exfoliation. Novel ways of stacking 2D materials have provided heterostructures of high quality and we show how one can avoid problems of bubbles and blisters. As we used different polytypes of MoS_2, we explain the procedure of chemical induced phase engineering. Moreover, we present the equipment that was used for the devices that have been fabricated as well as the ones that we used for the characterization. Finally, we introduce the tools that we used for the electrical measurements and the setups that helped reach cryogenic temperatures.

(a)   (b)
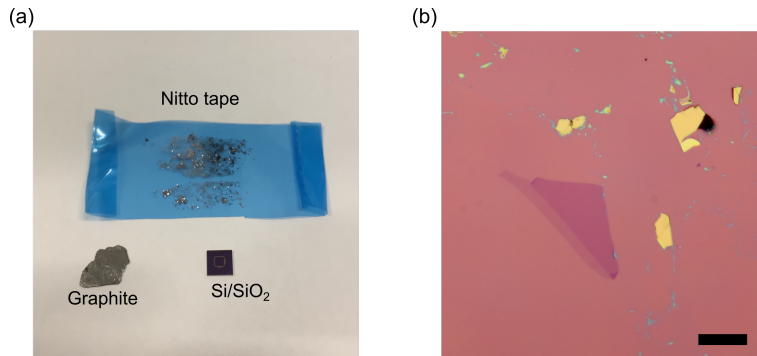
Figure 2.1: Exfoliation of a van der Waals material. (a) Components required for the exfoliation: A bulk crystal, which is natural graphite in this case, a sticky tape (Nitto) and a substrate (SiO_2/Si). (b) Graphene and graphite flakes on SiO_2/Si as seen under an optical microscope. Bar corresponds to 50μm.

2.1. INTRODUCTION

A fun part of studying properties of 2D materials and their heterostructures is the processes of exfoliation, assembly, device fabrication that we will explain shortly. Unlike studies on conventional 2DEGs (2D electron gasses) in quantum wells were the layers are formed via molecular beam epitaxy (MBE) and device mesa that are buried in the stack, 2D materials have completely different fabrication procedures.

The basic route towards the creation of a device based on 2D materials, goes as follows: Firstly, we need a 2D sheet and this can be grown or exfoliated as in the case of 2D materials. Then what follows is the assembly of the 2D heterostructure or if one wants only to study the bare material one can move directly to the step where he/she designs the device. The design of a device is important. For example, a Hall bar is used to perform Hall measurements and magnetoresistance without the contribution of the resistance from the contacts. If avoiding the edges of the channel is of major importance, a Corbino geometry or a tunneling device is more appropriate. After designing the device, the fabrication process takes place, where electron beam lithography, metal deposition or etching steps are applied. Once the device is ready the measurements can be performed. In case of optical experiments or basic material characterization one can perform measurements without the need to fabricate a device first. Then the data process and the drawing of the conclusions are the final steps of the process. In the following sections we explain the steps of the above route in more detail.

2.2. THE ART OF EXFOLIATION

Exfoliation of 2D van der Waals materials is the starting part of the process. This part requires three ingredients: A bulk crystal of a van der Waals material, for example graphite for isolation of graphene or molybdenite for MoS_2 (Fig. 2.1a). Mechanical exfoliation of bulk crystals results in better quality of flakes than liquid exfoliation or chem-
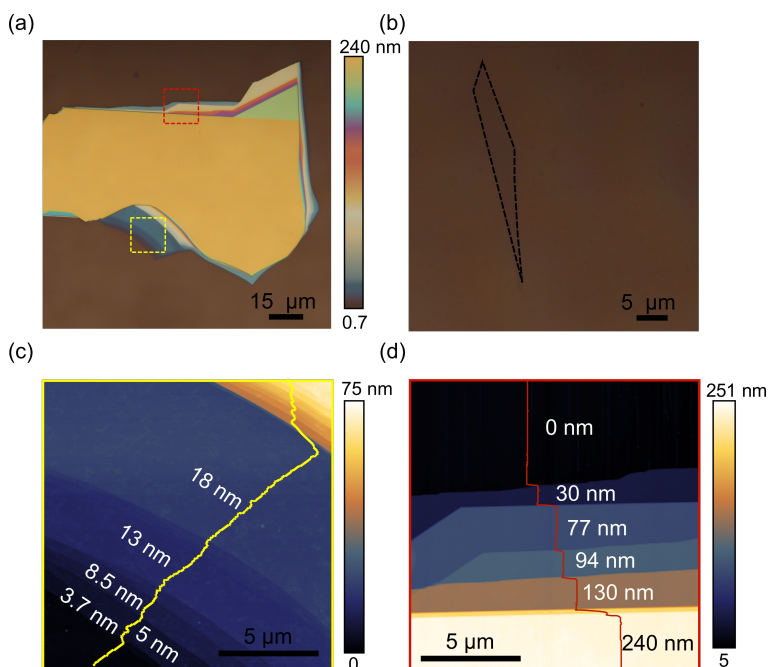
Figure 2.2: Color-thickness correspondence of hexagonal boron nitride on 90 nm SiO2/Si substrates. Optical image of a large flake with multiple terraces. The two colored square regions are the areas that were scanned with AFM and presented in panels (c) and (d). The colorbar on the left shows the color of the h-BN as its thickness varies. (b) A thin flake of h-BN, presumably bilayer.

ical vapor deposition (CVD) growth of flakes. The second ingredient is an adhesive tape or tapes (Fig. 2.1). The choice of the adhesive tape is important as it can contaminate the flakes if it has a lot of tack, or in some cases it may force the flakes to break into small pieces. In the experiments that we conducted in this thesis, we used mainly blue Nitto tape, scotch magic-tape and polydimethylsiloxane (PDMS) films.

The third ingredient is a proper substrate where the flakes will be exfoliated onto in order to be identified and processed further. Usually the substrate that is being used by the community of researchers, is SiO_2/Si although Si with another dielectric on top such as Si_3N_4 is used sometimes. In order for atomically thin flakes to become visible the thickness of the SiO_2 must have specific values in order to maximize the contrast of the flake. Typical values are 285-300 nm for graphene, MoS_2 and other 2D metals, semimetals and semiconductors. In the case of dielectrics, such as h-BN and talc, which have a refractive index with lower value, SiO_2 with thickness of 90 nm is an ideal substrate in order for a monolayer or bilayer to be visible. The contrast or color of the flake depends on its thickness. Once calibrated, an optical inspection of a flake can provide the number of the layers accurately without the need of Raman spectroscopy or atomic force microscopy (AFM). We have found that oxygen plasma cleaning of the substrates prior to the exfoliation increases the yield significantly.

We show in Fig. 2.2 an image of an exfoliated h-BN flake on 90 nm SIO$_2$, with multiple step-heights. Using atomic force microscopy (AFM) we measured its thickness and created the colorbar. For encapsulation of graphene or another 2D material, an h-BN that can serve as bottom and top dielectrics the typical thickness is 10-40 nm, although up to 60 nm thick h-BN can also work but the visibility of the intermediate layer is poor in that case. For h-BN that serves as a tunneling barrier the optimal thickness is between 1-5 layers. With a thickness of 3-5 nm (9-15 layers), h-BN, can serve as a barrier between two conducting layers like that of graphene for Coulomb drag or exciton condensation experiments [40], where the motion of the carriers in one layer affects the motion in the other without tunneling through the h-BN. So it is evident that a 2D material can be used for different purposes at different thicknesses. Another example is multi-layered graphene where at larger thickness it can be used as a gate electrode.

Recently it was found that heating while making the contact between the adhesive tape (with exfoliated flakes) and the targeted substrate can improve the yield of exfoliated flakes due to better interaction between flake and substrate [41]. In this thesis we used for the exfoliation of most of the materials the magic scotch tape heated to 100 ^{o}C to obtain thin flakes with large area. Alternatively, we used exfoliation with PDMS for example in the case of TMDCs where conventional exfoliation results in very small and thick flakes. This is even more amplified when Nitto tape is used, presumably due to the softness of this tape. Although the hot exfoliation results in a lot of polymer residuals on the substrate, the flakes are contaminated mainly on the edges and not in the bulk. Lastly, post-annealing at high temperatures (350-400 ^{o}C), should be avoided because although it cleans the flakes and the substrate, it increases the adhesion between flake and substrate and pick-up of the flake is not possible thereafter.

2.3. ASSEMBLY OF 2D HETEROSTRUCTURES

One can say that the biggest advantage of 2D materials is that they can be assembled in anyway that one desires. Unlike in 3D materials that are grown epitaxially where crystal structure and lattice constants are important in determining whether two materials can form a stack, in van der Waals material such obstacles do not exist.

Earlier methods of stacking of 2D materials involved complicated routes that involved covering them with polymers, etching of substrates and cleaning in solvents so a stack can form in a layer-by-layer way like Lego bricks. After the discovery of the dry-transfer techniques, such methods have become obsolete and the quality of heterostructures have improved substantially. Especially, the van der Waals pick-up technique, that is used to form 2D heterostrcutures by taking advantage of the adhesion to polymers and of the van der Waals forces of 2D materials, can improve significantly the quality of the heterostructures [42, 43].

Based on the pick-up technique, stamps of a glass slide/PDMS/and polycarbonate (PC) or (polypropylane carbonate) PCC are used to pick-up a flake that serves as the top layer and via van der Waals forces the subsequent ones are picked-up. When the polymer gets in contact with the 2D flake, the temperature rises above its glass transition temperature (T_g) where it behaves more like a liquid and covers uniformly the flake. After cooling down below T_g, the flake can be picked-up. Subsequently, the rest of the
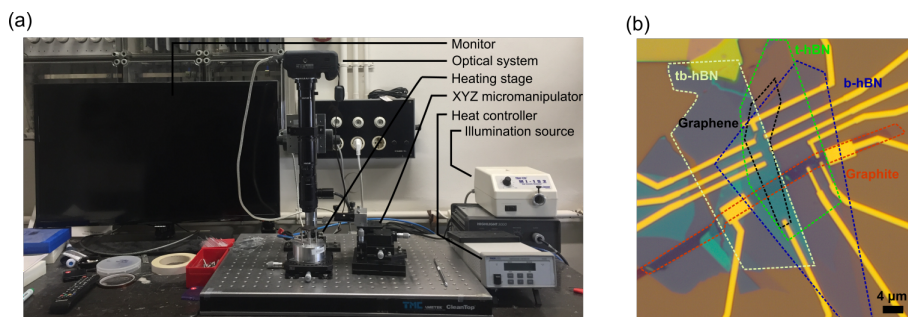
Figure 2.3: Setup for assembly of heterostructures and a van der Waals heterostructure. (a) Stamping and stacking setup of 2D materials at the Kavli Institute consisting of: a light source, a monitor, a XYZ-micromanipulator, a hating stage with a vacuum chuck embedded on an XY-positioning and rotating stage, as well as a heat controller. (b) A heterostructure fabricated with the current setup that can be used for tunneling experiments. The structure is h-BN/graphene/h-BN/graphite/h-BN on SiO$_2$/Si.

2D materials are picked-up and stacked on top of each other. This way the structure is formed on the polymer from top to bottom. The choice of the polymer, which can be PC or PCC or even PMMA, is important and depends on the limitations of the 2D materials that are used. For example, the working temperatures of PCC are much lower than those of PC and that is why PPC is better for temperature sensitive materials. On the other hand, graphene cannot be picked up with PPC but PC or a polymer that has a glass transition at a higher temperature may be used in that case. Also, for angle-aligned heterostructures higher temperatures tend to rotate the fakes with respect to each other and any attempts to construct magic angle superlattices can fail. Lastly, we have noticed that assembling heterostructures at a temperature above 120 ^{o}C results in negligible bubbles and blisters. Nowadays complete robotic systems that can exfoliate, recognize and stack flakes, have been developed [44].

Another way to construct 2D heterostructures is based on the dry-transfer technique (Fig. 2.5) [45, 46]. Based on this technique no heating is required and using PDMS stamps the flakes are stacked one after the other. The disadvantage is that the flakes have to be exfoliated on the PDMS although there are recent reports, where water assists the pick-up with PDMS [47]. This method, however, results in more bubbles at the interface of the materials and contamination from the PDMS cannot be excluded [48].

In this thesis the van der Waals pick-up technique was used to assemble the heterostructures. In the beginning of this Ph.D. the stamping method was also explored but was found to introduce more bubbles at the interfaces. Moreover, the PDMS stamping which relies on exfoliation and thinning of the flakes on the film itself, is limited to the usage of thick layers of boron nitride and insulators as a result of the low optical contrast of the thin flakes.
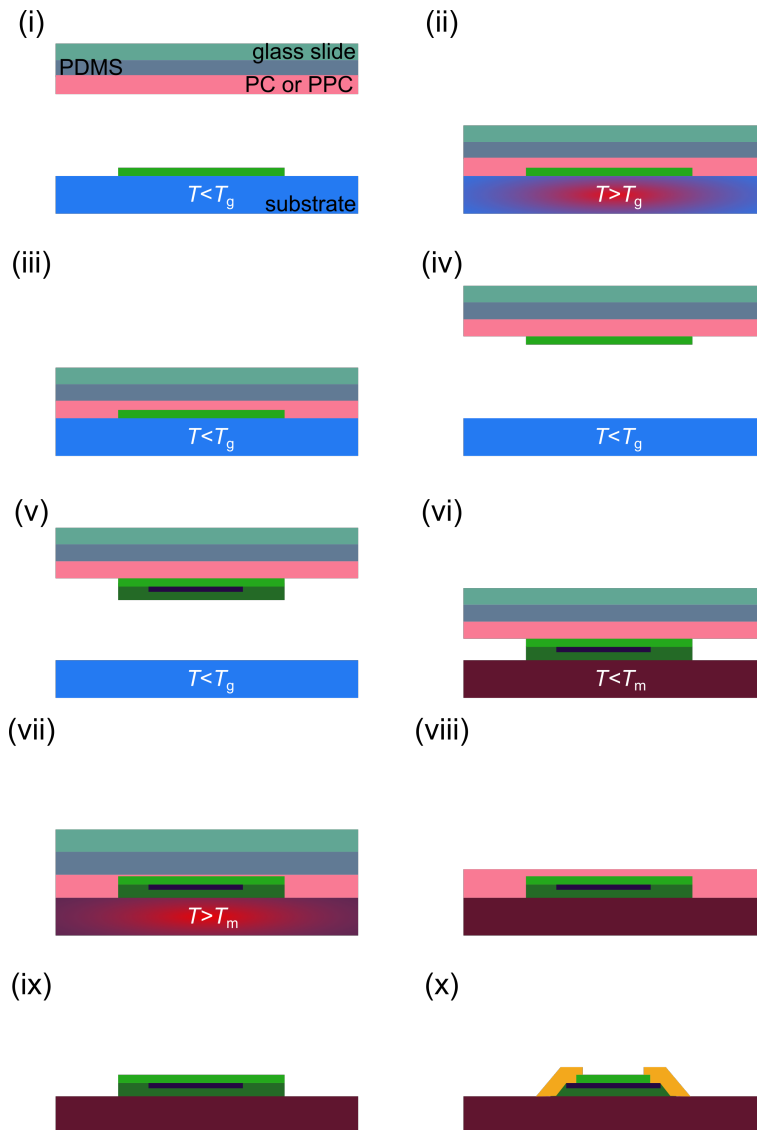
Figure 2.4: Assembly of 2D heterostructures using a pick-up method based on adhesive polymers. (i) The glass/PDMS/PC(PPC) is brought above the flake, (ii) The stamp is brought into contact with the flake and the temperature rising above the glass transition T_g so the polymer expands and covers the flake uniformly. (iii) When the temperature reduces below T_g then the stamp is retract and the flake is n the PC or PPC (iv). (v) Repeating steps (i-iv) for assembly of the stack. (vi) The final substrate is places below the 2D heterostructure. (vi) The heterostructure is brought into contact with the substrate and (vii) the temperature increases to above the melting point of the polymer (T_m). After retracting the PC or PPC with the heterostructure stay on the substrate (viii). (iv) After washing in a specific solvent to remove the polymers the structure can be process for the fabrication of the final device (x).
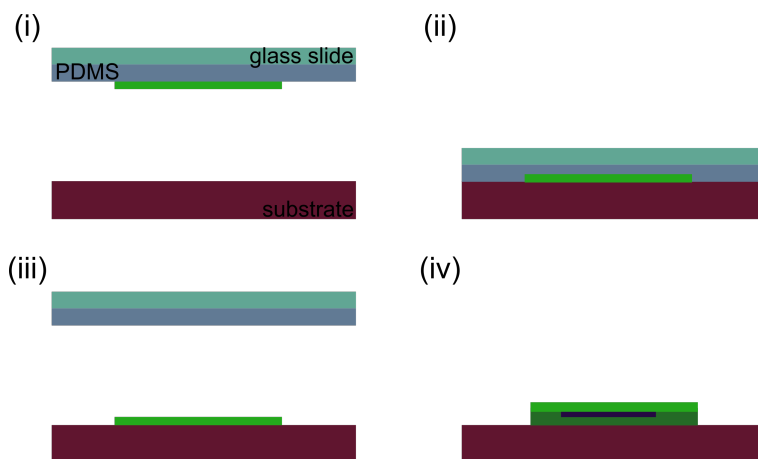
Figure 2.5: Assembly of 2D heterostructures using dry-transfer with stampping.(i) A PDMS stamp with an exfoliated flake is sitting on a glass slide and is brought above the targeted substrate. (ii) the stamp is brought into contact and upon releasing the flake stays on the substrate (iii). (iv) Repetition of steps (i-iii) multiple times to form a stack.

2.4. BASIC CHARACTERIZATION TECHNIQUES

For this particular thesis we used mainly four techniques to characterize our flakes without contacting them electrically: Optical microscopy, atomic force microscopy Raman and photoluminescence spectroscopy. These four tools combined can provide information about the thickness of the flakes or the stacks, their homogeneity, the presence of bubbles at the interfaces and material quality.

As we saw in the previous section, the color and contrast of the flake when placed on Si/SiO$_2$ substrates is strongly dependent on its thickness. It is therefore relatively easy to search and identify flakes with specific thickness and morphology for a desired experiment or application. Atomic force microscopy uses a tip on a cantilever to measure topology and can provide information about thickness, homogeneity and the presence of cracks or other "defects" that are difficult to detect optically. Measuring the thickness of a monolayer in non-contact mode is challenging because the interaction between tip-substrate and tip-flake can result in overestimation of the thickness.

Raman spectroscopy became popular technique in studies of carbon based (nano) materials. Raman spectroscopy probes phonon from the center of the Brillouin zone by exciting electrons in real or virtual states, thereby the electronic structure can play a significant role. In the case of 2D materials and based on the behavior of the peaks, Raman spectroscopy can provide information about the number of the layers, the strain, the doping and the disorder.

Lastly, photoluminescence (PL) spectroscopy is applied to semiconductors and the spectrum depends on the size of the band gap and whether the band gap is direct or indirect. We applied this technique to the TMDCs, due to their layer dependent bandgap at optical wavelengths. The spectrum can also tell us information about the doping and the

2
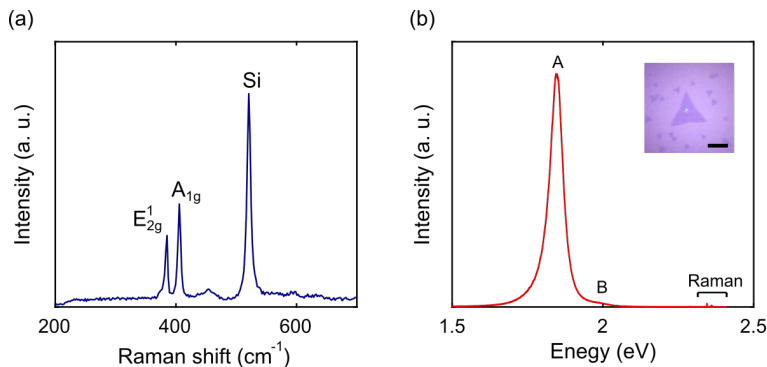
Figure 2.6: Raman (a) and photoluminescence spectra (a) of monolayer MoS_2 obtained with Renishaw inVia under illumination with a CW laser (λ=514 nm). In the case of Raman the two characteristic peaks of MoS_2 at 385 and 405 cm^{-1} can be seen, along with the peak from the silicon substrate at 520.7 cm^{-1}. In the case of the PL spectrum the A excitonic peak is evident, while the B excitonic peak and the Raman bands are more weakly present.

disorder as trap states can be seen as extra peaks in the spectrum. Finally, excitons can be studied and in the case of 2D materials many excitonic complexes exist in individual layers and heterostructures with interesting physics.

For the Raman and photoluminescence spectroscopy measurements we used a *Renishaw InVia* system which is equipped with a continuous wave (CW) excitation laser at 514 nm with a diameter spot less than 1 μ when focused with the 100x objective. The grating of 1800 lines/mm provides high resolution spectral separation (0.5 cm^{-1}) and an edge and notch filter is cutting-off the laser line before the signal reaches the peltier cooled CCD detector. With this system apart from obtaining spectra, using the X,Y automatic stage one can also perform Raman or PL mapping that can provide information about the spatial characteristics of samples. An example of Raman and PL spectra from monolayer MoS_2 can be seen in Fig. 2.6.

2.5. DEVICE FABRICATION

The fabrication of devices takes place inside the clean room of the Kavli institute, where the fabrication tools are and the contamination from dust and other particles is minimum (level 10,000-100). For the device fabrication described in this thesis, we mainly used three tools: (a) electron beam (*e*-beam) lithography, (b) reactive ion etching (RIE) and (c) metal deposition.

An electron beam pattern generator (EBPG) is a machine that uses an electron beam to pattern or generate a mask that is sensitive to the electron radiation. This is very similar to optical lithography, but since the Fermi wavelength of the accelerated electrons can be smaller than the diffraction limit of light, the minimum size that can be achieved is a few nanometers. Two systems have been used, both from *Raith*: the EBPG 5000+ and 5200, with an beam accelarated at 100 kV and with apertures of 200-400 μm.
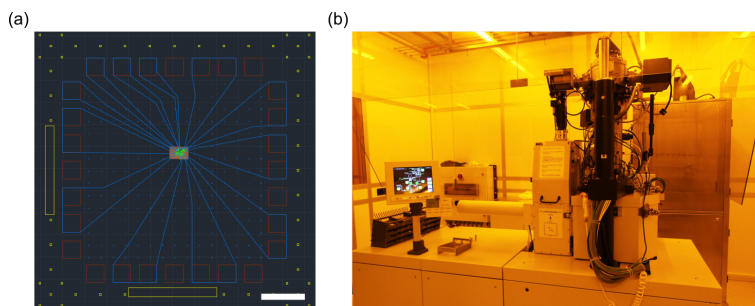
Figure 2.7: (a) A design of a complete device using AutoCAD software. Markers are yellow and blue, contact pads are red, blue and light green are device contacts and blue/purple is the etching mask. Bar is at 500 μm (b) EBPG5000+ system from the Kavli Nanolab in Delft.

Reactive ion etching is a dry etching technique that uses a chemically reactive RF excited plasma of gas molecules (O_2, Ar, CHF_3 (Fluoroform), SF_6 etc.) at low pressures to etch away material. Both sputtering (removal of material) due to the kinetic energy of the ions and removal due to chemical reaction of the ions on the surface take place. We have used mainly fluoride rich gases at pressures of a few microbar and power of less than 100 W. As etching masks we usually used Polymethyl methacrylate (PMMA), CZAR (ARP) resists as well as hydrogen silsesquioxane (HSQ).

For metal contacts and gates we used metal deposition through *e*-beam evaporation. The accelerated electron beam is guided on the crucible (with the metal) with magnetic lenses and consequently heats the material. The substrate sits above the target and faces downwards. Typical metals used in this thesis are titanium and chromium as sticking layers and gold or gold-palladium alloy on top.

The process of making a device can be found in each chapter individually and step-by-step fabrication recipes can be found in the appendix. We should mention though that the process consists usually two *e*-beam lithography steps, one dry etching step and one step of metal deposition for a device without any local gates (Si then acts as a global gate). If one does not need to have a specific device shape then just one step of *e*-beam lithography is efficient and one step of metal deposition. In chapters three and four we used a more complicated route with pre-patterned top boron nitride, prior to stacking and device fabrication steps, in order to ensure ohmic contacts to the devices.

During measurements, the device is connected with the outside world via wires. Cables from the measurements setups are reaching the dip sticks or the setup where the device is placed. In the case of a probe station the probes touch the device pads where currents and voltages are applied directly. On the other hand most of the setups contain PCBs (printed circuit board) on which the device is attached and wire-bonding has to take place. The wire-bonding technique is a complex process where the ultrasonic power heats the metal wire (Al-Si alloy or Au) that touches the device pads so that welding between pad and wire takes place. Toward avoiding problems such as gate leakage (too high force and power) or wire detachment (too weak force/power or bad adhesion of pad contacts), the bonding parameters such as force, power and time, need to be op-

2
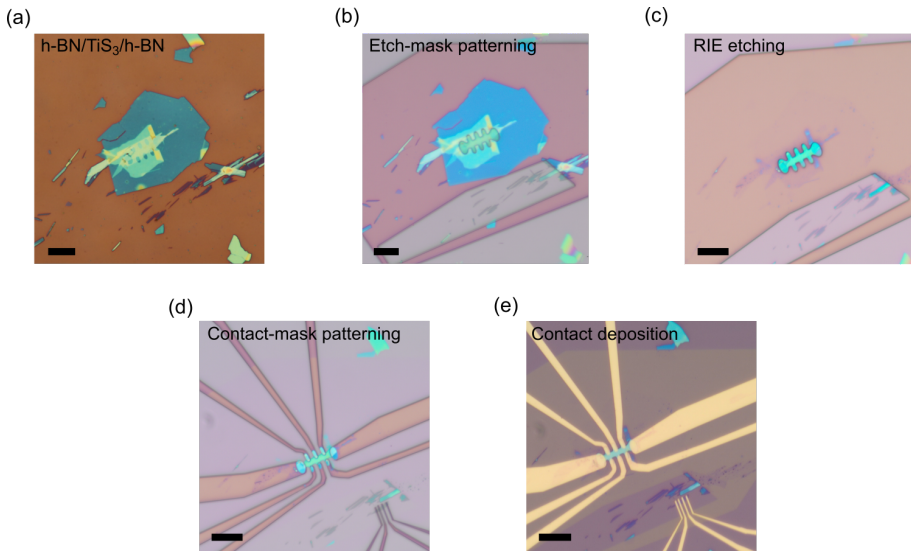
Figure 2.8: Optical images of a device after multiple fabrication processes. (a) An h-BN/TiS$_3$/h-BN heterostructure on 285 nm SiO$_2$/Si. (b) Heterostructure with a PMMA mask that defines the shape of the device (Hall bar) after e-beam lithography. (c) Structure after RIE etching with ChF$_3$/O$_2$ gas at 50 μbar and 60 W. (d) Stack with a PMMA mask that defines the contact leads to the Hall bar after e-beam lithography. (e) Complete and final device with Ti/Au contacts. Scale bars correspond to 10 μm.

timized. In the case of absence of a global back-gate silicon electrode, and with the use of local gating the above mentioned problems are reduced since one does not have to worry about gate leakages. Lastly, it is very important that the contact pads are nicely adhered to the substrate using a sticky layer like titanium in order to avoid metal pad detachments.

2.6. PHASE ENGINEERING IN MoS$_2$

Many materials have many allotropes and polytypes. That is when two materials share the same stoichiometry or chemical composition, but they have different structure and properties. A very well known example is graphite that has as allotropes diamond, carbon nanotubes and fullerenes. In this thesis we explored the allotropes of MoS$_2$ such as 1T and 1T′ MoS$_2$. Similar polytypes exist for WSe$_2$, WTe$_2$, MoTe$_2$ etc.

MoS$_2$ occurs naturally in the trigonal prismatic phase or 2H-phase (in the monolayer is called 1H). In this phase MoS$_2$ is a semiconductor with a band gap that depends on the number of layers. 1T-MoS$_2$ is metallic and 1T′-MoS$_2$ is a semiconductor and is potentially a spin Hall insulator. The route to transform the 2H-phase to the 1T and 1T′ phases is via doping. An electron density of above 10^{15} cm^{-2} can be sufficient to establish such a transition. The problem is that the 1T phase is metastabe and relaxes to the

2
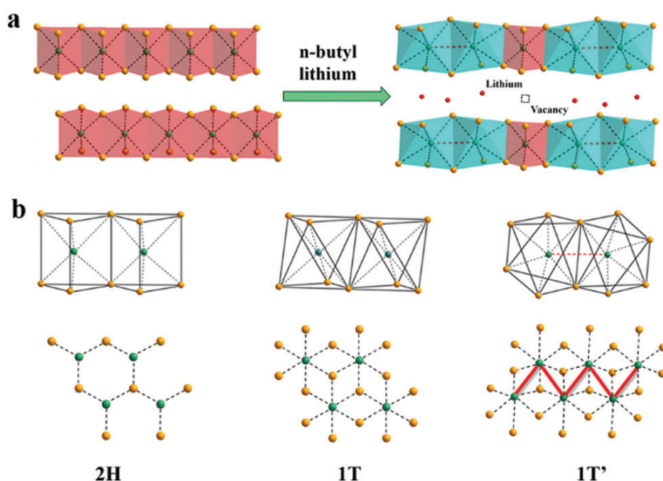
Figure 2.9: Phase engineering in different polytypes of MoS_2. (a) 2H-MoS_2 after immersion in n-butylithium becomes mainly 1T and 1T$'$ MoS_2 with a small areas of 2H-MoS_2 due to doping from the intercalated lithium. (b) Top view and side view of the crystal structures 2H-MoS_2 (trigonal prismatic), 1T-MoS_2 (octahedral) and 1T$'$-MoS_2 (distorted octahedral). Image adopted from [49]

1T$'$, causing an inhomogeneous landscape within a flake, with coexisting phases.

Chemical doping is an easy way for obtaining 1T/1T$'$ MoS_2. Solvents that are rich in alkali metals are usually employed. In this thesis n-butyl lithium was used that requires inert conditions for its usage. Exfoliated flakes were immersed in the solution for more than 24 hours and then they were washed with water and IPA (Fig. 2.9 and 2.10). The disadvantage of this technique is that some 2H phase remains.

2.7. ELECTRICAL MEASUREMENT SETUPS

For electrical measurement at room or low temperatures we used electronic equipment that has been fabricated at TU Delft (*DEMO*). It allows to perform low-noise and high-resolution measurements (IVVI-Rack). The optical digital-to -analog (DAC) converter
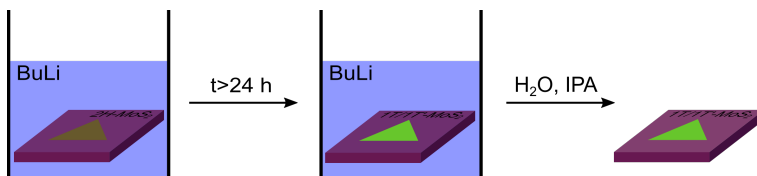
Figure 2.10: Phase engineering process via n-butylithium (Buli) in MoS_2. A substrate with MoS_2 flakes (or devices) is immersed in BuLi. After an extended period of time (>24 h) the lattice rearranges to the 1T/1T$'$ structures. Extraction and washing in H_2O and IPA results in 1T/1T$'$ MoS_2.

(16-bit) provides high resolution and low-noise signal conversion, and is connected to a computer. At the side of the sample it is connected to amplifiers that receive the signal to the device. The recorded signals from the device are collected, amplified and converted to voltages where they are being measured though a *Keithley* multimeter. The multimeter converts the analogue signal (voltages) to digital (ADC) and is sent to the computer. For lower noise and small-signal measurements we used lock-in amplifiers (*Stanford Instruments*), at low frequency AC signals.

Some of the room temperature measurements were performed in a probe station (*Lakeshore*) that allows us to apply low pressures on the sample to avoid oxygen and humidity to affect the measurements. For experiments at low temperatures (liquid helium and below) we used different types of fridges. The first is cryogenic setup that comprises of a long dip stick that can be immersed into liquid ^{4}He-bath (T =4.2, and is connected electrically to the electrical equipment). The sticks are usually equipped with a "1-K pot" to reach temperatures of ~2 K. We have also used a dry fridge or closed cycle cooling system (*Montana Instruments*), where the ^{4}He is condensing with the help of a variable flow helium compressor. The sample is in a compartment that is under vacuum. Lastly, in order to reach temperatures below 2 K we used a dilution refrigerator (*Leiden Cryogenics*), but due to a defect in the setup we did not manage to reach temperatures less than 300 mK for long duration. The fridges based on liquid ^{4}He and the dilution refrigerator, are also equipped with superconducting solenoids that can reach 8 and 14 T, respectively for magnetotransport measurements.

2.8. Contact engineering in MoS$_2$

On of the most challenging physical problems in mesoscopic devices is the formation of good ohmic contacts, which are required for transport experiments. In the case of a large contact resistance there are two problems: firstly, sourcing and draining the current from the device becomes difficult. This has also an extra effect, which is the Joule heating at the contacts. Second, if the contact resistance becomes comparable or larger than the internal resistance of the voltmeter, then the measured value on the voltmeter does not correspond to the difference of the potential across the channel. In general the contact resistance should be zero ideally, though this is not possible, but low values that are in the order of a few hundreds of ohms or a few kΩ at low temperatures are good for transport measurements.

Contact resistance is usually created by a barrier that forms at the interface of two metals, two semiconductors or metal and a semiconductor, and depends on the values of the workfunctions of the two materials. At equilibrium, the Fermi level across the junction has to be constant and this condition is established via charge transfer between the two materials. Charge transfer will cause band bending and the creation of a (build-in) potential, which in turn act as barrier for thermionic or field-emission of carriers. This barrier is called Schottky barrier. Therefore, choosing materials with similar values of workfunctions is a workaround this problem. For metal-semiconductor contacts this is more challenging and usually ion implantation below the contacts helps to increase the doping locally and help with the aforementioned alignment. Lastly, in this discussion we have ignored the Fermi level pinning effect, which originates from metal-
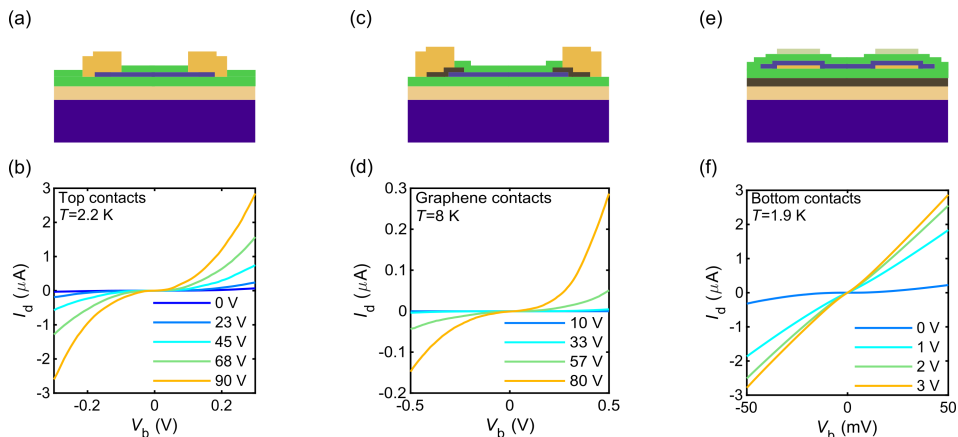
Figure 2.11: Contact engineering in ultrathin MoS$_2$. (a, c and e) Schematic illustration of the device cross-section with different contact configuration. (b, d and f) Current-voltage characteristic at different gate voltages. In the case of bottom contacts the local gates at 15 V and there is a bottom graphite gate that is responsible for the lower values of the gate voltages.

semiconductor states below the conduction band edge and make the workfunction of the metal somewhat irrelevant.

In graphene, ohmic contacts are easy to form and usually are one-dimension edge contacts [17]. In 2D semiconductors, ohmic contacts are more challenging to be achieved and there are many reports on improvements of the contact resistance through different metals and techniques, but most of them fail at low temperature [21, 50–53]. Nevertheless, there are many techniques that have can provide ohmic or quasi-ohmic contacts for ultrathin semiconductors like MoS$_2$ even at low temperatures. The most known are: edge contacts, graphene contacts with or without local gates [18, 54], post-etching of the top h-BN layer and metal deposition [55, 56], using pre-etched top h-BN layer as well as bottom metal contacts with local gates [57].

We carried out further investigation and tried three techniques for making contacts monolayer and bilayer MoS$_2$: top contacts through pre-etched boron nitride on monolayer (Fig. 2.11 a and b), graphene contacted bilayer (Fig. b and c) and bottom contacts on monolayer (Fig. d and e). As it can be seen from the I_d-V_b of the devices at low temperatures, the best configuration is the one of the bottom contacts with local gates that shows linear characteristics even in monolayer (Fig. 2.11f). The conatct resistance based on the top contact scheme depends on the chamber pressure during metal deposition. Although it does not work that well for monolayer MoS$_2$, in bilayer it provides good ohmic contacts as we will see in chapter 3. Moreover, method based on the top-contacts provides better results in the case of TiS$_3$, which has a lower bandgap of ~1 eV (see chapter 4). Also, graphene contacts could also provide good contacts in MoS$_2$ and other 2D semiconductors, but local gating is required to induce sufficient doping at the contacts.

Lastly, we should mention that we also investigated chemical doping and phase en-

2

(a)   (b)
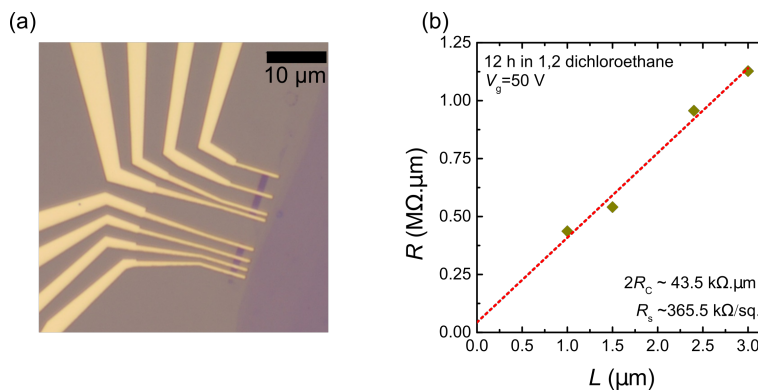
Figure 2.12: Transfer-length measurements in 1,2-dichloroethane doped monolayer MoS_2. (a) Optical image of a monolayer MoS_2 device consisting of multiple finger contacts with different channel lengths in the range of 0.5-4 μm. (b) Resistance multiplied with the width of the device versus channel length for V_g=50 V. The values follow a linear line. Extrapolating to L=0 μm the value of $2R_c$ is found equal to 43.5 k$\Omega\mu m$, while the slope yields the square resistance which is 365.5 $k\Omega$/sq.

gineering due to reports that presented promising results for reduction of the contact resistance. We, however, did not find a significant decrease of the contact resistance at room temperature. From transfer length measurements we found a contact resistance at room temperature of 20 k$\Omega \cdot \mu$m for doping with 1,2-dichloroethane, 40 k$\Omega \cdot \mu$m for ammonium hydrosulfide, and 100 k$\Omega \cdot \mu$m for doping with BuLi. At cryogenic temperatures the contact resistance would further increase and therefore the particular methods are not promising.

In chapters three, four and five we use the direct deposition of Ti/Au (top) contacts for devices with 2H-MoS_2, TiS_3 and 1T/1T′-MoS_2, respectively. In the other two chapters we use tunneling devices with graphene and we use edge contacts of Cr/Au layers.

3

WEAK LOCALIZATION IN BORON NITRIDE ENCAPSULATED MoS$_2$

We present measurements of weak localization on hexagonal boron nitride encapsulated bilayer MoS$_2$. From the analysis we obtain information regarding the phase-coherence and the spin diffusion of the electrons. We find that the encapsulation with boron nitride provides higher mobilities in the samples, and the phase-coherence shows improvement, while the spin relaxation does not exhibit any significant enhancement compared to non-encapsulated MoS$_2$. The spin relaxation time is in the order of a few picoseconds, indicating a fast intravalley spin-flip rate. Lastly, the spin-flip rate is found to be independent from electron density in the current range, which can be explained through counteracting spin-flip scattering processes based on electron-electron Coulomb scattering and extrinsic Bychkov-Rashba spin-orbit coupling.

3.1. INTRODUCTION

Molybdenum disulphide (MoS$_2$) is a member of the family of transition metal dichalcogenides (TMDCs) with semiconducting properties, in which the interplay between spin and other pseudo-spins, such as valley and layer index, has created new prospects for spintronics and valleytronics [25, 59]. Bilayer MoS$_2$ is centrosymmetric and the subbands of the two K and K′ valleys are spin degenerate under non perturbed conditions [60]. When an out-of-plane electric field is applied, an inter-layer potential is generated and the inversion symmetry breaks and leading the possibility of spin-valley locking in bilayers [61–63].

Quantum corrections to the conductivity due to interference effects of charged carriers in disordered systems can provide information about fundamental properties of the carriers that reside in the system [64, 65]. They can, for example, provide information about the phase-coherence as well as about spin[65], and other types of scattering rates of the carriers [66]. Specifically, in MoS$_2$ and other TMDCs, weak localization (WL) or weak antilocalization (WAL) can provide crucial information about the spin lifetime established by intravalley and intervalley scattering, as well as about the Zeeman-like splitting that is induced by the intrinsic SO coupling [38, 67].
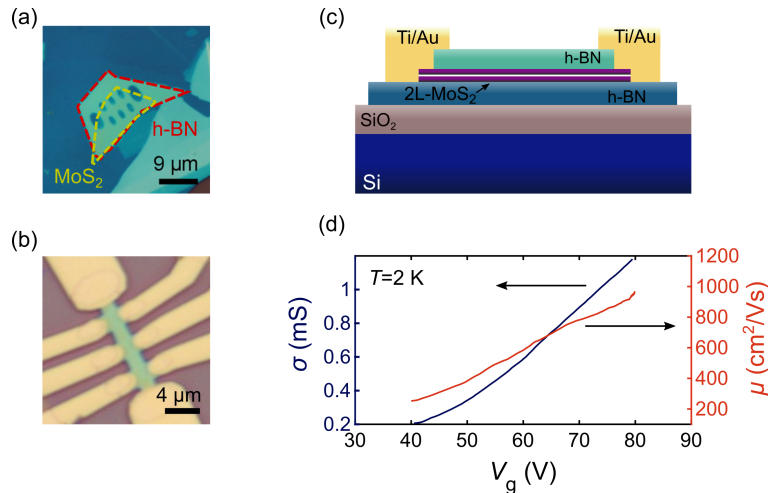
Figure 3.1: A high-mobility encapsulated MoS$_2$ bilayer Hall bar and device characteristics. (a) Optical image of an h-BN/2L-MoS$_2$/h-BN stack, with pre-patterned holes in the top h-BN. (b) Optical image of a completed Hall bar device. (c) Cross-sectional schematic of the device. (d) Electrical conductivity, σ, and electron mobility μ as a function of the gate voltage V_g, obtained from Hall measurements at $T = 2$ K.

Although other studies have observed WL in disordered monolayer [67] and in a few-layer MoS$_2$ samples [68, 69] the case of bilayer and boron nitride encapsulated has been unexplored. In this chapter, we study weak localization in high quality bilayer MoS$_2$ encapsulated in hexagonal boron nitride (h-BN). Analyzing our measurements using the
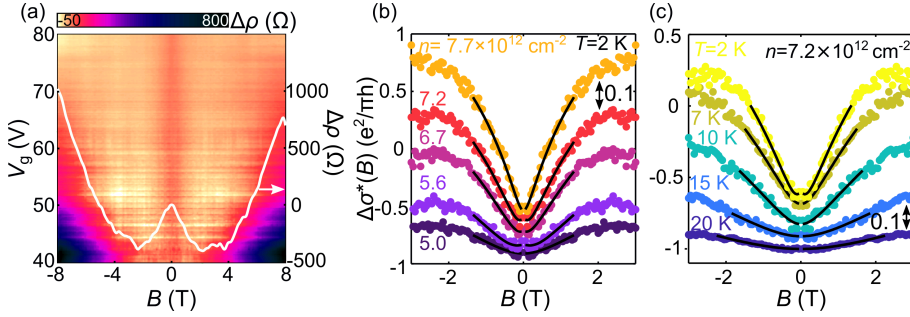
Figure 3.2: Weak localization in bilayer MoS_2. (a) Magnetoresistivity ($\Delta\rho = \rho(B) - \rho(B = 0T)$, $\rho(B = 0T) = 4.56$ kΩ at $V_g = 45$ V) as a function of the back-gate voltage (V_g) and the magnetic field (B) at T=2 K. The overlaid linecut shows the magnetoresistivity at a gate voltage of $V_g = 45$ V. (b) Symmetrized magnetoconductivity $\Delta\sigma^*(B)$ as a function of magnetic field for different electron densities n measured at $T = 2$ K. (c) Symmetrized magnetoconductivity as a function of magnetic field for different temperatures with $n = 7.2 \times 10^{12}$ cm^{-2}. The drawn solid black lines correspond to fits using the HLN model. Data and fitted curves have been shifted vertically by $0.1 e^2/\pi h$ for clarity.

Hikami-Larkin-Nagaoka (HLN) model [70], we extract the spin relaxation lengths and spin lifetimes that indicate fast spin relaxation rates through intravalley processes. Our data further suggest that the dominant source of phase-decoherence is the Altshuler-Aronov-Khmelnitsky mechanism, in which electron-electron inelastic scattering takes place [71], similar to previous studies of quantum transport in monolayer and a few-layer MoS_2 [67, 68].

3.2. RESULTS AND DISCUSSION

3.2.1. FABRICATION AND TRANSPORT PROPERTIES

Figure 3.1a and 3.1b show optical images of a van der Waals heterostructure (sample D2) and a final device (sample D1), respectively. To maintain the quality of MoS_2 during fabrication and to be able to establish good electrical contacts, we followed a different route than other studies [16, 55, 72]. Prior to the stacking of the heterostructure via the hot pick-up technique [73], at the top h-BN sheet we opened "windows" in it, via standard electron beam (*e*-beam) lithography followed by reactive ion etching. This allows the metallic contacts to be deposited directly on the MoS_2 channel [19] and recently it was shown that this can be a good alternative to graphene contacts [56]. The ohmic behavior of the current-voltage characteristics at moderate back-gate voltages V_g (Fig. 3.5) verifies the good quality of the contacts at low temperatures and allows the use of lock-in measurements, without the need of complicated stacking of graphene with local gates [54, 74]. In the main text we present results from data of sample D1, while in the supplemental material data from sample D2 can be found.

The carrier density is obtained using Hall measurements and is found to be in the
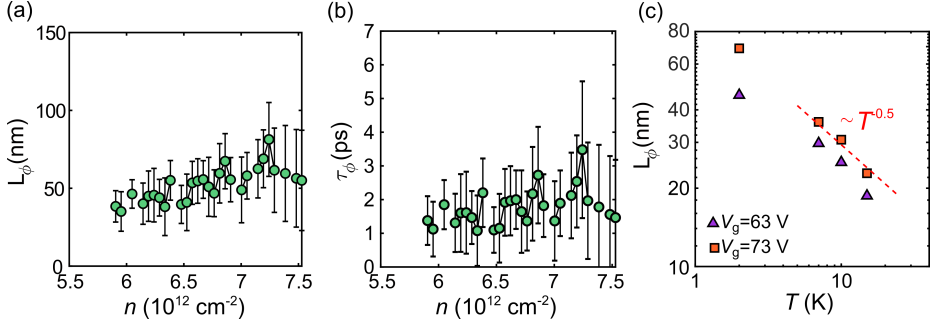
Figure 3.3: Phase-coherence length (a) and phase-coherence time (b) as a function of the electron density for $T = 2$ K. (c) Logarithmic plot of the phase-coherence length as a function of temperature, for two different back-gate voltages. The power law dependence with $a \sim 0.5$ suggests electron-electron scattering as the dephasing mechanism.

range of $4 - 8 \times 10^{12}$ cm^{-2} for gate voltages between 40 and 80 V. The conductivity versus back-gate voltage shows typical n-type behavior and increases when the temperature decreases due to the metallic character of the channel at these gate voltages (Fig. 3.5b). As a result of the encapsulation, the devices reach Hall mobilities of $\sim$1000 cm^2/Vs at V_g=80 V ($n = 7.9 \times 10^{12}$ cm^{-2}) and field-effect mobilities of $\sim$3000 cm^2/Vs at $T = 2$ K (Fig. 3.5d). The mean free path (L_e), the diffusion constant (D) and the momentum relaxation time (τ_p) are in the range of 6-30 nm, 0.4-2.2$\times 10^{-3}$ m^{2}s^{-1} and 55-200 fs, respectively, assuming an effective mass of $0.4m_0$, where m_0 is the free electron mass. Also, the Fermi level (ϵ_F) lies in the range of 13-24 meV above the conduction band edge. The electron mobility increases with the carrier density, which points to the presence of long-range Coulomb scattering [75]. The disorder induced doping in the MoS$_2$ channel can be obtained by extrapolating the carrier density to zero V_g, which gives $n_0 = 3.7 \times 10^{11}$ cm^{-2}.

3.2.2. MAGNETOTRANSPORT MEASUREMENTS

At low temperatures, the magnetoresistance in our devices shows a prominent peak around $B = 0$ T (Fig. 3.2a), a clear signature of weak localization of the electron wavefunctions. Figure 3.2b shows the symmetrized magnetoconductivity $\Delta\sigma^*(B)$ ($\Delta\sigma^*(B)$ $= (\sigma(B) + \sigma(-B))/2 - \sigma(B = 0T)$) in units of $e^2/\pi h$, for different carrier densities at $T = 2$ K and in Fig. 3.2c for different temperatures at $n = 7.2 \times 10^{12}$ cm^{-2}. As the carrier density increases, the dip at zero magnetic field becomes more prominent, while it declines with temperature. The former can can be attributed to an increase of the coherence length of the electrons with electron density, while the latter can be explained from a decrease in the coherence as the temperature increases. Furthermore, at high carrier densities the magnetoconductivities show oscillations that are ascribed to universal conductance fluctuations (UCFs) (see also Fig. 3.12). We have also observed weak localization characteristics in the sample D2, which has also similar transport characteristics (Fig. 3.6).

For the analysis of the low B-field magnetoconductivity we have employed the revised from Iordanskii *et al.* theory of Hikami-Larkin-Nagaoka [70, 76, 77] that has been

adopted for the analysis of magnetotransport in MoS_2 in previous reports [67–69]. This model contains spin-orbit terms, responsible for spin relaxations. We have also performed analysis with the recent theory for monolayer TMDCs [38]. In the main text we focus on results based on the HLN theory. The magnetoconductivity according to the HLN model is given by [69, 70, 76, 77]:

$$\Delta\sigma(B) = \frac{e^2}{2\pi^2\hbar} \times \left[F(\frac{B_\phi + B_{so}}{B}) + \frac{1}{2}F(\frac{B_\phi + 2B_{so}}{B}) - \frac{1}{2}F(\frac{B_\phi}{B}) \right]. \tag{3.1}$$

Here, $F(z) = \psi(1/2 + z) - ln(z)$ and ψ is the digamma function. Eq. (3.1), contains two variables: B_ϕ, which corresponds to the phase-coherence field and B_{so} which is related to the spin-orbit mediated spin relaxation processes. The black curves in Fig. 3.2b and 3.2c correspond to fits with Eq. (3.1). We have limited the fitting to fields below 1.5-2.2 T so we avoid contributions from the classical magnetoresistance and from UCFs.

3.2.3. PHASE COHERENCE OF ELECTRONS

From the fits, we have deduced the phase-coherence length of the electrons. In Fig. 3.3a we show the phase-coherence length as a function of the electron density for $T = 2$ K, calculated from the relationship $L_\phi = \sqrt{\hbar/(4eB_\phi)}$. The error bars have been calculated based on error propagation methods. The phase-coherence length is between 35 and 80 nm for $n = 5.5 - 7.5 \times 10^{12}$ cm^{-2}, showing an increase with the density. Even though the electron density is small in comparison to other reports [67–69], the phase-coherence lengths obtained here are among the largest reported for MoS_2, owing to the large mobilities of the samples. Furthermore, values of L_ϕ obtained from weak localization data are in good agreement with the ones obtained from the conductance fluctuations: using the equation $\Delta B = (\hbar/e)/(\pi r)^2$ [78] and for $\Delta B \approx 1.2 - 2$ T (period of oscillations), we get a length scale of 50-63 nm. Another quantity that we obtain is the phase coherence time from the relationship: $\tau_\phi = L_\phi^2/D$. Figure 3.2b presents the phase coherence time as a function of electron density. A weak density dependence can be observed with an increase from ~0.8 to ~2 ps. Lastly, the phase coherence length is found to depend on temperature with a power law: $L_\phi \propto T^{-a}$. We find values of α equal to 0.56 and 0.49, for $V_g = 63$ V and 73 V, respectively. Such values of α imply dephasing due to electron-electron scattering processes [71], which has also been reported in graphene [79], black phosphorus [78] and monolayer MoS_2 [67].

3.2.4. SPIN RELAXATION PROPERTIES

The fact that we observe weak localization in our devices indicates the absence of strong disorder that leads to intervalley spin-flip scattering and in turn to weak antilocalization [38, 67, 80]. Thus, the spin relaxation obtained through Eq. (3.1) is mainly related to intravalley spin-flip processes (Fig. 3.4a). The dependence of the spin relaxation length ($L_{so} = \sqrt{\hbar/(4eB_{so})}$) on density is presented in Fig. 3.4b. The values are between 40 and 75 nm for $n = 5.5 - 7.5 \times 10^{12}$ cm^{-2}, exhibiting an increase with n, presumably due to the increase of the diffusion constant as in the case of the phase-coherence length. The values obtained here are larger than the ones found in monolayer MoS_2 on SiO_2 (20 nm) [67] but somewhat smaller than those obtained from a few-layer MoS_2 in weak localization
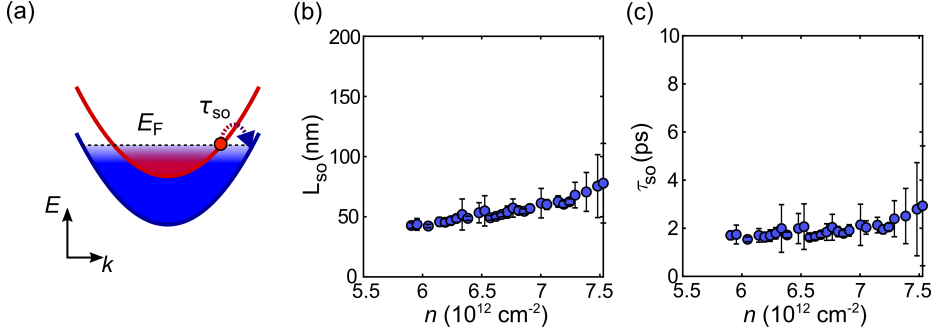
Figure 3.4: Spin relaxation properties of electrons in bilayer MoS$_2$. (a) Energy-dispersion schematic illustrating spin relaxation due to intravalley spin-flip process. Different colors represent electron populations of different spin orientations. Spin relaxation length L_{so} (b) and time τ_{so} (c) as a function of electron density ($T = 2$ K); obtained from fitting the magnetoconductivity data to Eq. (3.1). The spin relaxation length increases with electron density, while the spin relaxation time is independent of the electron density.

(100-270 nm) [68, 69] and non local spin measurements ($\sim$ 200 nm) [81]. We note that the spin relaxation and phase coherence lengths seem quite similar. Although we see no reason that these should be related, it is an interesting question if there is underlying physics behind this observation.

Unlike the spin relaxation length, the spin relaxation time is a more universal figure of merit that can be compared among different devices and materials as it does not depend on the diffusion constant. The spin relaxation time is found to be relatively fast, $\sim 2 - 3$ ps (Fig. 3.3b). Recent reports on pump-probe spectroscopy on monolayer WS$_2$ have also shown fast intravalley spin-flip rates [82]. Furthermore, we find that the spin relaxation time is independent from the density. We consider two counteracting effects that can explain this observation. Firstly, according to the theoretical work of Wang *et al.* [80] the intravalley spin-flip processes are dominated by electron-electron Coulomb scattering. As the electron density increases, the spin-flip rate should thus decrease. The spin-relaxation rate can also be tuned due to breaking of inversion symmetry in centrosymmetric TMDCs [83, 84]. The electric-field of the back-gate can polarize the two layers and therefore break the inversion symmetry of the system. In the case of our devices though, the inversion symmetry is already broken for the range of the back-gate voltages applied [61, 85] and should not affect the spin relaxation rate. The second mechanism tends to increase the spin relaxation rate through the Bychkov-Rashba SOC [86, 87]. These two mechanisms could counteract each other resulting in a relaxation time independent on n. For very large electric-fields, the Bychkov-Rashba SOC dominates and the in-plane and momentum-locked effective B-field becomes strong enough to drive the system to WAL by spin-flip intervalley scattering [38, 69, 83, 88].

In addition to the HLN model that has been typically used for the analysis the experiments of WL and WAL in MoS$_2$ [67–69], a specific model was recently developed for the analysis of of WL and WAL in monolayer TDMCs, which takes into account the inter-

play of the SO interaction and the multiple valleys in the band structure of TMDCs [38]. The model developed by H. Ochoa *et al.* and contains four free parameters (B_ϕ, B_s, B_e and B_λ). In the parameter range applicable to our measurements, however, we find that the parameters of the model are too strongly cross-correlated to provide a meaningful analysis of our data (see Fig. 3.11) We do note, however, that with similar parameters as found in the HLN fit, the model of [38] does provide a theoretical prediction of the WL that is in agreement with our observations (see supplemental material for the quality of the fittings as well as results from the fitting).

3.3. Conclusion

In summary, we have studied weak localization effects in h-BN encapsulated bilayer MoS$_2$ devices for different temperatures and electron densities. Based on the analysis of the HLN theory, we found large phase-coherence lengths limited by electron-electron inelastic scattering. The spin relaxation rate is found to be relatively fast and independent from electron density. This latter observation may indicate the presence of counteracting relaxation mechanisms involving electron-electron scattering and spin-orbit interaction.

3.4. Supplemental material

3.4.1. Electronic transport and device characteristics

The fabrication scheme that was used in this study provided ohmic behavior at cryogenic temperatures in the devices as shown in Fig. 3.5a. This verifies the low contact resistance in the devices. Both D1 and D2 devices exhibit a metallic behavior at the range of the applied back-gate voltages, as indicated by the fact that the resistivity (conductivity) of the channel decreases (increases) when the temperature decreases. Figure 3.5b shows the conductivity of sample D1 as function of back-gate voltage for various temperatures.

The carrier density was obtain via Hall measurements at different temperatures. The capacitance per unit area (C) is found equal to ~15 nF/cm^2, a value close to the predicted one from the parallel plate capacitor model for a 285 nm SiO$_2$ and 30 nm h-BN dielectrics 11 nF/cm^2, assuming a dielectric constant $\epsilon_r = 4$ for both dielectrics. The Hall mobilities (μ) were calculated using the Drude relation $\sigma = ne\mu$, while the field-effect mobilities where obtained from the linear fit of the conductivity versus gate voltage characteristics and using the relationship $\mu = \frac{1}{C} \frac{\Delta\sigma}{\Delta V_g}$.

Moreover, we studied the scattering mechanism in the devices (Fig. 3.5c). We find that at moderate temperatures the mobility increases upon cooling and the scattering is dominated by optical phonons, indicated by the value of the γ that is equal to -1.3, very close to theoretical prediction for monolayer [89]. At low temperatures the mobility is nearly independent of the temperature, which is a signature of scattering from impurities [90].

3
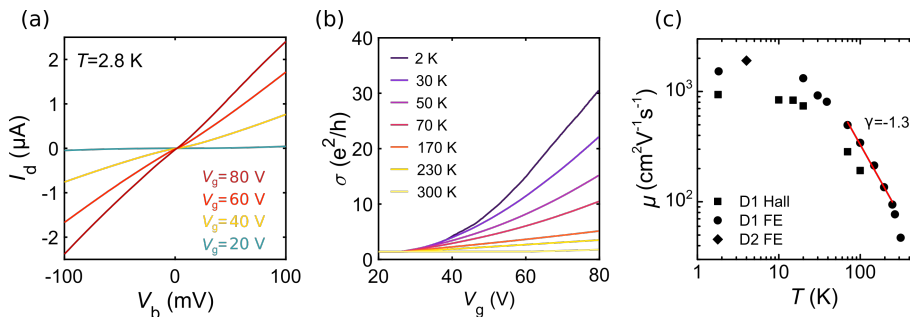
Figure 3.5: Transport characteristics of the bilayer MoS$_2$ van der Waals heterostructures.(a) Two-probe current-voltage characteristics at different back-gate voltages at 2.8 K. (b) Conductivity σ as a function of the back-gate voltage V_g for different temperatures.(c) Dependence of the electron mobilities μ from the temperature based on field-effect and Hall measurements. The values of Hall mobilities are for electron density of 7.7×10^{12} cm^{-2}. The red line corresponds to the linear fit to the data that yields a slope of -1.3, characteristic for optical-phonon scattering.

3.4.2. PHOTOLUMINESCENCE SPECTRUM

In order to verify that the thickness of the MoS$_2$ flakes corresponds to that of a bilayer we have measured their photoluminescence spectrum. Figure 3.6 shows the photoluminescence spectrum os the sample D1. As it can me seen this corresponds to the spectra of a bilayer MoS$_3$ flake according to earlier reports [24]. The peaks with the letters N, A and B, correspond to photon emission that originates from the indirect bands gap as well of the two distinct excitons of the direct gap, respectively.

3.4.3. WEAK LOCALIZATION IN SAMPLE D2

We have performed magnetotransport in sample D2 and we have observed weak localization effects as well. In this case we have taken datasets at gate voltages of 50 V and 60 V. Figure 3.7 presents the magnetoconductivity at 3.2 K, included the fitting with the HLN model. We believe that the deviation of the data from the fit is due to a jump in the gating of the channel due to an unstable gating effect. From the fitting we have obtain the values of L$_\phi$, τ_ϕ, L$_s$ and τ_s. Figure 3.8 shows the results for two different electron densities. The values are very similar to the ones that we obtained for sample D1 and presented in the main text.

3.4.4. BEHAVIOR OF THE FITTING PARAMETERS IN THE MODEL OF OCHOA *et al.* AND IN THE HLN MODEL

The model of Ochoa *et al.* that addresses quantum interference of electrons in TMDCs , is being used for the first time in the current report and we have to investigate it's behavior. The model (for $E_F > \lambda$ in the "clean" limit) contains four free parameters: magnetic
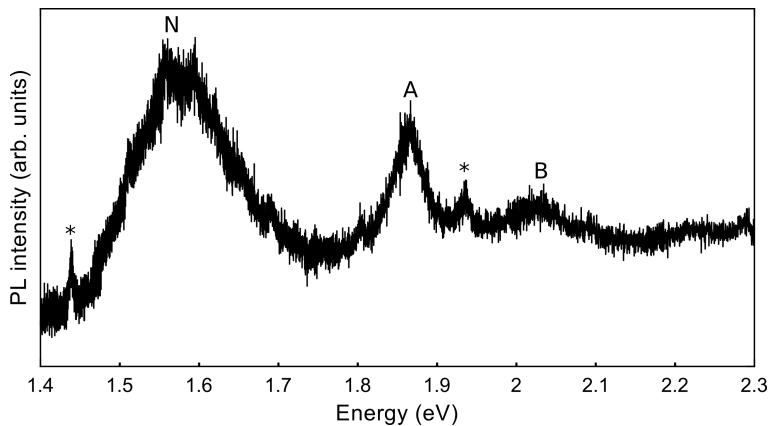
Figure 3.6: Photoluminescence spectrum of sample D1. The spectrum corresponds to bilayer MoS_2 [24]. The A, B letters indicate the A, B excitonic peaks of the direct transitions, while the N corresponds to indirect transitions. The stars (*) indicate peaks of unknown origin, which are possibly associated with defect or impurity luminescence from the MoS_2 according to previous reports [24].
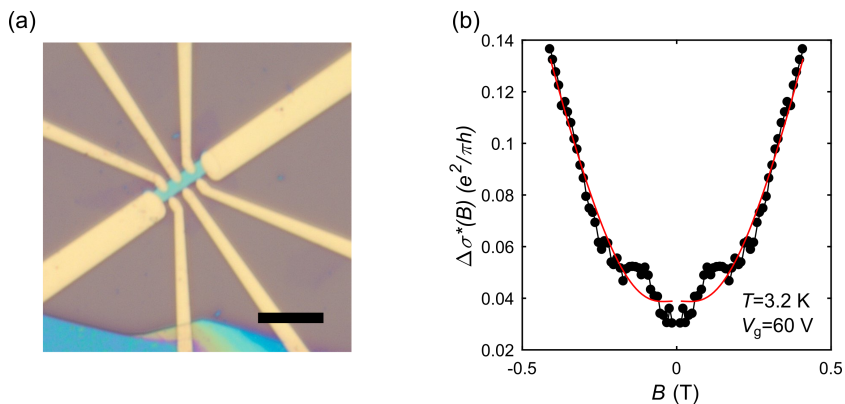
Figure 3.7: Weak localization in sample D2. (a) Optical image of sample D2. Scale bar is 10 μ m. (b) Magnetoconductivity of sample D2 at $T = 3.2$ K and $V_g = 60$ V. The red line corresponds to the fitted curve with the HLN model.
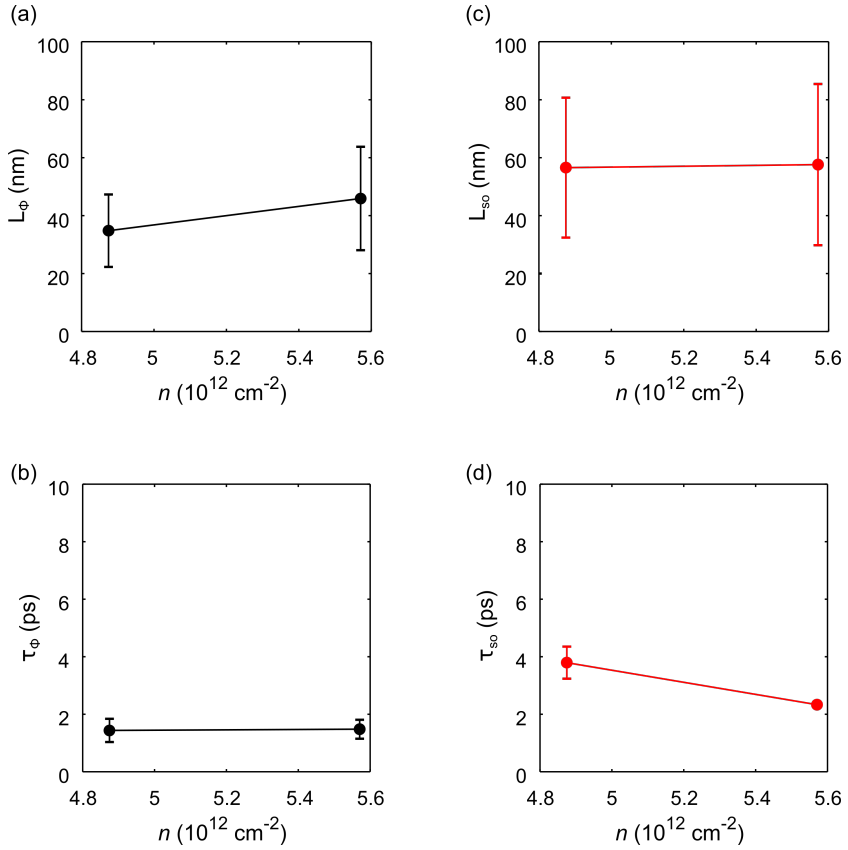
Figure 3.8: Results from the analysis of weal localization in sample D2 at $T = 3.2$ K. Phase coherence length (a) and time (b) and spin relaxation length (c) and time (d), as a function of the electron density. The error bars have been obtained using uncertainty propagation methods.

fields associated to the phase coherence length (B_ϕ), the momentum relaxation length (B_e), the spin-flip length (B_s) and length associated to the SO splitting of the bands (B_λ). In our analysis we have reduced the number of the parameters by one, due to the use of the momentum relaxation length from the transport data. Nevertheless, even three parameters in the model is a large number in order to have an accurate determination of the specific properties of the system. Therefore the uncertainty in the parameters can get very large values.

In a new function that is being used to fit a specific curve is useful to study how many minima of the residual sum squares (RSS or χ^2) exist in the parameter space. This allows us to verify whether a specific set of values can result from the fitting process or there are more sets of values that have same values of χ^2. In Fig. 3.9 we have plotted the χ^2 as a function of values of B_ϕ and B_s, for the case of the model of Ochoa *et al.* (Fig. 3.9a) (the expression of the model is presented in the next section) and for the Hikami-Larkin-Nagaoka model (Fig. 3.9b). According to Fig. 3.9a the χ^2 has minima across a line and therefore the two parameters are cross-correlated. On the other hand the HLN model has one global minimum of the χ^2. So in the case of the Ochoa model the initial conditions as well as any boundaries can affect the result of the fitting.
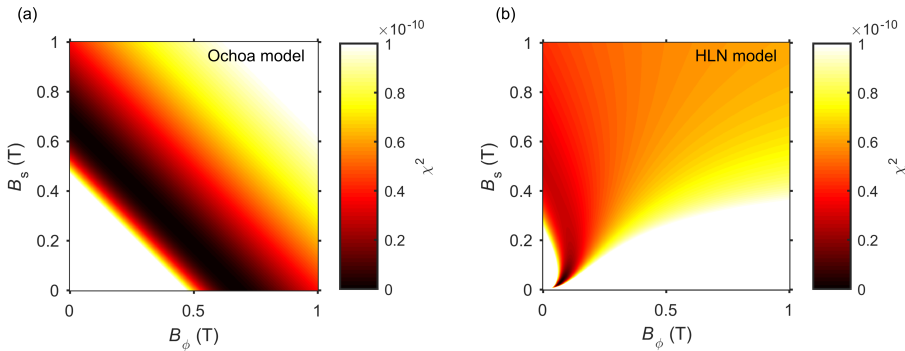
Figure 3.9: Residual sum squares (χ^2) as a function of B_ϕ and B_s for the model of Ochoa (a) and for the HLN model (b) for a specific data set ($V_g = 65$ V).

3.4.5. ANALYSIS OF THE DATA WITH THE MODEL OF OCHOA *et al.*

Although as we described above the model of Ochoa *et al.* has cross-correlated parameters, we will try to obtain some estimates by applying some boundaries. The condition that we apply is $B_f < B_s$, so that the phase coherence length is lager than the mean free path. Also, in order to avoid "biasing", we used initial values outside the bounds of the fitting parameters. For K/K' electrons with finite splittings and with the Fermi level above the SO splitting, the magnetoresistance is then given by [38]:
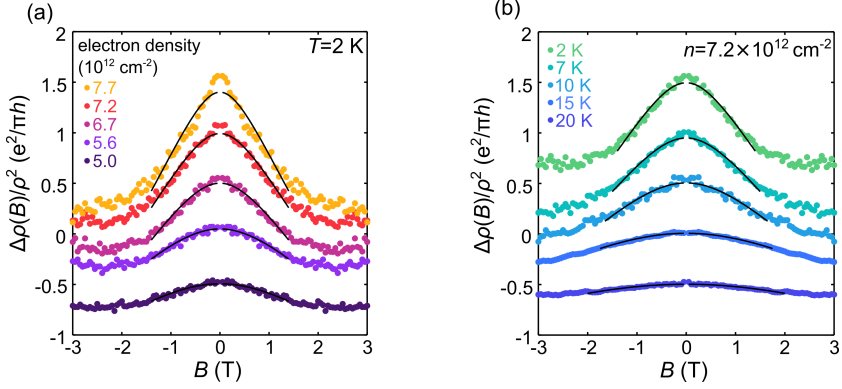
Figure 3.10: Symmetrized magnetoresistance $\Delta\rho(B)/\rho^2$ as a function of magnetic field B for different electron densities n measured at $T = 2$ K. (b) Symmetrized magnetoresistance as a function of magnetic field for different temperatures with $n = 7.2 \times 10^{12}$ cm^{-2}. The drawn solid black lines correspond to fits using Eq. (3.2). Data and curves have been shifted vertically by $0.5 e^2/\pi h$ for clarity.

$$\frac{\Delta\rho(B)}{\rho^2} = -\frac{2e^2}{\pi h}\left\{2F\left(\frac{B}{B_\phi+B_s}\right) + \frac{1}{\sqrt{1-\frac{B_e B_\lambda}{B_s^2}}} \times G\left(\frac{B}{B_\phi+B_s+B_\lambda}, \frac{B}{B_s\sqrt{1-\frac{B_e B_\lambda}{B_s^2}}}\right)\right\}, \quad (3.2)$$

with

$$G(z_1, z_2) = \sum_\pm \left[\pm\psi\left(\frac{1}{2}+\frac{1}{z_1}\pm\frac{1}{z_2}\right) \mp ln\left(\frac{1}{z_1}\pm\frac{1}{z_2}\right)\right]. \quad (3.3)$$

Here $F(z) = \psi(1/2 + 1/z) + ln(z)$. In the particular form we have considered mainly Dyakonov-Perel processes in the SO induced Zeeman term. Fitting to the experimental data are shown in Fig. 3.10 with black solid lines. The fitting is satisfactory for the most cases, but at high densities the fitted curves do not follow the data that well.

From the fitting we find that the phase coherence length has values that range between 30 and 40 nm for the lowest temperature and the mechanism of dephasing is also the Altshuler one as in the case of the analysis with the HLN model. On the other hand the spin relaxation length and time are small. Nevertheless the dependence from the density is the same with what we found with the HLN model. That is, an independent from density spin diffusion time and a linear increase of the spin relaxation length. We have not added the error bars in this case, due their large magnitude.

3.4.6. UCFs IN THE MAGNETOCONDUCTIVITY OF SAMPLE D1

The magnetoconductivity curves show oscillations at high magnetic fields. These oscillations are related to universal conductance fluctuations (UCFs) and not from Shubnikov de Haas type of oscillations. UCFs appear in samples with finite disorder as a result
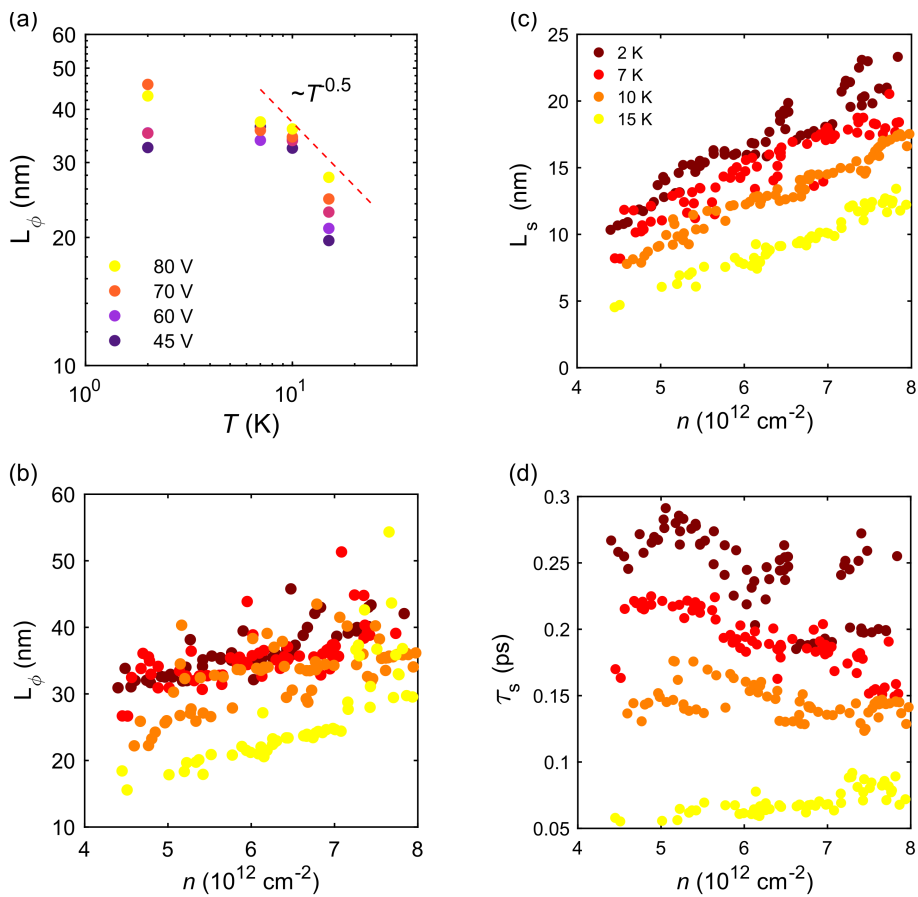
Figure 3.11: Results obtained from fitting the magnetoresistance data to Eq. (3.2). The spin relaxation length increases with electron density .(a) Phase coherence length as a function of temperature for different back-gate voltages in logarithmic scale. (b) Phase coherence length as a function of electron density for different temperatures (b). Spin relaxation length L_s (c) and time τ_s (d) as a function of the electron density for different temperatures.

of change in the relative phase of the different trajectories during their interference, as a result to changes in the impurity configuration, chemical potential or magnetic field (change of the magnetic flux that penetrates the path). As mentioned above, the period of the oscillations is $\Delta B \approx 1.2 - 2$ T, which can be translated in a coherence length of 50-63 nm using th relationship $\Delta B = (\hbar/e)/(\pi r)^2$.
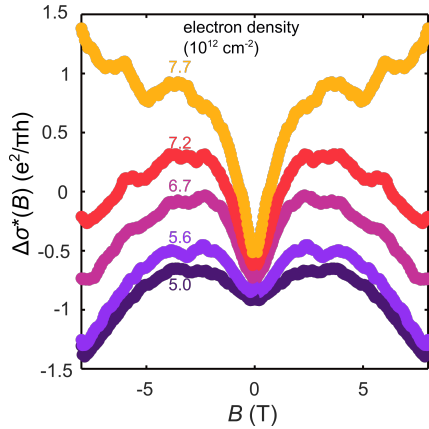
Figure 3.12: Extended version of Fig. 3.2b from the main text, where the UCFs can be seen more clearly. the curves are also shifted by $0.1 e^2/\pi h$.

4

MULTI-TERMINAL ELECTRONIC TRANSPORT IN BORON NITRIDE ENCAPSULATED TiS$_3$ NANOSHEETS

In this chapter we study electrical transport as a function of carrier density, temperature and bias in multi-terminal devices consisting of hexagonal boron nitride (h-BN) encapsulated titanium trisulfide (TiS$_3$) sheets. Through the encapsulation with h-BN, we observe metallic behavior and high electron mobilities. Below 60 K an increase in the resistance, and non-linear transport with plateau-like features in the differential resistance are present, in line with the expected charge density wave (CDW) formation. Importantly, the critical temperature and the threshold field of the CDW phase can be controlled through the back-gate.

4.1. Introduction

Titanium trisulfide (TiS$_3$) is a van der Waals semiconductor with a direct band gap of ~1 eV. It has a crystal structure with Ti-S bond lengths longer in the *b*-direction than in the *a*-direction, and is built of 2D sheets that are usually elongated along the *b*-axis. The one-dimensional chain-like lattice of TiS$_3$ is responsible for the large optical and electronic in-plane anisotropy [91, 92]. The anisotropic features along with the high mobilities and photo-response have established TiS$_3$ as a promising candidate for transistors [93–95] and polarization sensitive photodetectors [96, 97]. Furthermore, theoretical studies have suggested that monolayer TiS$_3$ has very high mobilities at low temperatures [98], rendering this material promising for studying quantum transport phenomena.

The electrical properties of bulk TiS$_3$ whiskers have been studied by Finkman *et al.* [99] and later on by Gorlova *et al.* [100, 101] who showed that TiS$_3$ exhibits semiconducting behavior (resistance decreases with temperature) and below certain temperatures (57 K and 17 K) it undergoes a transition to a charge-density-wave (CDW) state due to Peierls instability. Similar behaviors were also found for other members of the family of the transition metal trichalcogenides (TMTCs) like NbSe$_3$ [102] and ZrTe$_3$ [103]. Very recently, the electrical properties at different temperatures of field-effects devices from TiS$_3$ nanoribbons were studied [104, 105]. Similar to other 2D semiconducting systems like MoS$_2$ [106] and WSe$_2$ [107] on SiO$_2$, the devices showed disorder induced electron localization even at high temperatures and high carrier densities. Moreover, degradation during the fabrication should not be excluded as TiS$_3$ could form vacancies and oxidize under atmospheric conditions even at moderate temperatures [108].

In this chapter we present results on electrical and multi-terminal transport on multi-terminal TiS$_3$ devices. Via encapsulation with hexagonal boron nitride (h-BN), we eliminate extrinsic sources of disorder and measure the intrinsic properties of this material. We study the conductivity (sheet resistance), the mobility and the current-voltage relationship as a function of temperature and electron density.

4.2. Results and discussion

4.2.1. Heterostructure assembly

The boron nitride encapsulated TiS$_3$ heterostructures were fabricated using the van der Waals pick-up technique with polypropylene carbonate (PPC) films [73]. Prior to the stacking process, the top h-BN was pre-etched using a rich-in-CHF$_3$ gas reactive ion etching (RIE) process in order to deposit top metallic contacts (for more details see *methods* section) [109]. This way the channel is always protected during the device fabrication procedure. The elongated flakes were aligned so the long edge is parallel to the biasing direction. The final stacks were deposited on Si/SiO$_2$ substrates, where the carrier density can be tuned by the Si back-gate. A schematic of the device cross-section is shown in Fig. 4.1a. We fabricated two devices of thickness 26 and 9 nm, labeled as D1 and D2, respectively. In the main text we focus on results from sample D1 (inset of Fig. 4.1d). Very similar results on the conductivity and mobility were obtained from sample D2 and can be found in the supplemental material.
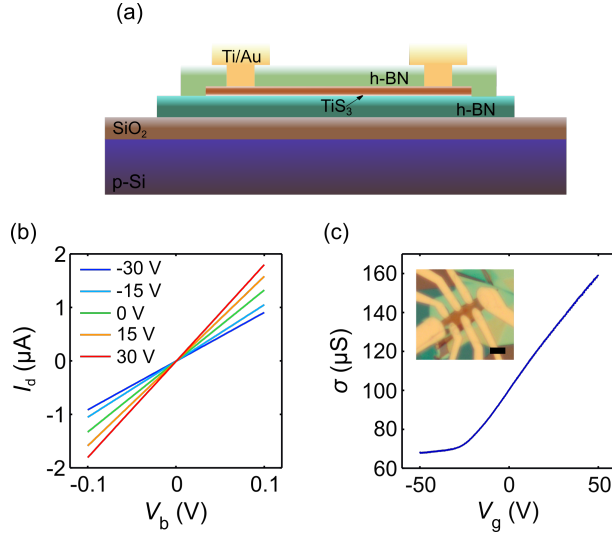
Figure 4.1: Device schematic and room temperature electrical characteristics. (a) Schematic illustration of the cross-section of a device consisting of a TiS_3 sheets encapsulated with h-BN. The Ti/Au contacts were deposited on TiS_3 through prepatterned windows on the top of the h-BN. (b) Current-voltage characteristics from two-terminal measurements for different back-gate voltages. (c) Conductivity from four-terminal measurements as a function of the back-gate voltage. Inset shows the device that was used for the measurements (sample D1). Scale bar corresponds to 3 μm.

4.2.2. ELECTRICAL TRANSPORT AT ROOM TEMPERATURE

Room-temperature electrical characterization in a two-terminal configuration verified the ohmic contacts from the drain current-voltage bias ($I_d - V_b$) characteristics at different back-gate voltages (V_g) (Fig. 4.1b). Using four-terminal measurements we obtain the intrinsic conductivity as a function of the back-gate voltage (Fig. 4.1c). We find an n-type semiconducting behavior similar to earlier reports [91, 94, 105]. The ON/OFF ratio appears to be small ~ 2.3, while the threshold voltage is about -30 V from the onset of conductivity, indicating that large residual doping is responsible for the large current in the OFF state, in agreement with previous studies [94]. The room-temperature field-effect mobility, was calculated based on the relationship $\mu_{FE} = d\sigma/(C_g^{FE} dV_g)$, where C_g^{FE} is the gate capacitance determined by the parallel plate capacitor model and σ is the 2D or sheet conductivity. The mobility is found to be equal to 54 and 122 cm^2/Vs for two- and four-terminal measurements, respectively. These mobilities are the largest reported so far for TiS_3 [93, 94, 105].

4
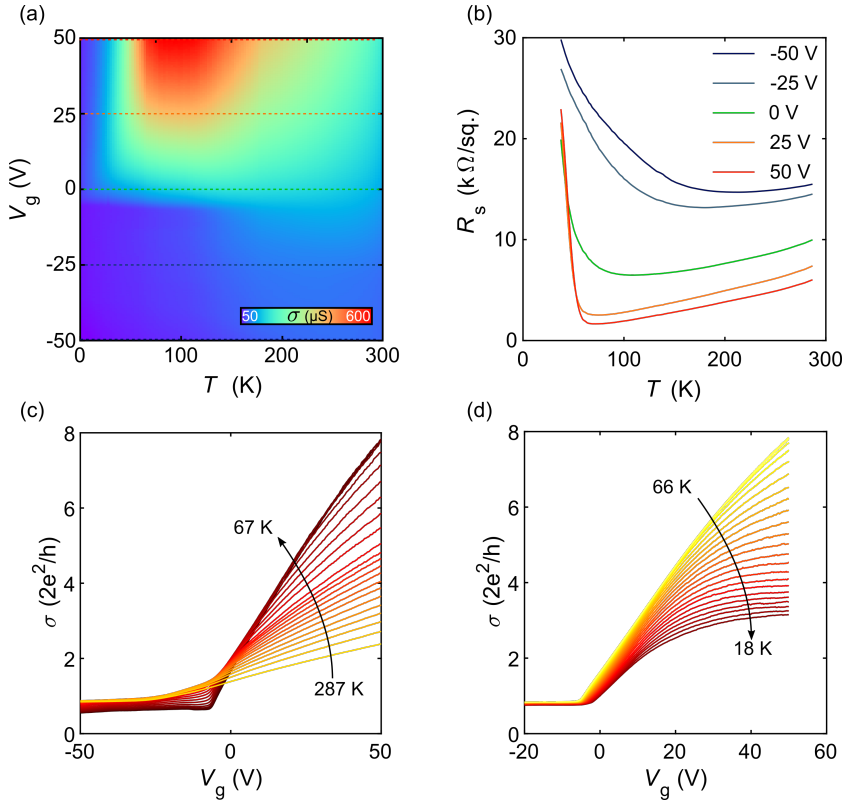
Figure 4.2: Temperature and gate dependence of the conductivity (sheet resistance). (a) Colormap of the conductivity as a function of the temperature and the back-gate voltage. The horizontal dashed lines correspond to the temperature sweep traces at constant gate voltages of the sheet resistance that are plotted in panel (b). (b) R_s *vs.* T for different back-gate voltages. Transfer characteristics for temperatures between 67 and 287 K in (c) and between 18 and 66 K in (d). The dataset of panels (a) ,(b) and (c) was obtained using $I = 100$ nA, while the dataset in panel (d) was obtained with $I = 20\,\mu$A.

4.2.3. TEMPERATURE DEPENDENCE OF THE SHEET RESISTANCE AND CONDUCTANCE

In order to investigate the conducting mechanism in the devices, we obtained the conductivity as a function of back-gate and temperature using multi-terminal DC measurements at finite current bias (Fig. 4.2a). A decrease of the sheet resistance with the decrease of the temperature is observed, which is a signature of metallic behavior at all back-gate voltages. Nevertheless, below certain temperatures (which range between 70 and 150 K, depending on the charge carrier density) the sheet resistance starts to increase, which is a signature of insulating behavior (Fig. 4.2b). For negative gate voltages this up-turn takes place at high temperatures around 150 K. This behavior can be ex-
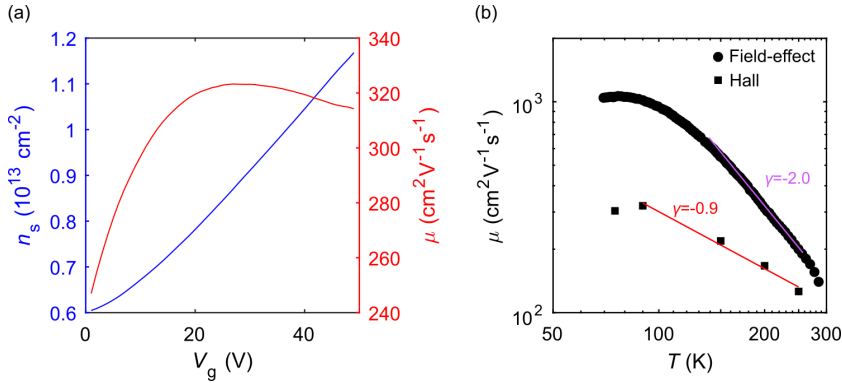
Figure 4.3: Mobility of device D1. (a) Electron density from Hall measurements and mobility as a function of back-gate voltage at $T = 66$ K. (b) Logarithmic plot of the mobility as a function of the temperature for different carrier densities. At high temperatures the dependence is approximately linear following a power law dependence $\mu \propto T^{\gamma}$. (c) Dependence of the coefficient γ on the electron density. The shaded grey curve represents the uncertainty in the parameter γ.

plained by a Fermi level alignment below the conduction band or mobility edge and when the temperature decreases the thermally excited carriers freeze out. For zero and positive gate voltage values we observe a metal-to-insulator-transition (MIT) at lower temperatures, but the resistance increase is more abrupt for higher gate voltages. This could be attributed to Mott-insulating behavior or more probably due to a CDW transition as expected at this temperature range for TiS_3 [100, 101]. From the transfer characteristics, we observe that the conductivity increases with the decrease of the temperature down to 67 K for positive gate voltages (Fig. 4.2c). The threshold voltage that is the back-gate voltage at which the conductivity starts to increase, shows a strong temperature dependence as a consequence of the aforementioned carrier freeze-out. Below 67 K the conductivity starts to drop and as the temperature decreases; the transfer characteristic show a sublinear 'bending', indicating enhancement of the insulating state at higher electron densities (Fig. 4.2d).

4.2.4. HALL AND FIELD-EFFECT MOBILITY

In semiconductors and metals one of the most important figures of merit is the carrier mobility, and to calculate it from the conductivity based on the Drude model, the carrier density should be known. To obtain the carrier density, we performed Hall measurements at various temperatures (75, 90, 150, 250 K). Figure 4.3a shows the carrier density, which increases in a linear way with the back-gate voltage; it equals 6-12×10^{12} cm^{-2} for V_g=0-50 V. From this measurement we obtain a capacitance per unit area of 1.9 ×10^{-4} F/m^2, which is larger than the estimated one from the parallel plate capacitor model (1.2 ×10^{-4} F/m^2, for ϵ_{hBN} = 4). Based on the Drude formula $\sigma = n_H e \mu_H$, where e the electron charge, n_H the electron Hall density and μ_H the Hall mobility, we calculate the Hall mobility as a function of the back-gate voltage. At 90 K, μ_H is found to be between

250 and 330 cm^{2}V^{-1}s^{-1} for $V_g = 0-50$ V (Fig. 4.3a). This result demonstrates that the device exhibits high electron mobilities due to the encapsulation with h-BN, although the mobilities are lower than those of TMDCs and black phosphorus when using similar encapsulation techniques [18, 110, 111]. Also, the large residual density for $V_g = 0$ V, shows that the TiS$_3$ sheet contains a large density of impurities that probably originates from sulfur vacancies as in the case of the TMDCs [112–114], thereby limiting the mobility in the device.

The mobility usually depends on the temperature with a power law: $\mu \propto T^\gamma$. The value of the coefficient γ can reveal the dominant scattering mechanism of the electrons. A γ in the range of -0.5 and below, is a signature phonon scattering [115]. At very low temperatures, γ can approach 0 (mobility independent from temperature), which is the case of impurity scattering for degenerate semiconductors, while in non-degenerate semiconductors with substitution doping $\gamma = 3/2$ [116, 117]. In Fig. 4.3b, we plot on a logarithmic scale the field-effect and the Hall mobilities (for $n_H = 9 \times 10^{12}$ cm^{-2}) as a function of the temperature from 280 to 75 K. The Hall mobility was calculated based on the Drude formula as mentioned above, while the field-effect mobility was obtained from the transconductance through the relationship $\mu_{FE} = \delta\sigma/(C_g^{FE}\delta V_g)$, with a linear fit in the σ-V_g plots of Fig. 4.2c around $V_g = 0$ V. From the linear fit of the data in this $\log_{10}(\mu)$ $vs.$ $\log_{10}(T)$ plot, we obtain the coefficient γ in the temperature range of 90 to 280 K. The value of γ is -0.9 and -2.0 for the Hall and field-effect mobilities, respectively, indicating phonon scattering at this temperature range [115]. As found usually, the Hall mobility is 2-3 times smaller than the calculated field-effect mobility [111, 118]. We attribute this discrepancy to the Hall scattering factor that can be different than unity [68, 119] and is defined as $r_H = \mu_H/\mu_{eff}$ where μ_{eff} is the effective or drift mobility, or equivalently $r_H = C_g^{FE}/C_g^H$, with C_g^H the capacitance per unit area based on Hall measurements. The Hall scattering factor in this case is found to be equal to 0.9 at 250 K and decreases to 0.6 at 90 K.

4.2.5. NON-LINEAR TRANSPORT

Metal-insulator transitions (MIT) or charge density wave (CDW) transitions are usually associated with non-linear transport with distinct characteristics. In the case of CDW, the lattice rearranges due to a Peierls instability and an electronic gap opens at the Fermi level due to the formation of the standing electron wave [120]. Pinning of the CDW to impurities leads to bias dependent transport. In the differential resistance a plateau appears around zero bias and above a critical field depinning leads to an abrupt decrease of the differential resistance. MITs, on the other hand, originate from carrier localization due to strong disorder. In this case hopping of electrons is strongly temperature and electric field dependent [121].

Figure 4.4a presents voltage-current bias (V_p-I) curves for $V_g = 50$ V from four-terminal measurements that show almost linear behavior for high temperatures, but below 66 K they become strongly non-linear. In the differential resistance a strong peak at low current bias is evident, which forms a plateau upon lowering the temperature (Fig. 4.4b). Figure 4.4c shows I-V_p characteristics for different gate voltages at $T=4$ K. The shape of the V_p-I curves shows clear signatures of a CDW phase as in the case of NbSe$_3$ [122, 123]. From the differential resistance the critical (or threshold) electric-field of the sliding
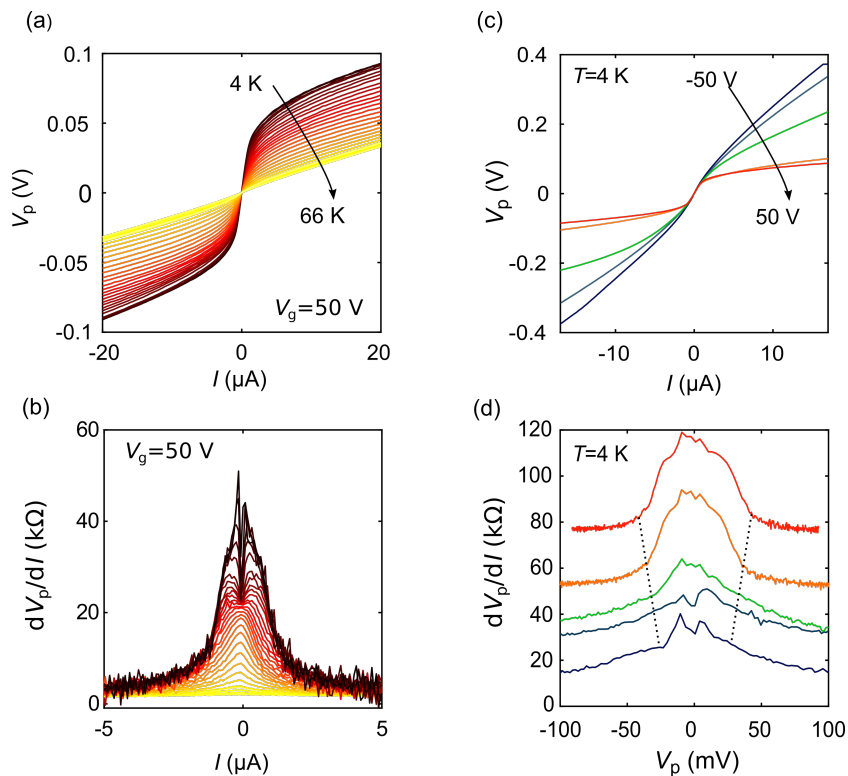
Figure 4.4: Low-temperature non-linear transport properties. Probe-voltage (a) and differential resistance (dV_p/dI) (b) as a function of the current bias for different temperatures below 67 K for $V_g = 50$ V. (c) $V_p - I$ characteristics for different gate voltages at $T = 4$ K. (d) Differential resistance as a function of the probe-voltage for the same gate voltages and temperature as in (c). The curves have been shifted vertically for clarity. Dashed lines indicate the critical voltage (E-field) of the sliding CDW.
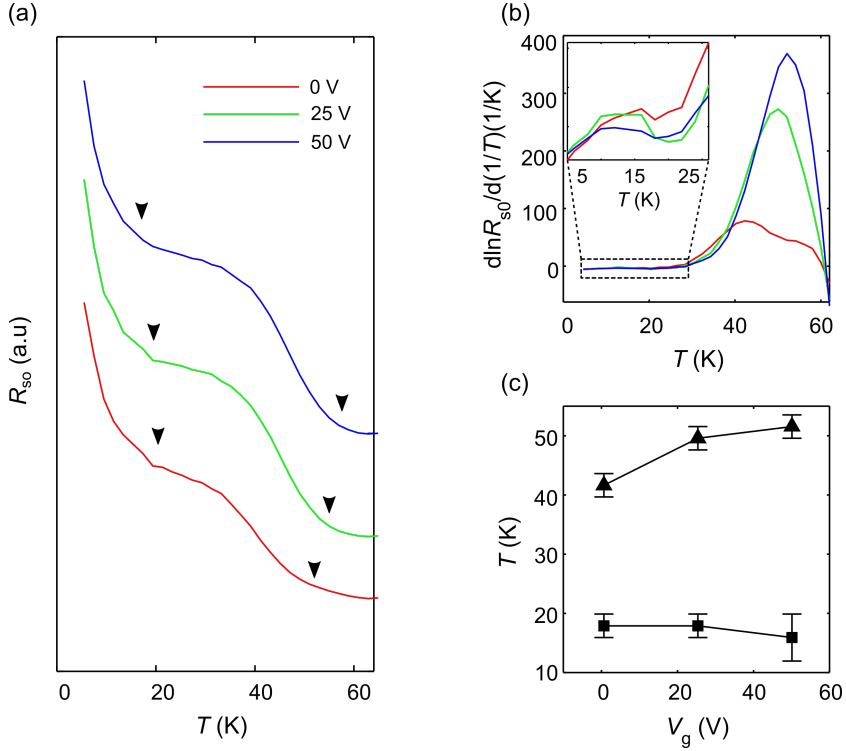
Figure 4.5: CDW analysis of resistance versus temperature curves. (a) Temperature dependence of the zero-bias differential resistance (R_{s0}) for different gate voltages. The curves have been shifted vertically for clarity. (b) $d(\ln R_{s0})/d(1/T)$ $vs.$ T. From the inflation point the critical temperatures associated with the CDW have been determined. The inset shows a zoom of the dashed area at the low temperature regime, where a second inflation is present. (c) Critical temperatures as a function of the gate voltage.

CDW estimated to be 120 V/cm for V_g = 50 V, where the transition can be seen more clearly (Fig. 4.4d). For lower gate voltages the I-V_p characteristics indicate a reduction of the critical field but as the curves are more smeared, it is difficult to extract accurate values.

4.2.6. CHARGE DENSITY WAVE ANALYSIS

Since the non-linear current-voltage curves indicate a CDW phase, we will follow with an analysis that is usually carried out to investigate the critical temperature of the CDW transition. The zero bias differential resistance (R_{s0}) as a function of T for three different gate voltages is plotted in Fig. 4.5a. A cusp is present at temperatures of ~ 60 K, followed by an increase in the resistance and a second cusp just below 20 K indicating the presence of two transitions shown by the arrows. Such anomalies in the differential resistance are evidence for a CDW transition due to the formation of the gap and have

been observed for different materials [124, 125]. For higher bias features of CDW vanish (Fig. 4.11) [126]. Plotting the logarithmic derivative $d(\ln R_{s0})/d(1/T)$ vs. T the CDW, the transition temperature can be determined from the maximum of the curves (Fig. 4.5b). There is a clear peak-like shape curve with a maximum around 60 K and zooming-in around 20 K there is a small bump visible (inset of Fig. 4.5b). Figure 4.5c presents the dependence of the temperatures of the two transitions on the back-gate voltage. The first transition exhibits an increase from 42 K to 52 K when the gate voltage increases from 0 to 50 V. In bulk samples and along the b-direction the critical temperature was found equal to be 59 K [101], close to the values obtained here. Such modulation of the transition temperature was also found in $NbSe_2$ and TaS_2 recently [127]. On the other hand, the second transition, which is found around 22 K for $V_g = 0$ V shows a weak gate dependence and drops to 19 K at $V_g = 50$ V. Since the uncertainty of this critical temperature is large, we cannot determine with certainty whether it increases or decreases with the back-gate voltage.

Sample D2 also shows signatures of CDW at positive gate voltages (see Supp. Info for the analysis). There are non-linear current-voltage characteristics, and for small values of V_g the dV_p/dI exhibit a zero bias peak-like feature in the differential resistance. At $V_g = 80$ V a clear plateau appears with a critical electric field of 112 V/cm, in agreement with sample D1. The bias dependent differential resistance with a peak structure is a characteristic of hopping transport (E-field dependent hopping) [128]. Following the same analysis for finding the T_{CDW} with sample D1, we find one critical temperature from the maximum of the curve in the $d(\ln R_{s0})/d(1/T)$ $vs.$ T plot. For sample D2, the critical temperature lies around ~50 K, similar to the one found in sample D1. The critical temperature however, shows an independence from the gate voltage. Such observation can be attributed to the presence of a MIT close to the CDW transition, therefore resulting in such weekly dependent on the gate voltage critical temperature, as well as superimposed plateaus and peaks in the differential resistance.

4.3. CONCLUSION

In summary, we have studied electrical transport in exfoliated TiS_3 encapsulated in boron nitride. TThe mobilities of our samples are the largest reported for this material, highlighting the encapsulation with boron nitride as a useful approach to improve sample quality. Moreover we found that the thicker sheet shows clear evidence for a CDW transition, while the thinner shows CDW features along with an overlapping MIT. Our results provide clear evidence that quantum phase transitions can be controlled in TiS_3 rendering the particular system interesting to study many-body physics.

4.4. SUPPLEMENTAL MATERIAL

4.4.1. METHODS: GROWTH OF TiS_3, FURTHER DETAILS ON DEVICE FABRICATION AND MEASUREMENT SETUPS

TiS$_3$ growth: The TiS_3 nanoribbons and nanosheets were synthesized by sulfuration of bulk Titanium discs. Titanium discs are vacuum sealed in an ampule with sulfur powder (> 75 atomic % sulfur) and heated to a designated growth temperature (500 ^{o}C). After 20

hours of growth, the ampule is cooled in ambient conditions (see also [91]).

Device fabrication. Flakes of TiS$_3$ (thickness:10-30 nm) and h-BN (thickness:15-30 nm) were exfoliated on substrates of SiO$_2$/Si. The flakes were identified using optical microscopy and investigated with atomic force microscopy and Raman later on. We found that in the case of TiS$_3$, flakes thinner than 10 nm have very small area and they could not be used for multi-terminal devices. The h-BN flakes that would be used as top dielectric were further processed for the opening of the windows for the contacts [109]. We used a polymethyl methacrylate (PMMA) mask and after patterning with electron-beam (*e*-beam) lithography, a reactive-ion-etching (RIE) step etched the holes through the h-BN. The boron nitride h-BN/TiS$_3$/h-BN stacks formed via the van der Waals pick-up technique based on PPC/polydimethylosiloxane (PDMS) stamps. The heterostructures were transferred on top of 285 nm SiO$_2$/Si substrates with delamination at 110 ^{o} C and cleaned with anisole and IPA to remove any polymer residuals. Sample D2 was etched in a Hall bar shape in a CHF$_3$ rich RIE step. For the metal contacts we used a dual layer of 450 A6/950 A3 PMMA resist and after patterning with *e*-beam lithography, Ti/Au contacts were deposited.

Measurement setups. All DC electrical measurements took place in a liquid-He bath cryogenic system, equipped with an 8 T superconducting magnet and in a Montana C2 cryostation.

Growth of the flakes was done by Eduardo Flores, Jose R. Ares, Carlos Sanchez and Isabel J. Ferrer

4.4.2. RESULTS FROM SAMPLE D2

(a)

(b)

(c)
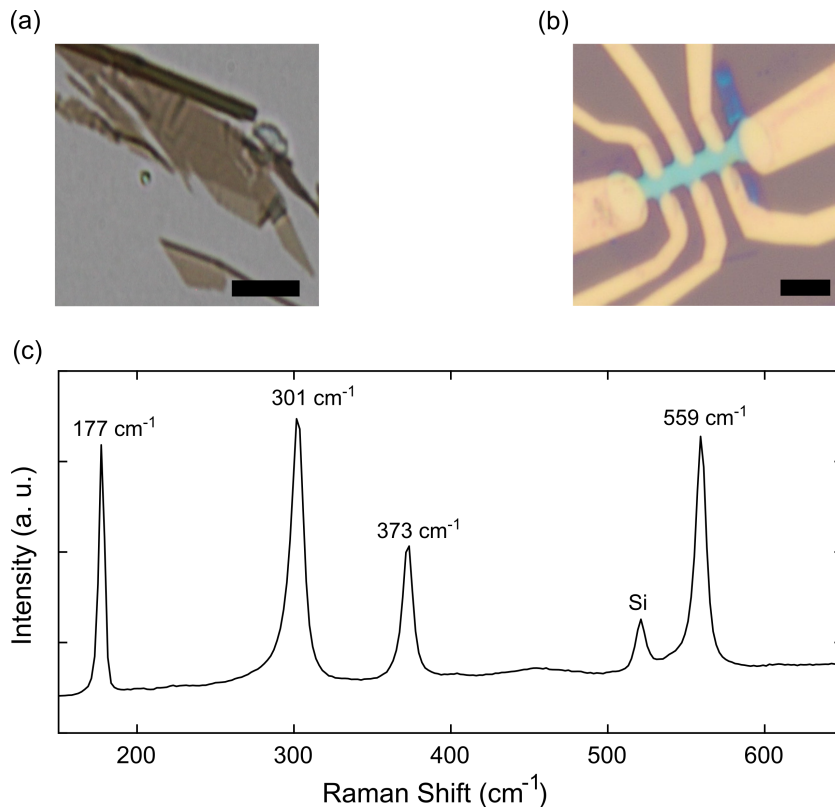
Figure 4.6: Optical image of Sample D2 and Raman spectrum. (a) Optical image (transmission mode) of the flake that was used to fabricate the device D2, sitting on PDMS film. (b) Hall bar device (sample D2) after fabrication. Scale bars are at 4 μm. Raman spectra of a TiS$_3$ flake in the range of 150 to 700 cm^{-1}. The four peaks of the A_{1g} modes of TiS$_3$ along with silicon peak at 520.7 cm^{-1} are visible.

Sample D2, which is thinner than sample D2, showed very similar properties. The device was fabricated with the same way as sample D1 using pre-etched top h-BN. Raman spectroscopy verified that the flakes were consisting from TiS$_3$ and not another allotrope (Fig. 4.6).

Similar to sample D,1 we recorded the four-terminal resistance/conductance as a function of gate voltage for different temperatures, from room temperature down to 4 K (I=20 μA)(Fig. 4.7a). The conductivity has a maximum around ~60 K and then declines as in the case of sample D1. The $R_s - T$ curves show a metallic behavior down to 60 K and below that temperature the sample shows an increase in the R_s (Fig. 4.7b).

The field-effect mobility, which was also calculated using the formula $\mu = \delta\sigma / (C_g^{FE} \delta V_g)$,
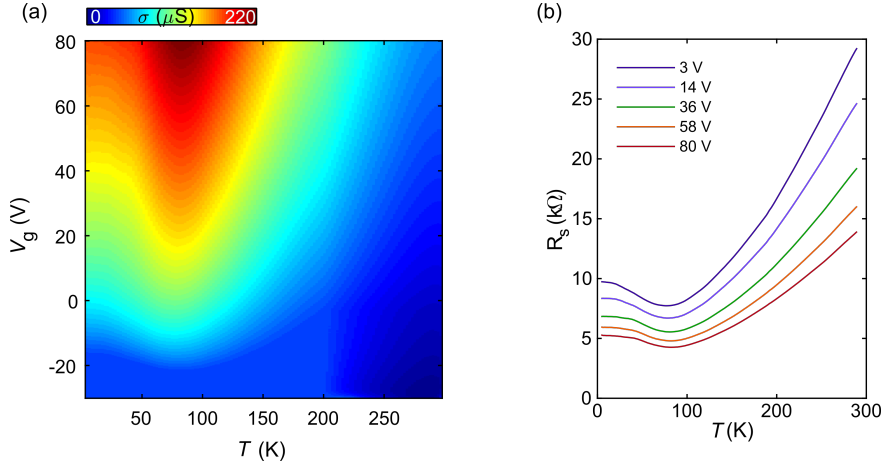
Figure 4.7: a Colormap of the conductivity as function of temperature and back-gate voltage. (b) Sheet resistance as a function of temperature for different gate voltages. The data were obtained with a bias current of 20 μA.

shows a decrease with the electron density (for $T = 90$ K) and it is 330 cm^{2}V^{-1}s^{-1} for V_g=0 V and decreases to 120 cm^{2}V^{-1}s^{-1} for V_g=80 V (Fig. 4.8a). Figure 4.8b shows a logarithmic plot of the field-effect mobility as a function of temperature in the range T=75-200 K. Similar to sample D2 the mobility increases as the temperature reduces and saturates below 80 K, as a result of the CDW transition. The slope of the linear fit at high temperatures yields the parameter γ, which is found to be equal to -1.8; a value close to the one found for sample D1 using the same method (field-effect measurements).

Figure 4.9 shows the differential resistance as a function of the probe-voltage. At the temperature of 4 K and for gate voltages below 80 V the dV_p/dI shows a prominent peak around 0 V, which is a characteristic of localization. At V_g =80 V we observe the plateau until 30 mV along with the superimposed peak at 0 V. This feature is associated with a CDW phase as in sample D1. The threshold field is found equal to 112 V/cm. The observed plateau is increasing as the temperature decreases (Fig. 4.9b).

Carrying out the same analysis as with sample D1, we plot the zero-bias differential resistance as function of temperature for different densities. In this case we observe a monotonic increase of the differential resistance for $T < 60$ K at all gate voltages (Fig. 4.10a). From the maximum of the $d\ln(R_{s0})/d(1/T)$ $vs.$ T, we obtain the temperature where the onset of the increase of the differential resistance (Fig. 4.10b). The critical temperature in this case is independent from the gate voltage (Fig. 4.10c) and can be attributed to a competition of metal-insulator and CDW transition. From Fig. 4.9a based on the plateaus of the dV_p/dI we can conclude that the CDW phase takes place at a temperature close to that of the MIT and similar to the T_{CDW} of sample D1.
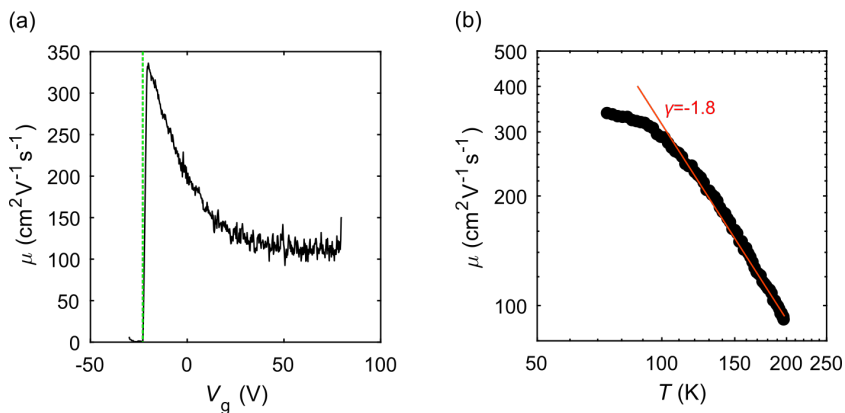
Figure 4.8: Electron mobility in sample D2. (a) Field-effect mobility versus back-gate voltage at T=90 K. The green line indicates the threshold voltage. (b) Logarithmic plot of the field-effect mobility $vs.$ temperature. The linear fit at the high-temperature regime results in the γ coefficient which is -1.8.
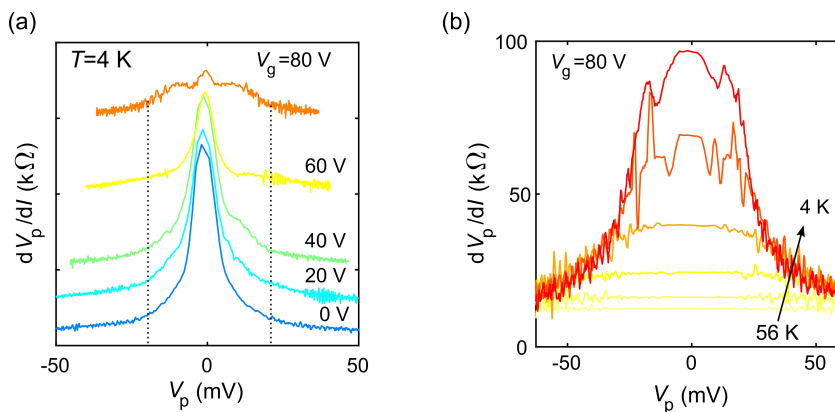
Figure 4.9: Differential resistance as a function of probe-voltage (measured in the four-terminal configuration) for different gate voltages at $T = 4$ K in a and for different temperatures (4 K (red) to 56 K (yellow)) for V_g=80 V in (b). The curves have been shifted vertically for clarity in a.
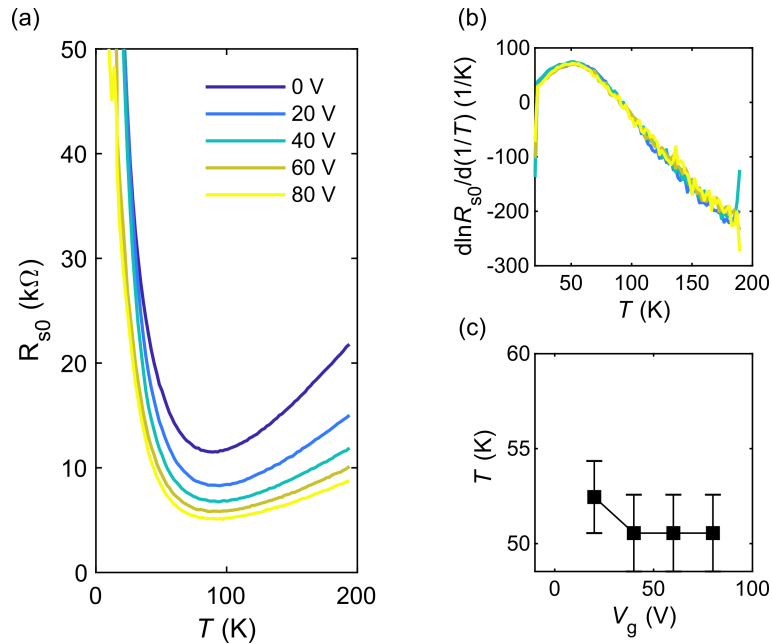
Figure 4.10: CDW analysis in sample D2. (a) Temperature dependence of the zero-bias differential resistance (R_{s0}) for different gate voltages. (b) $\frac{d(\ln R_{s0})}{d(1/T)}$ vs. T. From the inflation point we obtain the critical temperatures associated with CDW transitions. (c) Critical temperature as a function of the gate voltage.

4.4.3. CDW SUPPRESSION WITH CURRENT BIAS

When a sample shows signatures of CDW the bias current or voltage can suppress those signatures [102]. Also in our case we see that when we apply large current bias the resistance of the sample changes and features of CDW get smeared.
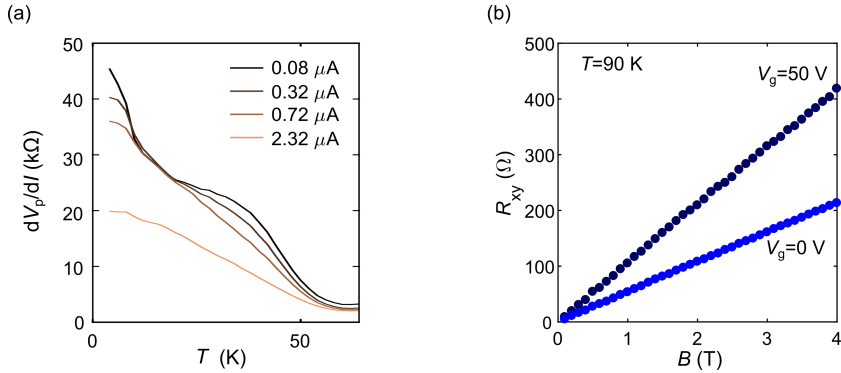
Figure 4.11: (a) Zero bias differential resistance of sample D1 as a function of temperature for different current bias. (b) Hall resistance (R_{xy}) of sample D1 as a function of the magnetic field (B) for two different gate voltages at T=90 K.

4.4.4. HALL RESISTANCE AT 90 K

Figure 4.12 shows the Hall resistance (R_{xy}) as a function of the magnetic field for two different gate voltages at T=90 K. As it can be seen the Hall resistance is linear as a result of a single carrier transport, which is electrons in this case. The electron density was obtained based on the relationship $n = e(\frac{\mathrm{d}R_{xy}}{\mathrm{d}B})$, where the e is the electron charge, and is shown in the main text.

5

EFROS-SHKLOVSKII VARIABLE RANGE HOPPING AND NONLINEAR TRANSPORT IN $1T/1T'$-MoS$_2$

In this chapter we study temperature- and electric-field dependent carrier transport in single flakes of MoS$_2$ treated with n-butyllithium. The temperature dependence of the four-terminal resistance follows the Efros-Shklovskii variable range hopping conduction mechanism. From measurements in the ohmic and non-ohmic regime, we estimate the localization length and the average hopping length of the carriers, as well as the effective dielectric constant. Furthermore, comparison between two- and four-probe measurements yield a contact resistance that increases significantly with decreasing temperature.

5.1. INTRODUCTION

Transition metal dichalcogenides (TMDCs) form a family of van der Waals crystals with the general formula MX_2, where M is a transition metal and X a chalcogen atom. Molybdenum disulphide is the most known among the TMDCs and in its natural form ($2H$ phase) it is a layered semiconductor with a band gap of 1.3 eV in bulk and 1.8 eV in monolayers [130]. $2H$-MoS$_2$ has attracted a lot of interest due to its use in field-effect transistors (FETs) [7], photodetectors [131], and its rich spin-valley physics [132]. Unlike $2H$-MoS$_2$, the $1T$-MoS$_2$ phase has metallic properties and an octahedral stucture [133]. This phase is metastable and relaxes to the distorted $1T'$ one with clustering of the Mo sites and formation of Mo chains [134, 135]. The $1T'$ phase is semiconducting whose band gap has not been measured directly, but calculations yield values ranging from 0.08 eV [136] to 0.8 eV [137].

High doping levels can cause a phase transition from the 2H to the $1T$ and $1T'$ phases, which can be achieved chemically via charge transfer through intercalation of alkali metals [138], by exposure to electron beam irradiation [139] or by metallic adatom adsorption on the surface [140]. This phase transition has been studied extensively and was found to take place with gliding of the sulfur atom planes [141]. Unfortunately, the above processes convert the 2H phase to the $1T$ and $1T'$ phases (1T/1T′), but they also leave some domains of the semiconducting 2H phase inside the MoS$_2$ lattice [142]. Nonetheless, the resulting sheets have very different electronic and chemical properties than the natural 2H-MoS$_2$.

Although there is a large variety of studies on 1T/1T′-MoS$_2$ and related heterostructures, there are not so many investigations on their electrical properties. Recently, temperature dependent two-terminal transport measurements showed that electrons in 1T/1T′-MoS$_2$ from chemical treatment are localized inside the metallic patches of the $1T$ phase, leading to Mott variable-range-hoping (VRH) [143]. Here, we report on four and two-probe measurements on few-layer 1T/1T′-MoS$_2$ flakes, obtained from a n-butyl lithium treatment. We find that the channel resistance increases dramatically as the temperature decreases. Comparison between the two measurement configurations yields a small contact resistance at room temperature that increases considerably at low temperatures. We find that the temperature dependence of the resistance obtained with four terminal-measurements in the ohmic regime fits the Efros-Shklovskii VRH mechanism better than the Mott-VRH model. Furthermore, we study the nonlinear transport at low temperatures with two-probe measurements. While at low bias (ohmic-regime) the temperature dependence of the resistance is strong, at high electric fields this dependence is suppressed and the device operates in the non-ohmic and electric-field activated regime [128].

5.2. RESULTS

5.2.1. PHASE TRANSITION AND FABRICATION

Thin MoS$_2$ flakes were obtained using the scotch tape technique and transferred on 285 nm SiO$_2$/Si substrates via a PDMS dry transfer method.[144] A transferred flake before the chemical treatment is shown in Fig. 5.1a. The flakes were immersed in n-
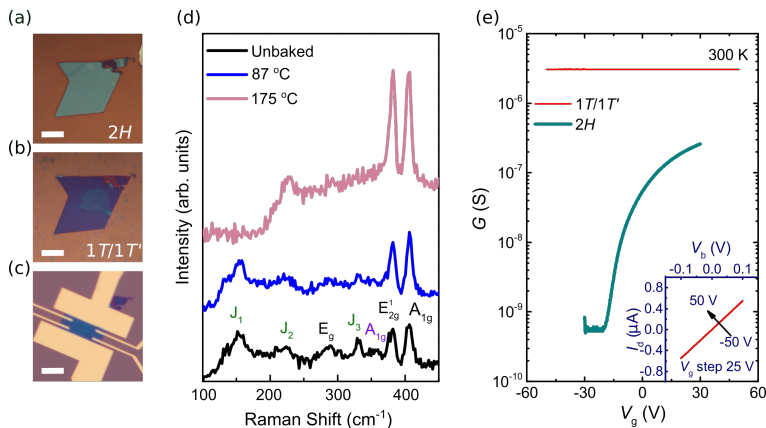
Figure 5.1: Room-temperature characterization of 1T/1T′-MoS$_2$ flakes and devices. Optical images of an MoS$_2$ flake after exfoliation (a), after immersion in n-butyllithium (b) and of a fabricated device (c). Scale bar is 15 μm. (d) Raman spectra from 1T/1T′-MoS$_2$ devices prepared under different conditions: Unbaked (black line), baked at 87 ^{o}C (blue line) and baked at 175 ^{o}C (red line). (e) Two-terminal conductance as a function of the back-gate voltage for 2H-MoS$_2$ (grey curve) and 1T/1T′-MoS$_2$ (red curve). The inset shows the transfer characteristics of the 1T/1T′ channel, for five back-gate voltages from -50 V to 50 V with a step of 25 V; all curves fall on top of each other.

butyllithium (1.6 M in hexane) for more than 48 hours and after extraction, the substrates were washed with hexane and deionized water to remove excess lithium. After the chemical treatment, there is a color change of the flake as can be seen in Fig. 5.1b. Another way to verify the phase transition is with Raman spectroscopy. Figure 5.1d depicts the spectrum of a flake after extraction from the n-butyllithium solution (black line). The J_1, J_2 and J_3 peaks that originate from the 1T′ phase (green labels), the A_{1g} peak from the 1T phase, as well as the E_g, E^1_{2g} and A_{1g} peaks from remnant patches of the initial 2H phase can be seen [134, 137]. The Raman spectrum therefore indicates that the phase transition was incomplete, in line with previous reports [142, 145].

After inducing the phase transformation, we proceed to device fabrication, for which standard e-beam lithography was used with a single layer PMMA resist. To preserve the 1T/1T′ phases, heating the PMMA above 95 ^{o}C must be avoided, which is the temperature at which the 1T/1T′ to 2H phase transition is expected to take place [133]. We have found that baking the PMMA resists at 87 ^{o}C in a vacuum oven for a couple of minutes is sufficient to preserve the 1T/1T′ phase. This can be seen in Fig. 5.1d, where the Raman spectrum before (black curve) and after baking (blue curve) is similar, indicating that there is no substantial composition change of the flake. In contrast, flakes with PMMA baked at 175 ^{o}C for 3 minutes show a significant reduction in the intensities of the J_1, J_2 and J_3 peaks with a change in the background and an increase in the peak intensity from the 2H phase.

After PMMA patterning via e-beam lithography, e-beam metal evaporation was used to evaporate 5 nm of Ti and 70 nm of Au to form the contacts. Several Hall bars and other

multi-terminal devices for transport measerements have been fabricated. The advantage of n-butyllithium treatment and post-fabrication, compared to a treatment after device fabrication, is that below the contacts there is 1T/1T′-MoS$_2$, which can provide better ohmic contacts according to earlier reports [39, 50]. One of the final devices is shown in Fig. 5.1c.

Figure 5.1e shows a room-temperature, two-probe electrical characterization of devices with 2H (grey) and 1T/1T′-MoS$_2$ (red) flakes. The G-V_g curves were obtained by applying a DC voltage bias between source and drain and measuring the source-drain current while sweeping the back-gate voltage. In the case of the sample with the 1T/1T′-MoS$_2$, the back-gate modulation of the conductance is negligible, while in the untreated 2H-MoS$_2$ sample the curve is semiconducting n-type with a high ON/OFF ratio. The zero transconductance in the case of the treated sample shows that the Fermi level lies inside the conduction band and that the material has a high electron density. The inset shows current-voltage characteristics from the device with the 1T/1T′-MoS$_2$ channel at different back-gate voltages; these are linear, indicating ohmic behavior.

5.2.2. TEMPERATURE DEPENDENCE IN THE OHMIC REGIME

To investigate the electrical properties of thin 1T/1T′-MoS$_2$ flakes, we studied their four- and two-terminal resistance as a function of temperature in two devices. Figure 5.2a shows current-voltage curves of two-terminal measurements that remain linear (ohmic) down to liquid nitrogen temperatures. The decreasing slope indicates that the resistance increases upon cooling. Using a four-probe configuration, we extract the resistance of the channel in the ohmic regime as a function of temperature by applying currents of ±100 nA between source and drain, while measuring the voltage drop across the channel. Figure 5.2b shows the two-probe and four-probe resistance as a function of temperature; both exhibit a strong temperature dependence displaying semiconductor-like behavior. The four-terminal resistance increases from 5 kΩ at room temperature to 180 kΩ at 90 K, while the two-probe resistance reaches 700 kΩ at 90 K. From this data, it is clear that although the 1T/1T′ state shows a reduced resistance at room temperature and no gate voltage dependence, at low temperatures it exhibits an insulating state.

From the data in Fig. 5.2b the contact resistance of the device can be estimated from the formula $R_c = 0.5(R_{2T} - (l_{2T}/l_{4T})R_{4T})$, where R_{2T} is the two-terminal and R_{4T} the four-terminal resistance, l_{4T} the length between the voltage probes and where l_{2T} is the length between the current contacts. At 275 K R_c is around 5.2 kΩ and increases considerably with decreasing temperature, reaching 70 kΩ at 90 K (Fig. 5.2c). The contact resistance in the two devices was found to be less than 20% of the total resistance between 90 K and 275 K.

To probe the nature of this localization, we analyze the temperature dependence of the four-terminal conductance of the device. The increase in the resistance indicates that the carrier transport takes place via hopping processes of the localized carriers. There are several models for hopping transport in solids. In the nearest neighbor hopping model (NNH) the resistivity is proportional to $\exp(E_A/k_B T)$, with E_A the activation energy [146]. The general form for VRH assisted transport on the other hand is $\rho \propto \exp((T_0/T)^a)$, where T_0 is a characteristic temperature. For two-dimensions and in the case of Mott-VRH, the exponent a is equal to 1/3 and the electrons hop between

states that are spatially further apart but closer energetically [147]. In the case of Efros-Shklovskii (ES) VRH the exponent $a = 1/2$ and hopping takes place under the influence of strong electron-electron interactions [148].

As it can be seen from the inset of Fig. 5.2b, which depicts the natural logarithm of the four-terminal conductance $\ln G$ as a function of $1000/T$, the data do not follow a straight line so that the NNH model cannot explain the conduction mechanism of 1T/1T'-MoS$_2$. To analyze this further, one can plot $\ln G$ *vs.* $T^{-1/2}$; in the case that the transport is governed by ES-VRH, the data should show a linear relation. The data in Fig. 5.2d shows such a plot, and the linear relation indeed suggests an ES-VRH mechanism. To confirm the exponent, one can also plot $\ln W$ as a function of $\ln T$, where $W = -\partial\ln\rho/\partial\ln T \propto a(T_o/T)^a$. The slope of $\ln W$ *vs.* $\ln T$ is equal to the exponent a. Such a plot is shown in the inset of Fig. 5.2d. From a linear fit, we extract an exponent $a = 0.46 \pm 0.02$, close to the exponent expected for an ES-VRH mechanism [149, 150]. Similarly from a second device (device B) $a = 0.43 \pm 0.02$. Interestingly, if we do the same analysis for two-terminal measurements that include the contact resistance, we find a slope for device A of 0.31±0.02 and for device B of 0.49±0.03, highlighting the importance of four-terminal measurements for the determination of such exponents.

Returning to the analysis of $\ln G$ *vs.* T^{-a}, we can also compare different linear fits taken for different exponents for the temperature on the x-axis. In the plot of $\ln G$ *vs.* $T^{-1/2}$, a linear fit yields a residual sum of squares error of 0.0076. Similarly, in a plot of $\ln G$ *vs.* $T^{-1/3}$ (not shown), the linear fit yields a value of the residual sum of squares error equal to 0.025. The smaller value of the residuals in the former case verifies that the Efros-Shkolvskii mechanism explains better our results than the Mott-VRH model. From this analysis, we can also extract the slope in a $\ln G$ *vs.* $T^{-1/2}$ plot, from which the characteristic temperature of the ES hopping (T_{ES}) can be determined. For the two devices, we find a T_{ES} of 5426 K (device A) and 7898 K (device B).

5.2.3. ELECTRIC-FIELD DEPENDENCE IN THE NON-OHMIC REGIME

Another aspect of hopping conduction is the field-assisted motion of charge carriers between localized states [151]. This field-assisted hopping leads to nonlinear transport characteristics and above a critical electric field the conductivity becomes temperature independent. According to the ES-VRH model, the dependence of the resistivity from the electric field (E) is given by [128, 152, 153]:

$$\rho \propto e^{(E_{ES}/E)^{1/2}}, \tag{5.1}$$

where E_{ES} is a characteristic field connected to the localization length(ξ) and to T_{ES} by the relationship: $E_{ES} = k_B T_{ES}/e\xi$ [152].

Bellow a critical field $E_c(T)$ transport follows an ohmic dependence and is in the strongly temperature-dependent regime, since the phonons assist the hopping processes. Above $E_c(T)$ the carriers have enough energy to pass the Coulomb barrier and the temperature dependence is suppressed. As $E_c(T)$ is temperature dependent and decreases as temperature is lowered, nonlinear current-voltage curves are therefore more prominent at low temperatures; furthermore, at low temperatures the channel resistance can become very high and four-terminal measurements are therefore more challenging for studying the electric-field dependence of transport.
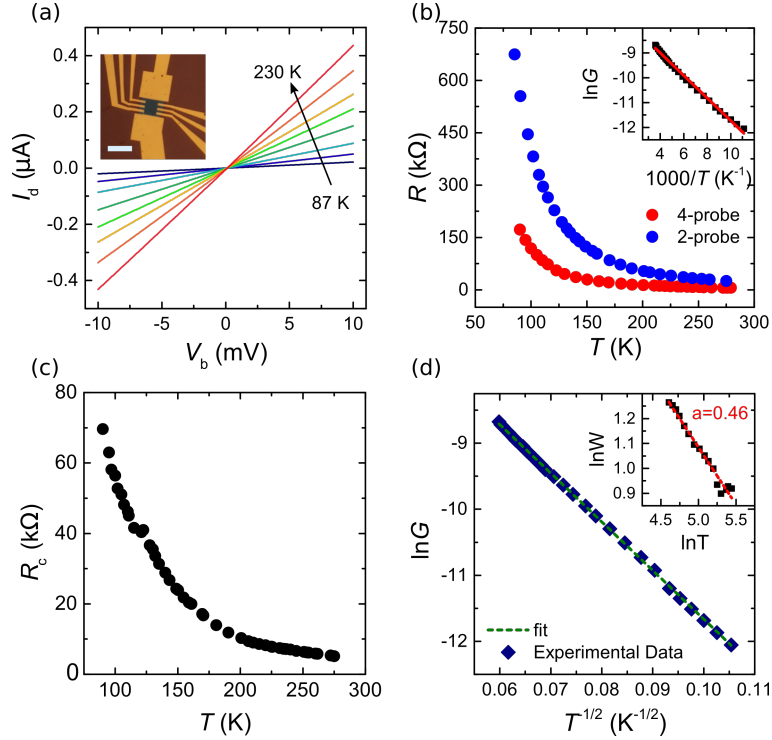
Figure 5.2: Four-terminal transport measurements from room-temperature to liquid nitrogen temperatures to determine transport mechanisms. (a) Current-voltage (I_d-V_b) characteristics from 87 K to 230 K. In this temperature range, the observed low-bias I_d-V_b curves are linear with resistances below 1 MΩ. Inset shows an optical image of the device that was used. Scale bar is 7 μm. (b) Two-terminal (blue) and four-terminal (red) resistance as a function of temperature. Inset shows the dependence of natural logarithm of the four-terminal conductance from the inverse of the temperature $1000/T$. The deviation of the data from a linear relation (red line) indicates that the transport mechanism is not nearest neighbor hopping. (c) Contact resistance as a function of temperature: at low temperatures, the contact resistance diverges. (d) $\ln G$ as a function of $T^{-1/2}$. The symbols are experimental data and the green dashed line the linear fit to them. Inset shows $\ln W$ (see main text for definition) as a function of $\ln T$. The linear fit yields an exponent $a = 0.46 \pm 0.02$, consistent with the ES-VRH model.
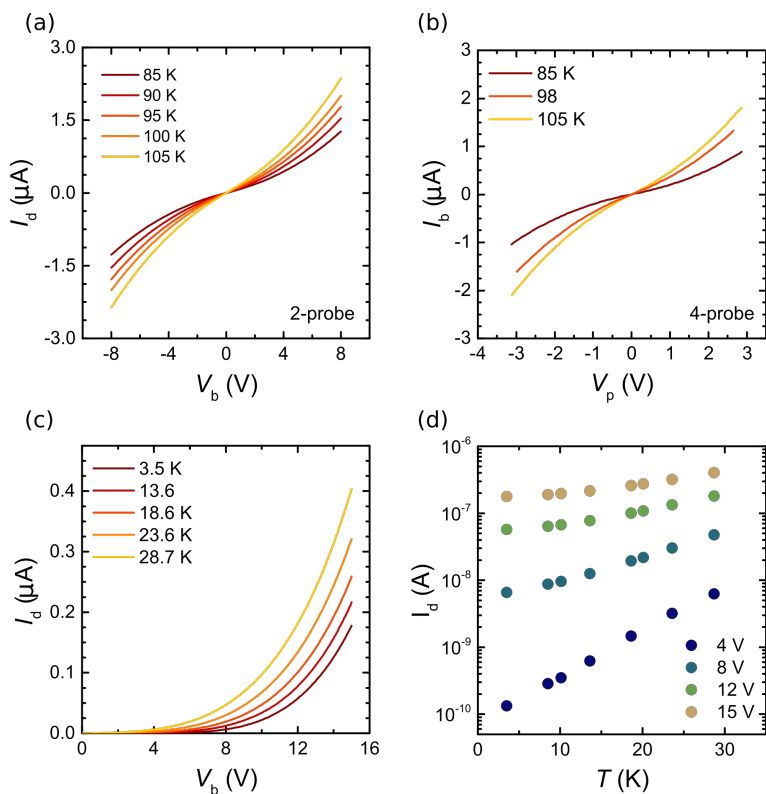
Figure 5.3: Non-linear transport in 1T/1T′-MoS$_2$. (a) Nonlinear current-voltage characteristics in the range of 85-105 K. (b) Four-terminal current-voltage characteristics at three different temperatures, displaying a nonlinear dependence. (c) (a) Current-voltage characteristics in the range of 3.5-30 K showing strong nonlinearities. (d) Semi-logarithmic plot of the current I_d as a function of temperature for different bias voltages V_b. The crossover from a strong temperature dependence to a weak temperature dependence of the channel current is more clearly seen.

In Fig. 5.3a and 5.3c we plot two-terminal I_d-V_b curves of the device (device B in this case), at temperatures between 85 and 105 K and 3.5 and 30 K, respectively; they are highly nonlinear. At a temperature of 3.5 K and with a bias of 4 V the resistance is 4.4 GΩ, while for 15 V it declines to 150 MΩ. Despite the high bias we did not observe electrical breakdown of the devices. Note, that the large channel and contact resistances (GΩ), do not allow to perform four-terminal measurements at very low temperatures due to the internal resistance of the voltmeter and the voltage limits of our isolation amplifiers. Nonlinear transport characteristics in the current-voltage curves in this device were also observed in four-terminal measurements at temperatures between 85 K and 105 K (see Fig. 5.3b), but the activationless regime is not accessible due to the high critical field (E_c) at these temperatures.

The crossover from strong to weak temperature dependence can be seen more clearly in Fig. 5.3d, which depicts a semi-logarithmic plot of the current as a function of temperature for different bias voltages (V_b). The plot indicates that the suppression of the temperature dependence takes place above 12 V. This translates to an electric field of 2×10^6 V/m for a channel of 6 μm. At V_b=4 V the ratio between the current at 3.5 K and 30 K is on the order of 50, while for 15 V this ratio is about 2.

Assuming that the nonlinearity in the current-voltage curves arises from ES-VHR with a negligible contribution from the contacts, we can then extract the ES electric field from the non-ohmic regime. The value of E_{ES} can be obtained by plotting the lnI_d as a function of $E^{-1/2}$ as depicted in Fig. 5.4 for different temperatures. As the electric field increases (left hand side of the plot) the curves from different temperatures converge to a single line at the temperature dependent critical field ($E_c(T)$). Equation (5.1) indicates that a least square fit to the linear part of the lnI_d-$E^{-1/2}$ curve provides an estimate for E_{ES}. For the lowest temperature (3.5 K), which fulfills this condition, we obtain a slope of 14347 (V/m)$^{1/2}$ that corresponds to an electric field of 2.06×10^8 V/m (inset of Fig. 5.4). For the other device, E_{ES} is found to be 3.8×10^8 V/m.

5.3. DISCUSSION

From the values of E_{ES} and T_{ES} determined from the experiment, the localization length ξ can be estimated using the relationship $\xi = k_B T_{ES}/eE_{ES}$. For device A the localization length is 1.2 nm, while for device B the localization length is 3.3 nm. The average hopping length, which for ES-VRH is given by $\bar{r} = \xi(T_{ES}/T)^{1/2}$, can be estimated using the experimental values of ξ and T_{ES}. At 300 K, the average hopping distances of the carriers in Device A and Device B are 5 and 17 nm, respectively. The obtained values of $\bar{r}$ favor the physical picture of electron hopping from one $1T$ phase patch to another as previously suggested by Kim et al. [143].

Another parameter that can be calculated from the data is the effective dielectric constant of Li treated MoS$_2$, which in this case originates from the $1T'$ and 2H phases between the $1T$ phase domains. According to the ES-VRH model the critical temperature is given by [154]:

$$T_{ES} = \frac{2.8e^2}{4\pi\epsilon_0\epsilon_r k_B\xi},$$

(5.2)

where e is the electron charge, ϵ_r is the dielectric constant and ϵ_0 the electric permittivity
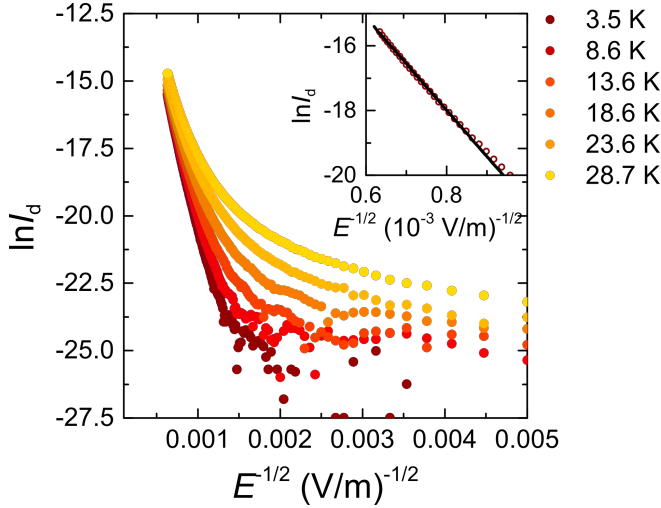
Figure 5.4: Determination of the characteristic field E_{ES} from the nonlinear transport data. $\ln I_d$ as a function of $E^{-1/2}$ for temperatures from 3.5 K to 28.7 K (red to yellow). The slope of the linear part at high electric fields and at 3.5 K yields the parameter $E_{ES}^{1/2}$ (inset).

of the vacuum. We estimate effective dielectric constants of 7 and 2 for the thick and thin flakes, in line with the order of magnitude expected for MoS_2 [155]. We note that this estimation of the dielectric constant does not take into account the possibly metallic character of the material, which could change the screening characteristics. To get better estimates of the effective dielectric constant in atomically thin materials, their 2D nature should be taken into account [156].

We also note that in a previous work Mott-VRH was observed in the transport behavior of n-butyllithium treated MoS_2 from two-terminal measurements, a hopping mechanism that is different compared to our analysis on data from four-terminal measurements [143]. We note, however, that an analysis of our two-terminal resistance data from device A can also be performed with the Mott-VRH model, with an exponent of $a = 0.31$ and a localization length of 0.7 nm, very similar to previous work [143], and in this sense the two datasets are not in contradiction.

Our observation of Efros-Shklovskii driven transport in $1T/1T'$-MoS_2 agrees with studies on similar systems [149, 157, 158]. Theoretical studies of irregular arrays of metallic grains, embedded in an insulating matrix resembling the n-butyllithium treated MoS_2 lattice, show that Coulomb interactions take place and that the transport follows the ES-VRH mechanism [157]. Similar results were obtained from electrical transport in two-dimensional graphene quantum dot arrays[158] and chemically reduced graphene oxide sheets [149].

Finally, the significant increase of the contact resistance in $1T/1T'$-MoS_2 suggests that the material is not the ideal candidate for contacting semiconducting 2H-MoS_2 for experiments at cryogenic temperatures. Nevertheless, at room temperature, the mea-

sured R_c is low, which is in agreement with previous studies [39]. Measurements on devices with varying channel lengths (transfer length method) and studies on flakes with higher content of the metallic $1T$ phase, can provide more insights regarding the behavior of the current injection into the 1T/1T′ material.

5.4. CONCLUSION

In summary, we observe Efros-Shklovskii-VRH transport in 1T/1T′-MoS$_2$, as obtained from a treatment with n-butyllithium. From temperature-dependent measurements in the ohmic regime and electric-field dependent studies in the non-ohmic and electric-field driven regime, we obtain localization lengths in the order 1-3 nm. An interesting future direction of research could be to quantify and control the mixing of the different phases and observe how this affects the transport mechanisms.

5

6

TUNNELING SPECTROSCOPY OF LOCALIZED STATES OF WS_2 BARRIERS IN VERTICAL VAN DER WAALS HETEROSTRUCTURES

In transition metal dichalcogenides, defects have been found to play an important role, affecting doping, spin-valley relaxation dynamics, and assisting in proximity effects of spin-orbit coupling. Here, we study localized states in WS_2 and how they affect tunneling through van der Waals heterostructures of h-BN/graphene/WS_2/metal. The obtained conductance maps as a function of bias and gate voltage reveal single-electron transistor behavior (Coulomb blockade) with a rich set of transport features including excited states and negative differential resistance regimes. Applying a perpendicular magnetic field, we observe a shift in the energies of the quantum levels and information about the orbital magnetic moment of the localized states is extracted.
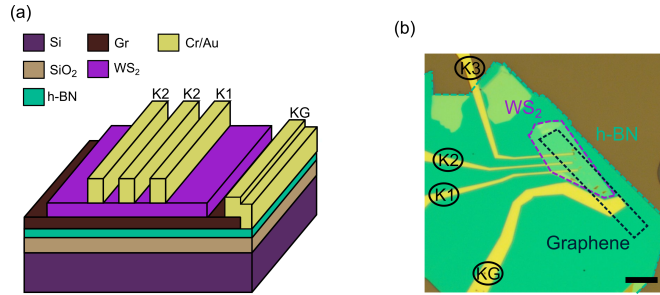
Figure 6.1: Device schematic and optical image. (a) 3D schematic illustration of a device illustrating the different layers and electrical contacts. (b) Optical image of a final device. The dotted purple and green lines indicate the shape of the WS$_2$ and h-BN flake, respectively. K1, K2 , K3 and KG are labels of the contacts. Scale bar: 5 μm.

6.1. INTRODUCTION

Tunneling spectroscopy in van der Waals and other heterostructures is a powerful tool that can reveal unique information about the density of states (DOS) of the electrodes [159, 160], about phonons (or other excitations) [161–163], about the chiral, valley [164] and spin states of the carriers [165, 166] and their interactions [167]. Recently it was shown that the presence of defects in crystalline hexagonal boron nitride (h-BN) tunneling barriers can be detected in the tunneling spectra, which is dominated by Coulomb blockade effects [168, 169].

Semiconducting layered materials such as transition metal dichalcogenides (TMDCs) are promising building blocks for transistors and tunneling devices [170–172]. Furthermore, because of their crystallinity and absence of surface dangling bonds, they can be used as ideal substrates and barriers[173–175] when the Fermi level is placed inside their band gap. Earlier studies have shown that WS$_2$, which has the largest bandgap among the TMDCs, is a promising material for tunneling transistors [173, 176]. Moreover heterostructures of graphene and WS$_2$ are interesting for proximity induced spin-orbit coupling in graphene [177] as well as for tuning the excitonic properties of TMDCs [178].

Here, we study tunneling spectroscopy of h-BN/graphene/WS$_2$/metal heterostructures at low temperatures. The conductance maps show clear Coulomb diamonds (CDs), which originate from tunneling through localized states formed by defects in the WS$_2$ barriers. Such states have also been found in electrostatically defined WS$_2$ quantum dots[179] but have not been studied in detail. We find that these localized states have a radius on the order of 2-12 nm in the plane of the WS$_2$, in agreement with previous reports [179]. Finally, by studying the behavior of the energies of different charge transitions under a perpendicular magnetic field, we calculate their orbital magnetic moments. Using these values, we estimate the spatial extent of the individual states.
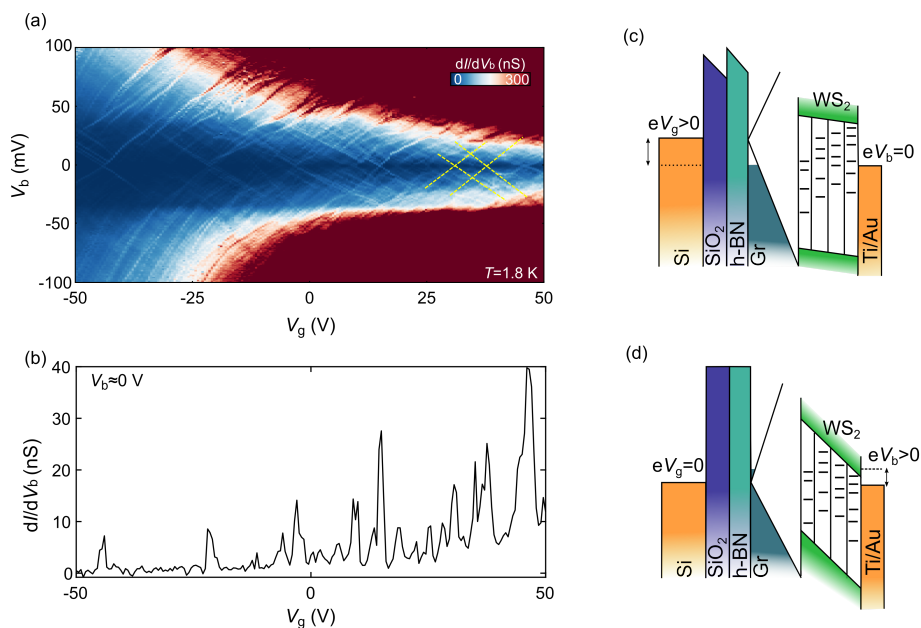
Figure 6.2: Tunneling spectroscopy at low temperatures. (a) Differential conductance (dI/dV_b) as a function of bias-voltage (V_b) and back-gate voltage (V_g) recorded at $T = 1.8$ K. The green dashed lines indicate two Coulomb-diamonds. (b) Line-cut showing at dI/dV_b versus V_g at $V_b = 0$ V extracted from (a). (c),(d) Energy band diagram of the vertical heterostructure under $V_g > 0$ V and $V_b = 0$ V in (c) and $V_g = 0$ V and $V_b > 0$ V in (d). The back-gate is capacitively coupled to the graphene as well as to the WS$_2$, which has discrete states in the band-gap that are located in different layers. Carrier tunneling between the two electrodes takes place via the impurity states. When the bias voltage $|V_b|$ increases above a certain point, carriers can directly tunnel into the conduction band of WS$_2$ thereby increasing the conductance significantly (regions in panel a).

6.2. RESULTS AND DISCUSSION

Devices with thin WS$_2$ tunnel barriers have been fabricated by a van der Waals pick-up method using poly-carbonate (PC) films [42]. A four-layer WS$_2$ flake and a monolayer flake were chosen as tunneling barriers. The bottom electrode in the devices consists of a monolayer graphene, while for the top tunneling electrodes Cr/Au or graphite was deposited on the WS$_2$ flakes. Moreover, we employ hexagonal boron nitride (h-BN) as bottom dielectric with a thickness of 40 nm. The flat h-BN substrates provide ideal substrates that eliminate extrinsic disorder in graphene and WS$_2$ [11]. Figure 1a and 1b show a schematic illustration of the 4L-WS$_2$ device and an optical image of the heterostructure, respectively. All the measurements shown in the main text are data taken from the device with four layers of WS$_2$ (D1), by using the KG-K1 tunneling electrodes (see Fig. 1). Data from the other electrodes can be found in the supplemental material section. The device with monolayer WS$_2$ (D2) as barrier did not show any tunneling characteristics, an observation that is in-line with reports on monolayer MoS$_2$ Josephson junctions, where metallic behavior in the monolayers was observed [180]. Results from the D2 device can be found in the supplemental material.

Figure 2a shows the dependence of the differential conductance (dI/d$V_{\rm b}$) on the tunnel bias ($V_{\rm b}$) and back-gate voltage ($V_{\rm g}$) at a temperature of 1.8 K. Although at room temperature the conductance of the device is a few μS (see Supplemental material), a significant decrease of three orders of magnitude in the values of dI/d$V_{\rm b}$, as well as many resonant features from Coulomb blockade effect are evident. The observed Coulomb diamonds in the differential conductance originate from parallel tunneling through multiple states originating from impurities in the WS$_2$ layers (Fig. 2c), presumably sulfur or tungsten vacancies. Similar features in hexagonal boron nitride tunneling barriers have been reported recently [168, 181?, 182]. Moreover, an increase in the number of the resonances with back-gate voltage is observed (Fig. 2b), that can be attributed to the presence of localized states close to the edge of the conduction band, which could originate from sulfur vacancies. Interestingly even at $V_{\rm g}$ = 50 V, the zero-bias background conductance is suppressed, verifying that the Fermi level of WS$_2$ is below the conduction band edge.

The conductance map in Fig. 2a provides further information about the nature of the localized states in the WS$_2$ sheet. The full-width-at-half-maximum (FWHM) of the zero-bias peaks is found to be close to $3.5k_{\rm B}T$ which suggests that the system is in the thermally broadened, weak coupling regime i.e. the electronic coupling to the impurity states is the smallest energy scale. Furthermore, from the slopes of the diamonds we can extract their capacitive couplings to the leads ($C_{\rm s}$, $C_{\rm d}$) and the back gate ($C_{\rm g}$) and can calculate the lever arm $\alpha = C_{\rm g}/(C_{\rm s} + C_{\rm d} + C_{\rm g})$ for the quantum dots [183]. We find that α follows a distribution of values in the range of $0.8 - 2.5$ meV/V, with a maximum at 1.3 ± 0.1 meV/V (see Fig. 6). Interestingly, we observe several diamonds with large values of α at large negative gate-voltages. A possible origin of these diamonds are different types of impurities with a smaller localization size and on-site capacitance. Assuming that the level spacing ΔE is much smaller than the charging energy $E_{\rm c}$, such that the addition energy $E_{\rm add} \approx 2E_{\rm c}$, and that the shape of the dots is circular, we can estimate the size of the quantum dots using $2E_{\rm c} = \frac{e^2}{8\epsilon_0\epsilon_{\rm r}r}$, for disk shape dots. Here e is the electron
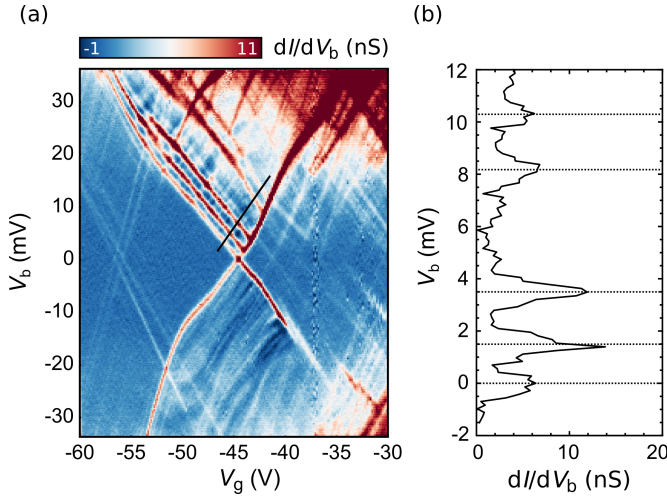
Figure 6.3: Excited state spectroscopy of defect states. (a) Detailed differential conductance map as a function of bias voltage V_b and gate voltage V_g. The Coulomb diamond shows four excited state lines that run in parallel to the diamond edge. (b) Energy as a function of differential conductance from the linecut in panel (a). The high conductance peaks correspond to the excited states and have energies of 1.4, 3.5, 8.2 and 10.3 meV.

6

charge, ϵ_0, the vacuum permittivity, r is the dot radius and $\epsilon_r = 3.9$ the effective relative permittivity of SiO_2 and h-BN. Using the extracted values of $E_{add} = 50 - 75$ meV, this assumption yields a quantum dot size of about 9-12 nm. It is worth to mention that the diamonds and their positions change significantly after thermally cycling the device (see Supplemental Material).

Above a voltage bias $|V_b|$ of 30 mV the conductance in the map of Fig. 2a increases significantly and many lines from diamonds can be observed. To explain such an increase of the current and the differential conductance at high bias, we have to take into account the effects of the interlayer voltage bias on the shape of the barriers. Although at zero bias and non zero gate voltage, the bias window contains only states within the band gap that assist the tunneling process (Fig. 2c), at higher bias the shape of tunneling barrier is modified and the WS_2 conduction band is lowered [184, 185]. This results in a field emission of the carriers above the band gap of WS_2 (Fig. 2d) [173, 185], where carriers from the graphene and the electrode can tunnel directly into the WS_2 layer, which increases the conductance significantly.

Figure 3a shows a detailed differential conductance map of the gate voltage regime between -60 and -20 V, where a clear Coulomb diamond can be observed. This particular diamond exhibits excited states for positive bias and many negative differential resistance (NDR) features in the sequential tunneling regime. Excited states can have many different origins and can be phonon, spin or orbital excited states. Figure 3b shows E vs. dI/dV_b obtained from the line-cut of Fig. 3a (black line). The level of the ground state has been shifted to 0 meV for clarity. From this we can extract the excited state energies

of the first two excited states which are 1.4 and 3.5 meV, respectively. The next pair of excited states have energies of 8.2 and 10.3 meV. It is worth mentioning that the diamonds, apart from providing information about the localized states in WS_2, show features that originate from the graphene. In a few diamonds (like the one shown in Figure 4a), we observe lines with slopes that are different from those of the diamond edges. These lines represent multiple negative-differential-resistance (NDR) like feature. Earlier reports on molecular junctions [186] and tunneling spectroscopy through h-BN barriers [187], have shown similar lines in their stability diagrams and they have been attributed to universal conductance fluctuations (UCFs) from the graphene contacts.

Upon application of a magnetic field perpendicular to the 2D plane, the Coulomb diamonds can reveal information about the spin and the orbital states. To this end we recorded the stability diagrams in the Fig. 3a and Fig. S1 at magnetic fields up to 12 T in order to study the field dependence of the ground and the excited states. Figure 4 shows the dI/dV_b maps at 0 and 12 T, in (a) and (b), respectively. From the former, we observe clearly three zero-bias resonances, from which two have same values of α (~1.3 mV/V) while the other one has a slightly higher value of α around 2.1 mV/V, presumably originating from a different type of defect. As it can be seen in Fig. 4b, the different types of diamonds have shifted horizontally at $B = 12$ T, which can be explained by the coupling of the electron magnetic moment to the magnetic field. Moreover, the UCF lines decrease in number upon increasing B due to the formation of Landau levels in the DOS of the graphene. Additionally, we observe bending of the excited state lines as well as the edges of the Coulomb diamonds, a finding which could be explained by parallel transport via multiple dots.

Figure 4c shows dI/dV_b versus V_g at zero bias, for magnetic fields from 0 to 12 T in steps of 0.5 T (blue to red). For $B = 0$ T, the three ground-state resonance peaks are located at -7, -10 and -11 V, which we label P1, P2 and P3, respectively. P1 and P3 have similar gate couplings, while P2 has a larger α as was seen in Fig. 4a. The P2 and P3 peaks shift in a similar way to more negative energies with increasing magnetic field, indicating that the two states have the same orbital wave-function. The P1 peak, on the other hand, shifts weakly to more positive gate values. Such shifts of the three states, originate from the coupling of the magnetic moments of the localized states to the external magnetic field. This becomes apparent when plotting the peak positions of P1, P2 and P3 as a function of magnetic field (Figure 4 (d)). The field dependence of the P2 and P3 peaks is non-linear, indicating a strong orbital magnetic moment of the involved ground state. Furthermore, from the linear fit to the high magnetic field data of peaks P1, P2 and P3, we get magnetic moments of 0.09±0.03, 0.44±0.05 and 0.32±0.03 meV/T, respectively. From the Zeeman energy, $E_z = \frac{1}{2}\mu B = \frac{1}{2}g\mu_B B$, where g is the Landé g-factor, μ and μ_B the magnetic moment and the Bohr magneton, g-factors 3.4±0.9, 15.8±1.8, 11.0±0.9. All the corresponding g-factors are much larger than the value of 2 expected for a free electron. Thus, orbital magnetic moments play a significant role in the magnetic field dependent transport of defects in WS_2.

Finally, we recorded the stability diagram shown in Fig. 3 at a magnetic field of 8 T (Fig. 4e). Besides the aforementioned bending of the excited state lines and the edges of the Coulomb diamond we observe a drastic change of the excited state energies when comparing the data recorded at 0 and 8 T: out of four lines observed at 0 T (see Fig. 3), we
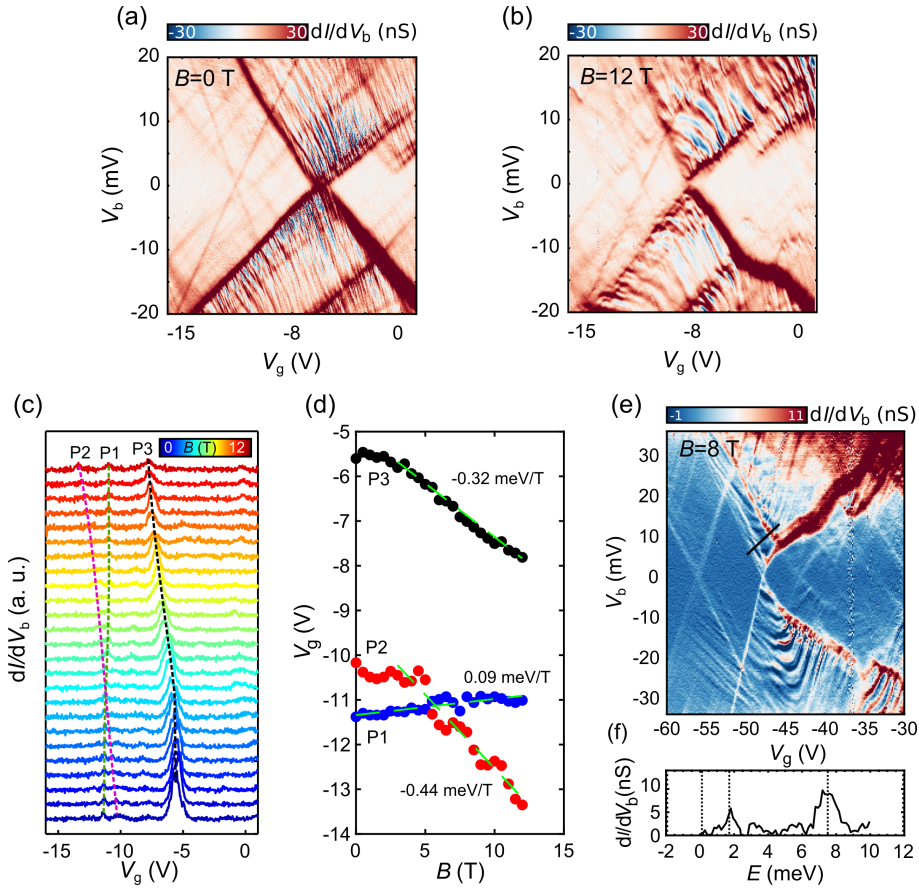
Figure 6.4: Ground state and excited state spectroscopy at finite magnetic fields. Differential conductance versus V_b and V_g obtained by applying B-fields of 0 in (a) and 12 T in (b). (c) Waterfall plot of dI/dV_b *vs.* V_g for different magnetic fields. The dashed lines track the shifts of the three different resonances. (d) Position of the P1, P2 and P3 peaks in (c) as a function of magnetic field. From linear fits to the data we extract $\mu_B = \frac{\Delta E}{\Delta B}$ equal to 0.09±0.03, 0.44±0.05 and 0.32±0.03 meV/T for P1, P2 and P3 respectively. (e) dI/dV_b map of Fig. 3 at B=8 T and dI/dV_b *vs.* E (f) from the linecut of panel (e).

only observe two lines with energies 1.8 and 7.3 mV at 8 T (Fig. 4f). Such strong changes of the excited state energies further suggests that the corresponding *g* factors are large and/or that the spin of the excited state is ≫ 1/2.

Unlike the hydrogen atom, whose ground-state has an orbital magnetic moment of zero ($m = 0$) due to spherical symmetry, in the case of a dot formed in a 2D material there is a finite out-of-plane orbital magnetic moment even for the *s*-shell, as a result of the reduced dimension along the *z*-axis. The orbital magnetic moment of a moving charge in a circular orbit, is given by [188, 189]: $\mu_{\text{orb}} = r e v_F / 2$, where r is the radius of the orbital, v_F the Fermi velocity and e the charge of the electron. Assuming a Fermi velocity around 1×10^5 m/s, we obtain a radius for the P1, P2 and P3 resonances of 2±1, 9±2 and 6±1 nm, in relatively good agreement with the estimations of the dot size based on the capacitance extracted from the addition energies (Fig. 2a).

6.3. Conclusions

In summary, we have performed tunneling spectroscopy measurements in van der Waals heterostructures with WS$_2$ barriers. Our data reveal a rich spectrum of Coulomb diamonds that we attribute to localized states inside the WS$_2$ sheet. These states localize carriers in a radius of a few to ten nanometers and show large orbital magnetic moments. Recent experiments indicate that such localized states have intrinsic spin-orbit coupling as large as 230 meV, and therefore tunneling devices as the ones shown here can be used for single spin-polarized electron injection. Lastly, localized states in TMDCs are important for single photon emission [190, 191] and if properly engineered could provide new systems for quantum communications, similar to nitrogen-vacancy centers in diamond.

6.4. Supplemental Material

6.4.1. Room temperature tunneling characteristics

At room temperature, the current-voltage (I-V_b) characteristics for different back-gate voltages (V_g), exhibit non-linear behavior (Fig. 6.5a). By increasing the back-gate voltage, the current and differential conductance increases (Fig. 6.5b), which is a characteristic of *n*-type behavior of the WS$_2$ film. The absence of graphene-transport characteristics like ambipolar behavior can be attributed to on-barrier thermionic emission of carriers from the graphene to the metallic contacts [173] or thermally activated interlayer hopping. The n-type behavior, also demonstrates that the electrochemical potential of WS$_2$ can be efficiently tuned by the back-gate.

6.4.2. Tunneling spectroscopy measurements from all contacts after thermal cycling

Figure 6.6, shows the conductance map from the same tunneling contacts as the ones that were used for the map of Fig. 2a of the main text (KG-K1). It can be seen that although the device is the same, the data set looks very different and it can be seen that the density of the Coulomb diamonds has increased. This indicates that the density of the defects has increased with time, even though the device was stored in low humidity
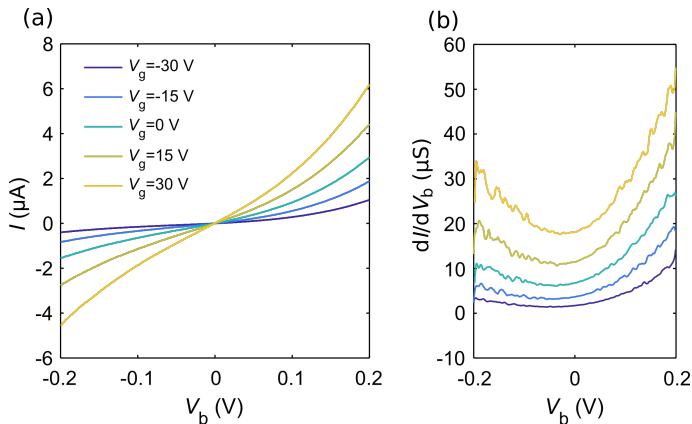
Figure 6.5: Room temperature tunneling characteristics of the device. Current (I) and differential conductance (dI/dV_b) versus voltage bias (V_b) for different gate voltages (V_g) in (a) and (b), respectively.

and N_2 rich conditions. Moreover, we find that although the first measurements contained diamonds with similar slopes, in Fig. 6.6 (also zoomed in Fig. 6.4a and 6.4b) we can observe some diamonds with different and actually steeper slopes. The back-gate lever arm a of such states reaches 2 mV/V. Although small variation in the values of a can be explained of a model of defects in different layers (Fig. 6.6d), such large value of a is attributed to a defect with smaller localization radius as indicated by the small magnetic moment in Fig. 6.4d.

Apart from the KG-K1 contacts that we used to investigate carrier tunneling in the device, also the KG-K2 and KG-K3 tunneling configurations were used and as it can be seen in Fig. 6.7, they show similar patterns.

6.4.3. SAMPLE (D2) WITH A MONOLAYER WS_2 AS TUNNEL BARRIER

Apart from the device with the 3-4 layer WS_2 barrier, we fabricated a device with a monolayer WS_2 barrier and with a top graphite contact, rather than Cr/Au. The reason for using graphite electrode, is to prevent the quality of the tunneling area of the monolayer WS_2. Figure 6.8a shows an optical image of the device consisting of Si/SiO$_2$/h-BN/graphene/1L-WS_2/graphite. This sample shows linear I-V_b characteristics with high currents at low temperatures (Fig. 6.8b), which is a signature of negligible barrier resistance and high transport transparency of the WS_2 layer. This is further verified from the dI/dV_b map at 8 T, where conductance enhancements due to Landau level formation is present (Fig. 6.8c). To elaborate further graphene at such magnetic fields is a quantum Hall insulator and the continuous density of states splits into Landau levels. As it can be seen these oscillations in Fig. 6.9c and 6.8d do not show an dependence on the V_b. Comparing these observations with similar reports on Josephson junctions with Mo_2 [180], we conclude that some short of charge transfer or hybridization between metal-leads and TMDC monolayer resulted in the metallic behavior of WS_2 monolayer [180].
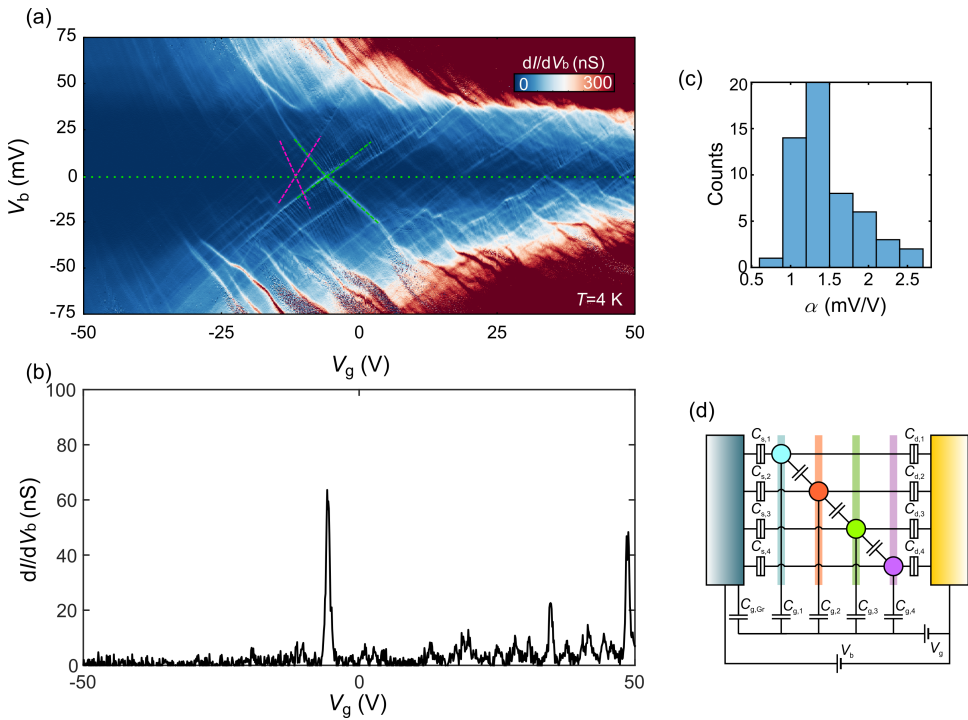
Figure 6.6: Differential conductance as a function of bias-voltage and back-gate voltage for $T = 2$ K. (b) Line-cut at $V_b = 0$ V from (a). The dash green and magenta lines indicate two different diamonds. (c) Histogram of the value of the a obtained from all the stability diagrams, showing a distribution attributed to the dispersion of the impurity states within the different layers. (d) Model of different dots in different layers that can explain the dispersion of values in a due to different coupling to the gate.
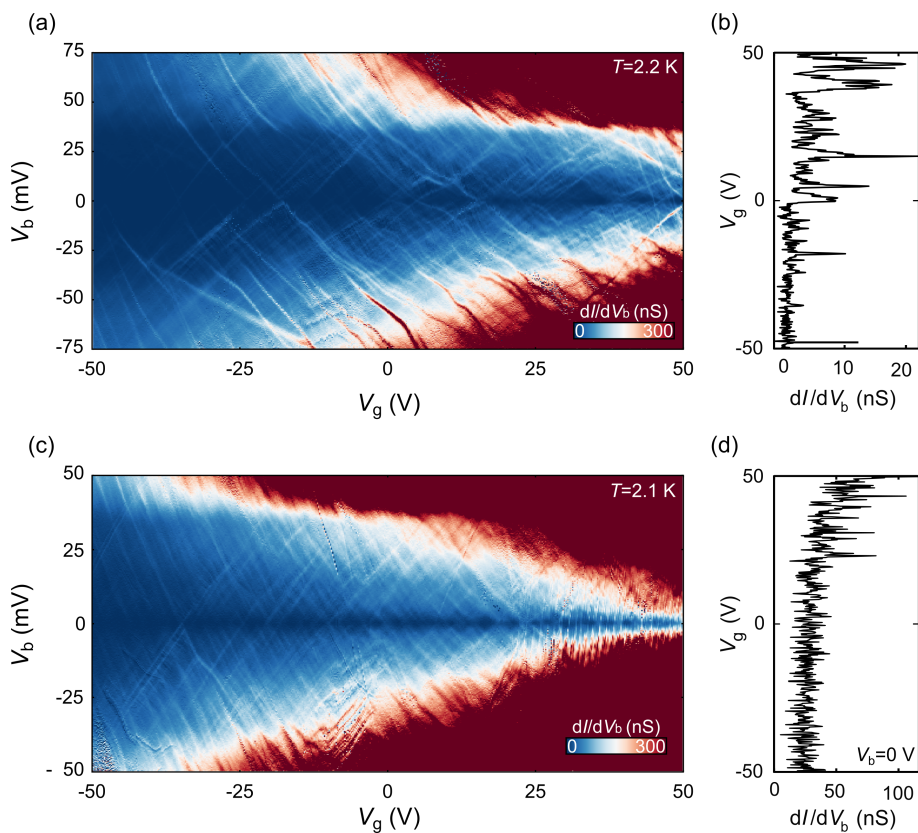
Figure 6.7: Tunneling spectroscopy using the other contacts. dI/dV_b from KG-K2 and KG-K3 contacts showing similar trends with Fig. 2c. Panels (b) and (d) depict zero bias dI/dV_b-V_g traces from panels (a) and (c), respectively. In panel (c) at the diamond at V_g=-30 V some excited states can be seen at negative V_b voltages.
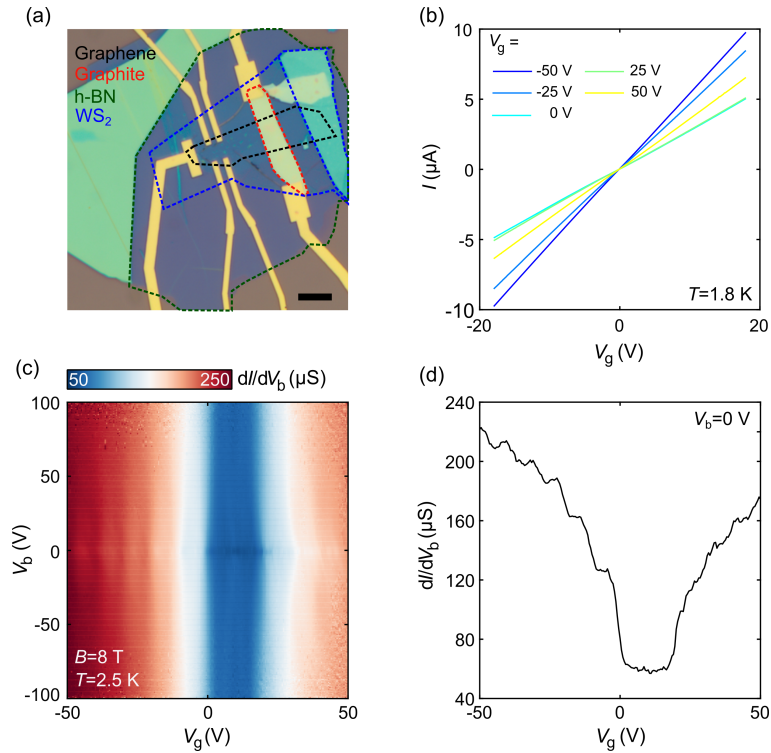
Figure 6.8: Data from a tunneling device with monolayer WS$_2$ barrier. (a) Optical image of a device consisting of Si/SiO$_2$/h-BN/graphene/1L-WS$_2$/graphite. Scale bar is at 6 μm (a) I-V_b characteristics for different back-gate voltages (T=1.7 K). The high linearity indicates high transparency of the monolayer WS$_2$ barrier. (c) dI/dV_b map at a perpendicular magnetic field of 8 T. The vertical dI/dV_b peaks originate from Landau levels in the graphene, but the independence from the V_b indicates ohmic transport rather than tunneling. (d) dI/dV_b-V_g for V_b=0 V. The conductance oscillations are due to the formation of Landau levels in the graphene electrode.

Regions were WS$_2$ has broke and graphene touches graphite directly, should not be excluded completely, although were not observed during the assembly process. Lastly, the zero-bias suppression of the conductance was also present in two-terminal measurements on the graphene layer and is due to non-ideal edge contacts to the graphene.

7

TUNNELING SPECTROSCOPY OF GRAPHENE ON WSE$_2$

2D materials are sensitive to their environment and modifications in their electronic spectrum can take place. It had been found that spin-orbit coupling from TMDCs can be proximitized to graphene. In this chapter we investigate such interactions of graphene on WSe$_2$ via tunneling spectroscopy in vertical heterostructures. We do not find any band gap and spin-splittings in the Landau level spectrum of graphene, which is in line with a Rashba type of induced spin-orbit coupling. Furthermore we find a Fermi velocity around 2×10^6 m/s, indicating spectrum renormalization. Lastly, we measure the gaps of the lowest Landau levels, which split as a result of lifted spin and valley degeneracy due to electron-electron interactions.

7.1. Introduction

Heterostructures of 2D materials have shown great results on interesting physics with a lot of potential for applications in electronics, photonics, photoelectronics and spintronics [9, 10, 192, 193]. One of the properties of 2D materials is that their properties can be altered when are placed in different environments. One of the most profound examples is graphene on hexagonal boron nitride (h-BN), where the mobility of the carriers resembles that of free-standing graphene and the charge inhomogeneity is reduced significantly, but also in graphene/h-BN superlattices the sublattice symmetry is broken and sizable bandgaps open [11, 194, 195]. Also, two examples that we are more interested here is the graphene in a modified dielectric environment that shows spectrum renormalization [196, 197] and modification of the band structure of graphene due to proximity induced spin-orbit coupling (SOC), which has recently attracted a lot of attention [27, 177, 198–201].

Here, we investigate the electronic properties of graphene on WSe$_2$ via tunneling spectroscopy through ultra-thin boron nitride barrier, that proves directly the electronic spectrum [202]. As tunneling electrode we use graphite that provides a flat and homogeneous electrode for the carriers of graphene. We examine possible modifications of the band structure of graphene due to proximity induced SOC, as well as modification due to the dielectric environment that can impact the Fermi velocity of the carriers.

7.2. Results and Discussion

7.2.1. Device configuration
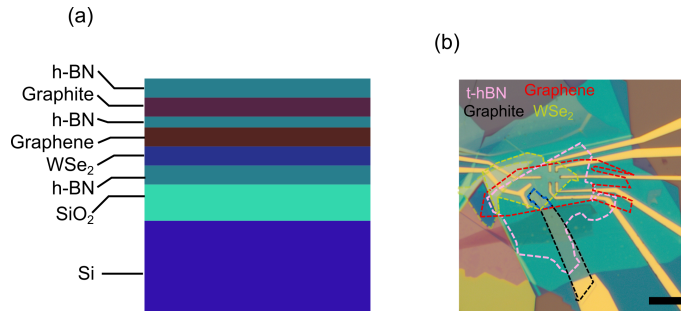
Figure 7.1: Si/SiO$_2$/h-BN/WSe$_2$/graphene/h-BN/graphite/h-BN heterostructure. (a) Schematic of the cross section of the heterostructure. (b) Optical image of the final device with highlighted some of the individual layers of the heterostructure. The scale bar corresponds to 8 μm.

Heterostructures of h-BN/WSe$_2$/graphene/h-BN/graphite/h-BN, were fabricated using the van der Waals pick-up technique with PC/PDMS stamps (Fig. 7.1a). Individual layers of few layer WSe$_2$, monolayer graphene, 3-4 layer of boron nitride as tunneling barrier, 20-40 nm of bottom and top boron nitride dielectrics and graphite flake (15-20 nm) were exfoliated on different substrates of SiO$_2$/Si and assembled via the van der

Waals pick-up technique. The heterostructure was processed such that edge contact of Cr/Au electrodes were deposited on the graphene and the graphite. The final device is shown in Fig. 7.1b. For the

7.2.2. TUNNELING AT ZERO MAGNETIC FIELD

The Fermi level of the graphene is tuned by the back-gate voltage and the interlayer bias voltage. All measurements were performed in a combination of DC+AC signals via a lock-in amplifier at the frequency of 187 Hz with excitation of 250-500 μm. Figure 7.2a shows the 2D plot of the differential conductance (dI/dV_b) as a function of the interlayer bias voltage (V_b) and the back-date voltage (V_g). Note that the back-gate voltage is applied to the Si electrode. There are many features visible in the particular plot. Firstly, the black dashed line indicates the low conductance loci that is associated with the zero DoS Dirac point of the graphene. The gate lever arm, is close to 9.3 mV/V. Second feature in the map is the low conductance band from -17 to 17 mV of V_b. This band is clearly independent from the back-gate voltage and is associated with the suppression of the elastic tunneling at those voltages [202, 204]. At higher voltages inelastic tunneling via phonon emission takes place and the conductance is increased. The suppression of the elastic tunneling rate comes from the fact that momentum of the carriers needs to be conserved and in the particular device the lattice of the graphene is strongly misaligned with the lattice graphite and that rotates the Brillouin zones of the materials resulting in large momentum offsets.

One more feature in the map that can be seen weakly is the vertical low conductance line at V_g=-7 V. This low conductance feature is independent from the interlayer bias and is the Corbino resistance of the graphene. Since the tunnel current has to traverse laterally through the graphene Layer to reach the contacts, the Corbino (spreading) resistance also contributes to our observed device resistance. On the other hand we cannot identify any characteristics related to graphite or WSe$_2$ DoS, but we can see some conductance resonances in the low dI/dV_b horizontal band (see also in Fig. 7.7), which originate from defect states in the h-BN barrier, responsible for effects like Coulomb blockade as we saw in the previous chapter.

The advantage of the tunneling device over other types of devices and experiments (transport, capacitance etc.) is the fact that the DoS of a material can be qualitatively seen in the data sets. Figure 7.2b shows a dI/dV_b-V_g curve from line cut at V_b=-50 mV. The 'V'-like shape of the graphene DoS can be seen clearly. We observe that the tunnel conductance of our device does not vanish at the Dirac point, where the DoS of pristine graphene is expected. This effect might originate from weak disorder in the sample that does not allow us to access that regime. Furthermore, if we plot the dI/dV_b as a function of the bias voltage for different back-gate voltages (Fig. 2c), we can identify the lower conductance dips that shift as the back-gate voltage changes (denoted with arrows on top of curves).

The tunneling process can be seen clearly in Fig. 7.3d in panels (i-iii). For V_b and V_b equal to zero and ignoring any doping effects the tunneling process can be seen in (i). Note that graphite is a compensated semimetal and electron-hole carriers coexist at zero energy. When an interlayer voltage is applied, the levels of graphene are shifted up (for negative bias and grounded graphite electrode) and there are carriers (electrons) from

7
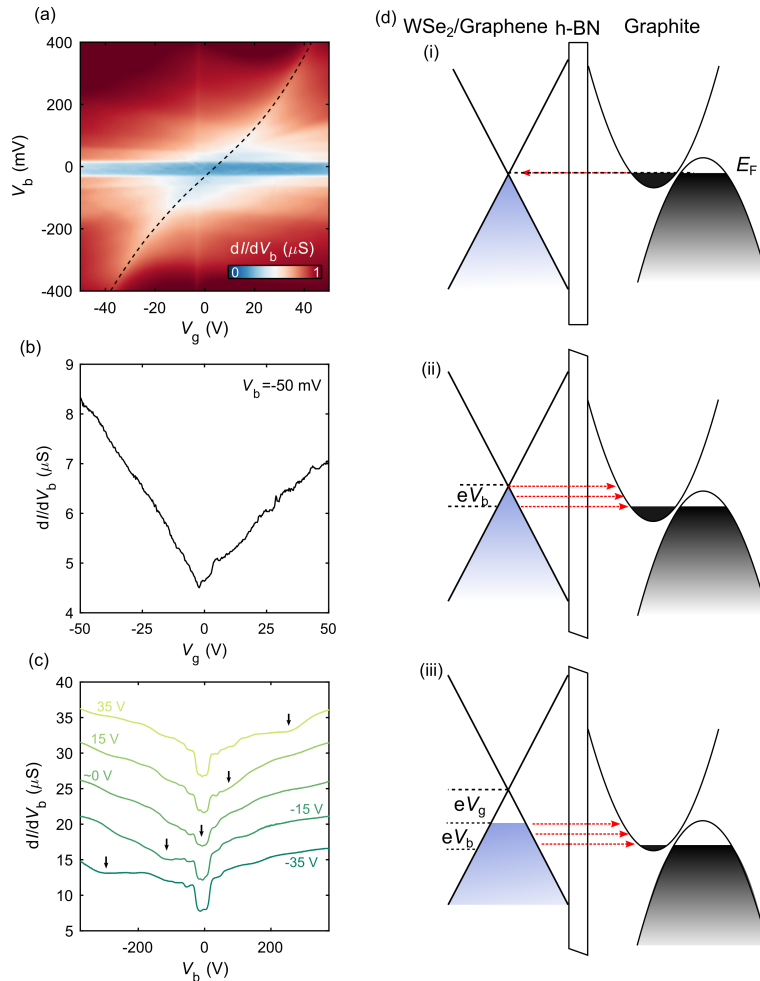
Figure 7.2: Carrier tunneling between graphene and graphite. (a) dI/dV_b vs. V_g and V_b at $T = 2$ K and B=0 T. The black dashed line indicates the low conductance associated with the DoS at the Dirac point of graphene. (b) dI/dV_b as a function of V_g at V_b=-50 mV. The line shape has the characteristic "V" shape of the graphene DoS. (c) dI/dV_b vs. V_b for different gate voltages. The arrows indicate the position of the Dirac point. (d) Tunneling process for different conditions. (i) for V_b=V_g=0 V, (ii) $V_b \neq 0$ V and for V_b and $V_{gb} \neq 0$ V. In the band structure of graphene has not been taken into account any modifications from the proximity induced SOC. The graphite DoS shown here has been sketched by taking into account that thin graphite is a compensated semimetal where electrons and holes are free for at zero energy [1, 203].

more states that can tunnel to the graphite's empty states. Upon application of a back-gate voltage the bands shift up or down in energy, thereby tuning the chemical potential of the graphene, and for a positive value the levels of the graphene shift further down,

consequently increasing carrier density and more electrons tunnel to the graphite.

7.2.3. LANDAU LEVEL SPECTROSCOPY
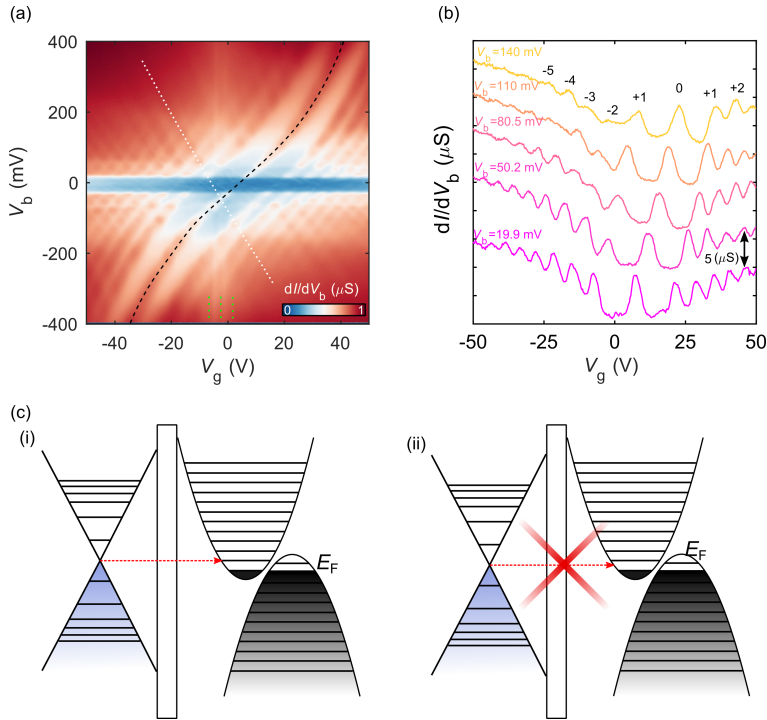
Figure 7.3: Tunneling at finite magnetic fields. (a) dI/dV_b *vs.* V_g and V_b at B=3 T. (b) dI/dV_b as a function of V_g at different V_b voltages. The curves are shifted vertically for clearance and the numbers on the peaks indicate the LL index. (c) Inter-Landau level tunneling. (i) Tunneling is allowed when the filled LLs from graphene align with empty LLs from the graphite. (ii) Tunneling is blocked when the filled Landau levels of graphene align with filled LLs from graphite

By applying a perpendicular to the device plane and large magnetic field, the Landau level spectrum of the graphene can be investigated. The presence of a gap or any spin-splittings in the DoS of the graphene should be seen in the dI/dV_b map as extra splittings in the LLs of the graphene. Figure 3c shows the conductance map at B=3 T. The black dashed line indicates the position of the zero-LL, while the white line indicates the resonances that probably emerge from LLs in graphite. The resonance from the LLs of the graphene and graphite are responsible for the observed checkerboard like structure. Similar maps have been observed in graphene to graphene tunneling in twisted heterostructures [205]. Although in graphene, due the dependence of the energy of the Landau levels on the magnetic field that follow the relationship $E_n \propto \sqrt{B}$, the individual LLs can be clearly seen and identified. On the other hand, the LLs that originate from the graphite, due to the parabolic dispersion of the bands, have equal distances and the

zero LL cannot be identified. As we mentioned above, graphite has large DoS and is a 3D metal, at which a quantum Hall effect is not expected, but recently has been shown that it undergoes a dimensional reduction and can hold a unique quantum Hall effect [203]. Figure 7.3a shows three vertical yellow dotted lines. These lines indicate the Corbino conductance that oscillates with the back-gate voltage due to finite conductance when the Fermi level crosses a LL. Since there are no edges in the graphene to assist transport, when the Fermi level lies between LLs the resistance takes very large values as the bulk of the graphene is gapped.

Figure 7.3 shows dI/dV_b vs. V_g for different values of interlayer bias voltage. the LLs of the graphene can be seen and they shift as the bias V_b changes. Up to thirteen individual LLs can be seen and eight of them have been labeled according to their index. Figure 7.3c explains schematically the tunneling process at finite magnetic field. The band structure of graphene and graphite forms LLs. When there are available empty LLs within the interlayer bias window the conductance is enhanced (panel i), while when all the LLs are occupied or the Fermi level of graphene and graphite lies between LLs, the conductance is suppressed (panel ii). From Fig. 7.3a and 7.3b broadening of the Landau levels at large bias is observed. The broadening with the increase of the bias voltage can be explained if we take into account that as the bias voltage increases, carriers acquire higher drift velocities until they reach the tunneling regime, which increases the effective temperature of the carriers.

From the LLs in Fig. 7.3a no splitting at the zero or any other LL is visible. This indicates that there is no gap at the graphene charge neutrality point or any spin-splittings as a result of the proximity induced SOC of the WSe$_2$, indicating that any Ising SOC is small or negligible.

Landau Fan diagrams can track the evolution of the LLs with the magnetic field. We have obtained the Landau fan diagrams at low and high bias, shown in Fig.7.4. For low bias (V_b=20 mV) the Landau fan diagram shows the emergence of LLs at magnetic fields as low as 0.1 T, characteristic of a high quality sample. The LLs show also their characteristic $B \propto E_n^2$ dependence as a result of the massless-Dirac linear spectrum of graphene.

As a result of the high quality of the sample the fourfold degeneracy of the zero Landau level is lifted, due to Coulomb exchange interactions that break the SU(4) (from the spin and valley) symmetry, at the magnetic field of 5 T. It is evident that all the other LLs do not show any splitting.

Spin splittings due to Rashba SOC in the band structure of a material are momentum-dependent (bands shifts horizontally) and cannot be probed by a tunneling experiment that probes quasi-particles in real-space [206]. It has also to be taken into account that the strength of the Rashba SOC has been measured to be 0-15 meV [200, 207–209], indirectly via weak antilocalization and spin-transport experiments, while Ising SOC that results in Zeeman-like spin splitting is in the order of 1-2 meV [210, 211]. On the other hand, SOC induced band gap has been predicted to be in the order of 0.54 meV [210]. Small vertical (in energy) splittings and bandgap cannot be easily resolved at 4 K and for voltage bias of 20 mV as a result of possible broadening. Also, lower bias is not possible due to the reduced carrier tunneling. In the Landau fan diagram obtained at bias of 150 mV, the -2,-1,+1 and +2 LLs cannot be resolved due to smearing, proving the need for low interlayer bias (Fig. 7.3b).
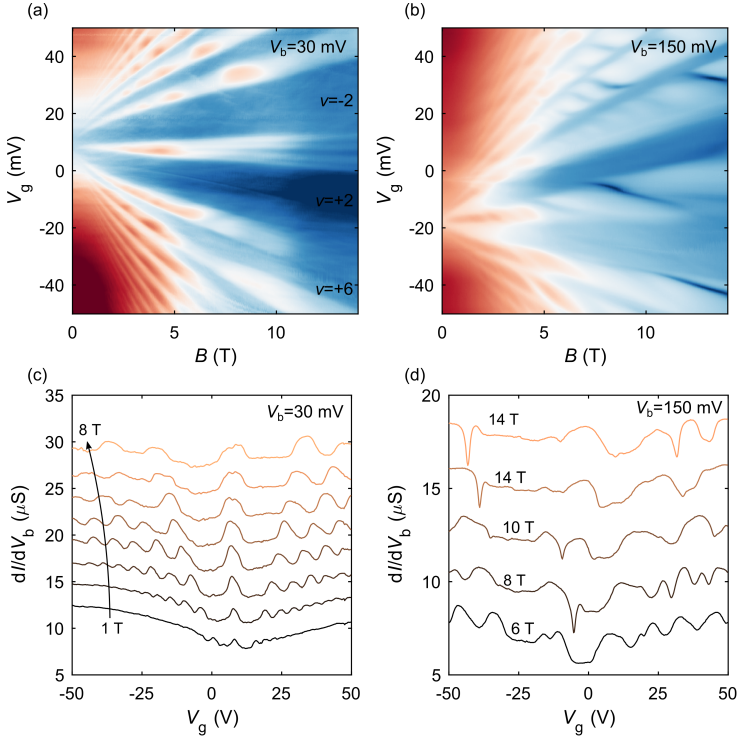
Figure 7.4: Landau Fan diagrams at different interlayer bias voltages. (a) Landau Fan diagram for V_b=30 mV in (a) and for V_b=150 mV in (b). In the low bias Fan diagram the zero LL breaks into four, while for bias of 150 mV such splitting cannot be observed. In the high bias regime the Fan diagram contains some conductance dips that cross different LLs. In panel (a) blue to red: 1 to 9 muS and in panel (b) 4 to 9 μS. (c) Plots of dI/dV_b as a function of V_g at different magnetic fields from panel (a) in (c) and from panel (b) in (d). In the low bias spectra the zero landau splits in four peaks, due to lift of the spin and valley degeneracy, with filling factors v=-2,-1,+1,+2. In the case of the spectra obtained with V_b=150 mV the LLs are not as clear and many conductance dips are observed.

The Fermi velocity of the relativistic Dirac Fermions can be obtained from the dispersion of the LLs. Based on the relationship:

$$E_n = E_D \pm \sqrt{2e\hbar v_F^2 |N| B}, N = 0, \pm 1, \pm 2, ..., \qquad (7.1)$$

where E_D is the energy of the charge neutrality point point, e is the electron charge, $\hbar$ is the Planck constant divided by 2π, v_F the Fermi velocity, N the Landau level index and B the magnetic field. From the E $vs.$ sign$\sqrt{NB}$ plot and based on a linear fit a Fermi velocity of 1.9-2.5 × 10^6 m/s is obtained (Fig. 7.5a). The value of the Fermi velocity that is obtained here is larger than the Fermi velocity of graphene on boron nitride [197, 212, 213] and can be attributed to the screening of the long range charged impurity scattering

by the WSe$_2$ substrate and the graphite electrode. Screening of the long range impurities can enhance the kinetic energy, leading to electronic spectrum renormalization [197].

Based on the plot of Fig.7,4a, we have evaluated the energy gaps for the filling factors of ν=0, ν=6 and ν=10 (Fig. 7.5b). The difference between the ν=0 and the ν =6,10 gaps is that the former is due to many-body interactions, while the other two result from the cyclotron orbits of the carriers. The ν=0 gap shows a more linear behavior and other than Coulomb interactions have to be also taken into account. These results are in agreement with previous findings [214].

Also, to investigate further the low conductance curves that appear in Fig. 7.4b we plot in Fig. 7.6 the dI/dV_b for B=14 T. In this plot the N=0 and ±1 LLs can be seen and they are very broadened. Also, many low conductance lines that seem symmetric around V_b=V_g=0 V are present. We can only speculate the origin of such complicated data structure, and we can say that it probably originates from the carrier tunneling conditions between graphene and graphite.
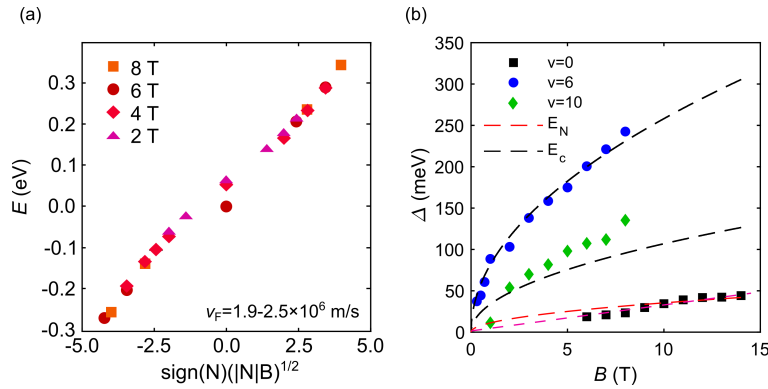
Figure 7.5: Fermi velocity and energy gaps of the LLs at different fillings (a) E as function of sign$\sqrt{NB}$ plot. The linear fit of the data yields Fermi velocity 1.9-2.5×10^6 m/s. (b) Dependence of the energy gaps of different filling factors on the magnetic field. The black dashed lines correspond to LL cyclotron gaps using Eq. (7.1) and the red dashed line based on the Coulomb energy ($E_c = e^2/4\pi l_b$, $l_B = 26$ nm /$\sqrt{B}$ and $\epsilon = 5\epsilon_0$). The magenta dashed line serves as a guide to the eye.

7.2.4. ZERO-BIAS PEAK AND DEFECT ASSISTED TUNNELING

In the section above we showed data from a large range o bias. For low bias a gap is observed. Figure. 7.7a illustrates the dI/dV_b map at the regime of ±14 mV. As it can be seen multiple Coulomb diamonds are present, but these resonances are weaker than the resonances in the case of the WS$_2$ in the previous chapter. The slope of the diamonds yields α equal to 1.3 mV/V, which is similar to what we found for the localized states of WS$_2$, and this value indicates dot size around ~10 nm. Another characteristic is the zero-bias peak of amplitude 0.4 μS that is present and spans in all the range of gate voltages. At a perpendicular magnetic field of B=7 T the map changes significantly and the peak looks like a dip.
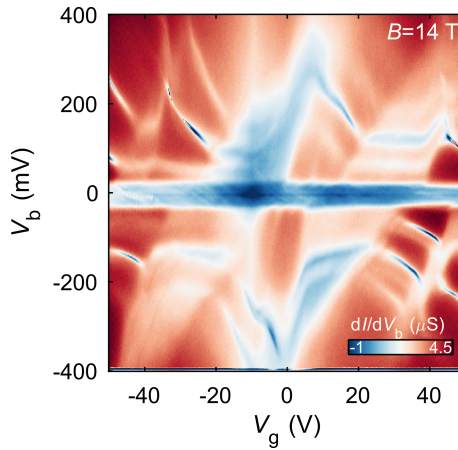
Figure 7.6: dI/dV_b *vs.* V_g and V_b at B=14 T. Only the -1, 0 and +1 LLs are visible with a very large broadening.

There are a few possible explanation for such-zero bias peak. Firstly, since there are multiple dots that cross each other, they can enhance the conductance at zero-bias voltage. Second possible explanation is the Kondo effect [215] that can create such pattern, and third and a bit more unlike is the coupling between electron (holes) from graphene and holes (electrons) from the graphite that result in pairing and a condensate giving rise to enhancement of conductance at zero-bias [216]. Although the first scenario is more likely, more experiments need to take place; for example temperature dependence or in-plane magnetic field measurements could elucidate the root of such observation.

7.2.5. CONCLUSION

In summary, we have studied tunneling spectroscopy in graphene on WSe$_2$ substrates. The tunneling spectra show the absence of a bandgap and splittings related to the proximity induced SOC, indicating that either such gap and splittings are too small to be resolved or the proximity induced Rashba SOC results in momentum-dependent spin-splitting and no considerable bandgap. From the datasets we have obtained the Fermi velocity that indicates reduction of the Coulomb interactions. Also, interactions play a significant role for energies close to the charge neutrality point, where the N=0 Landau level exhibits a fourfold splitting to the ν=±1 and ±2 filling factors. Further studies are required on the particular system in order to fully understand all the different features in the data as well as to verify the role on the WSe$_2$ in the properties of the graphene band structure. It would be beneficial if the graphite electrode can be substituted with a more simple metal that can provide an interface of similar quality, and does not form Landau levels at high magnetic fields.

7
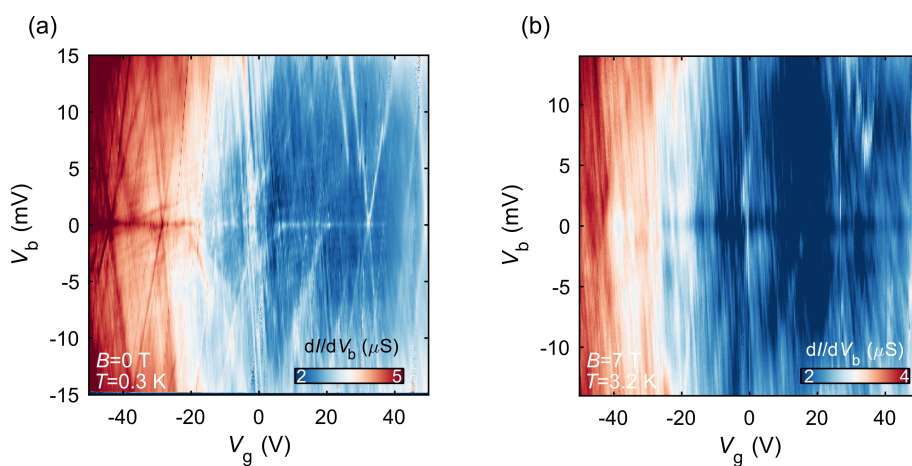
Figure 7.7: $\mathrm{d}I/\mathrm{d}V_{\mathrm{b}}$ map at B=0 T (a) and B=7 T (b). The suppressed tunneling regime shows multiple Coulomb diamonds that originate from defect assisted sequential tunneling. For B=0 T and at V_{b}=0 mV an enhancement of the conductance is observed, while for B=7 T the zero-bias peak becomes a dip.

8

CONCLUSIONS AND OUTLOOK

In conclusion we saw a few works of electrical transport in 2D heterostructures. The results can be summarized below:

In chapter 3 it was shown that encapsulation with boron nitride does not improve only the electron mobilities but also improves other properties of the electrons. We overcame the problem of forming ohmic contacts by a technique with pre-etched windows for metal evaporation top boron nitride layer. By studying the weak localization effect we saw that the phase coherence is improved with respect to MoS_2 on SiO_2 substrate, but the spin relaxation is relatively fast and in the order of a few picoseconds. Since the spin relaxation in good quality samples takes place through intravalley scattering, the fast spin relaxation that we obtained, indicates that the intravalley scattering is fast. The independence of the spin relaxation time on the electron density is a characteristic that indicates that spin-flip due to electron-electron scattering that decreases with the increase of the gate voltage compete with the Rashba SOC that tends to increase the spin-flip rate.

In chapter 4 we studied another 2D semiconductor, TiS_3, which shows a rich range of properties. In order to avoid extrinsic disorder we encapsulated the devices with h-BN as in the case of MoS_2. We found that when the Fermi level lies in the conduction band the material show metallic behavior with metal insulator transitions at low temperatures. The highest mobility reached by our devices is 350 cm^2/Vs at 90 K, and is the highest to be reported so far. Until 60 K, TiS_3 shows trivial electrical properties of a band-insulator or semiconductor, but below 60 K the non linear transport characteristics exhibit signatures of a charge-density-wave phase along with features of localization. The critical temperature and electric-field of the CDW depinning is found dependent on the electron density that can be controlled through the gate electrode yielding new opportunities for studying many-body phenomena in TiS_3.

$1T/1T'$-MoS_2 whose electrical transport mechanism was not known, was studied in chapter 5. Although the devices show low resistivity and no modulation of the conductivity through the backgate (due the large carrier density) at room temperature, as the temperature decreases the resistance increases rendering the material an Anderson in-

sulator, which is insulator due to high disorder or inhomogeneity. Temperature dependence of the resistivity can elucidate the transport mechanism, which we found to be the Efros-Shklovskii variable-range-hopping, in contrast to earlier reports with two-terminal measurement that show Mott variable-range-hopping as the transport mechanism. The localization length is found around 10 nm in line with the size of the 1T domains. The role of the electron-electron interactions and the reduced screening in 2D materials, implicates that Efros-Shklovskii could be potentially the dominant variable-range-hopping mechanism in the 2D limit.

In the second part of the thesis we explored physics in the tunneling devices with combinations of TMDCs with graphene. The motivation of such experiments was to learn whether one can extract direct evidence of proximity effects in the band structure of graphene and what are the limitations. In chapter 6 when we use WS_2 as a tunneling barrier in vertical heterostructures, the conductance maps can be dominated by Coulomb diamonds whose origin is defect/impurity states withing the WS_2 layers. Although such observation obstructs in studying the density of states of the graphene, it provides a lot of valuable information about such states, that are important for the electronic and optical properties of WS_2 and similar TMDCs. From the conductance maps and more accurately from the Coulomb diamond slopes we can distinguish different types of defect states. By studying the behavior of such states at large magnetic fields we also showed that they have finite magnetic moments, which we used to calculate the localization lengths of individual states, and found to be 2-10 nm.

Finally in chapter 7 we explore tunneling of heterostructures where graphene lies on a WSe_2 and carriers tunnel though ultrathin boron nitride to the graphite electrode. Ultathin boron nitride is insulator and can have less disorder than TMDCs, therefore is a better candidate for tunneling experiments. Graphene on WSe_2 shows good quality with Landau level formation at magnetic fields of 0.1 T. The DoS of the graphene was probed at high magnetic fields and the characteristic with the Dirac type of Landau level dispersion was revealed. We observed symmetry breaking states at the zero Landau level due to electron-electron interactions, but not any visible splitting due to the proximity induced spin-orbit coupling. This proves that Rashba SOC that splits the spin up and spin down bands in momentum can be stronger than Ising SOC, which shifts spin-up and spin-down bands in energy. Lastly we measured the Fermi velocity of the carriers, which depends on the dielectric environment and was found equal to 1.9-2.5×10^6 m/s.

Further directions of research would be to experiment further with tunneling experiment with graphene on WSe_2 or encapsulated to WSe_2 where WSe_2 acts also as a tunnel barrier. Such experiments will provide more evidence about the proximity induced spin-orbit coupling in graphene and its consequence to the band structure of graphene. Helical edge states that were found to exist in bilayer graphene proximitized to WSe_2 can be important in graphene Josephson junctions and SOC induced topological phases in multilayer graphene have been proposed [211]. Transport with TMDCs has matured over the years and some groups around the world are advancing with samples and devices of higher quality where the spin-valley properties can be probed in magnetotransport in the quantum Hall regime [57, 217]. Weak localization and antilocalization can be explored further in the low density regime in bilayer MoS_2 or $MoSe_2$ and it can be studied in detail how the position of the Fermi level at the spin-valley split bands, as well as

the inversion symmetry affects quantum interference effects. Lastly a more interesting direction would be the realization of Majorana bound states in graphene. Combining proximity induced SOC and superconductivity in graphene one can explore Majorana physics [30]. Limiting the transport modes to 1 by using the ν=1 LL or using bilayer graphene quantum point contacts. In combination with tunneling experiments there can be direct evidence for the existence of such exotic states in graphene.

8

References

[1] K. S. Novoselov, *Electric field effect in atomically thin carbon films,* Science **306**, 666 (2004).

[2] M. Dresselhaus and G. Dresselhaus, *Intercalation compounds of graphite,* Advances in Physics **30**, 139 (1981).

[3] A. K. Geim and P. Kim, *Carbon wonderland,* Scientific American **298**, 90 (2008).

[4] E. P. Randviir, D. A. Brownson, and C. E. Banks, *A decade of graphene research: production, applications and outlook,* Materials Today **17**, 426 (2014).

[5] N. C. Wang, S. Sinha, B. Cline, C. D. English, G. Yeric, and E. Pop, *Replacing copper interconnects with graphene at a 7-nm node,* in *2017 IEEE International Interconnect Technology Conference (IITC)* (IEEE, 2017).

[6] K. S. Novoselov, D. Jiang, F. Schedin, T. J. Booth, V. V. Khotkevich, S. V. Morozov, and A. K. Geim, *Two-dimensional atomic crystals,* Proceedings of the National Academy of Sciences **102**, 10451 (2005).

[7] B. Radisavljevic, A. Radenovic, J. Brivio, V. Giacometti, and A. Kis, *Single-layer MoS2 transistors,* Nature Nanotechnology **6**, 147 (2011).

[8] T. kumar Agarwal, B. Soree, I. Radu, P. Raghavan, G. Iannaccone, G. Fiori, W. Dehaene, and M. Heyns, *Material-device-circuit co-optimization of 2d material based FETs for ultra-scaled technology nodes,* Scientific Reports **7** (2017), 10.1038/s41598-017-04055-3.

[9] A. K. Geim and I. V. Grigorieva, *Van der waals heterostructures,* Nature **499**, 419 (2013).

[10] K. S. Novoselov, A. Mishchenko, A. Carvalho, and A. H. C. Neto, *2d materials and van der waals heterostructures,* Science **353**, aac9439 (2016).

[11] C. R. Dean, A. F. Young, I. Meric, C. Lee, L. Wang, S. Sorgenfrei, K. Watanabe, T. Taniguchi, P. Kim, K. L. Shepard, and J. Hone, *Boron nitride substrates for high-quality graphene electronics,* Nature Nanotechnology **5**, 722 (2010).

[12] J. Xue, J. Sanchez-Yamagishi, D. Bulmash, P. Jacquod, A. Deshpande, K. Watanabe, T. Taniguchi, P. Jarillo-Herrero, and B. J. LeRoy, *Scanning tunnelling microscopy and spectroscopy of ultra-flat graphene on hexagonal boron nitride,* Nature Materials **10**, 282 (2011).

[13] B. Hunt, J. D. Sanchez-Yamagishi, A. F. Young, M. Yankowitz, B. J. LeRoy, K. Watanabe, T. Taniguchi, P. Moon, M. Koshino, P. Jarillo-Herrero, and R. C. Ashoori, *Massive dirac fermions and hofstadter butterfly in a van der waals heterostructure,* Science **340**, 1427 (2013).

[14] L. A. Ponomarenko, R. V. Gorbachev, G. L. Yu, D. C. Elias, R. Jalil, A. A. Patel, A. Mishchenko, A. S. Mayorov, C. R. Woods, J. R. Wallbank, M. Mucha-Kruczynski, B. A. Piot, M. Potemski, I. V. Grigorieva, K. S. Novoselov, F. Guinea, V. I. Fal'ko, and A. K. Geim, *Cloning of dirac fermions in graphene superlattices,* Nature **497**, 594 (2013).

[15] L. Wang, Y. Gao, B. Wen, Z. Han, T. Taniguchi, K. Watanabe, M. Koshino, J. Hone, and C. R. Dean, *Evidence for a fractional fractal quantum hall effect in graphene superlattices,* Science **350**, 1231 (2015).

[16] L. Wang, I. Meric, P. Y. Huang, Q. Gao, Y. Gao, H. Tran, T. Taniguchi, K. Watanabe, L. M. Campos, D. A. Muller, J. Guo, P. Kim, J. Hone, K. L. Shepard, and C. R. Dean, *One-Dimensional Electrical Contact to a Two-Dimensional Material,* Science **342**, 614 (2013).

[17] L. Wang, I. Meric, P. Y. Huang, Q. Gao, Y. Gao, H. Tran, T. Taniguchi, K. Watanabe, L. M. Campos, D. A. Muller, J. Guo, P. Kim, J. Hone, K. L. Shepard, and C. R. Dean, *One-dimensional electrical contact to a two-dimensional material,* Science **342**, 614 (2013).

[18] X. Cui, G.-H. Lee, Y. D. Kim, G. Arefe, P. Y. Huang, C.-H. Lee, D. A. Chenet, X. Zhang, L. Wang, F. Ye, F. Pizzocchero, B. S. Jessen, K. Watanabe, T. Taniguchi, D. A. Muller, T. Low, P. Kim, and J. Hone, *Multi-terminal transport measurements of MoS2 using a van der Waals heterostructure device platform,* Nature Nanotechnology **10**, 534 (2015).

[19] J. I.-J. Wang, Y. Yang, Y.-A. Chen, K. Watanabe, T. Taniguchi, H. O. H. Churchill, and P. Jarillo-Herrero, *Electronic Transport of Encapsulated Graphene and WSe2 Devices Fabricated by Pick-up of Prepatterned hBN,* Nano Lett. **15**, 1898 (2015).

[20] A. Avsar, I. J. Vera-Marun, J. Y. Tan, K. Watanabe, T. Taniguchi, A. H. C. Neto, and B. Özyilmaz, *Air-stable transport in graphene-contacted, fully encapsulated ultrathin black phosphorus-based field-effect transistors,* ACS Nano **9**, 4138 (2015).

[21] A. Allain, J. Kang, K. Banerjee, and A. Kis, *Electrical contacts to two-dimensional semiconductors,* Nature Materials **14**, 1195 (2015).

[22] D. Rhodes, S. H. Chae, R. Ribeiro-Palau, and J. Hone, *Disorder in van der waals heterostructures of 2d materials,* Nature Materials **18**, 541 (2019).

[23] T. Mueller and E. Malic, *Exciton physics and device application of two-dimensional transition metal dichalcogenide semiconductors,* npj 2D Materials and Applications **2** (2018), 10.1038/s41699-018-0074-2.

[24] K. F. Mak, C. Lee, J. Hone, J. Shan, and T. F. Heinz, *Atomically Thin MoS2: A New Direct-Gap Semiconductor,* Phys. Rev. Lett. **105**, 136805 (2010).

[25] X. Xu, W. Yao, D. Xiao, and T. F. Heinz, *Spin and pseudospins in layered transition metal dichalcogenides,* Nature Physics **10**, 343 (2014).

[26] J. R. Schaibley, H. Yu, G. Clark, P. Rivera, J. S. Ross, K. L. Seyler, W. Yao, and X. Xu, *Valleytronics in 2d materials,* Nature Reviews Materials **1** (2016), 10.1038/na-

trevmats.2016.55.

[27] Z. Wang, D.-K. Ki, H. Chen, H. Berger, A. H. MacDonald, and A. F. Morpurgo, *Strong interface-induced spin–orbit interaction in graphene on WS$_2$,* Nature Communications **6**, 8339 (2015).

[28] H. Meissner, *Superconductivity of contacts with interposed barriers,* Physical Review **117**, 672 (1960).

[29] J. J. Hauser, *Magnetic proximity effect,* Physical Review **187**, 580 (1969).

[30] F. Finocchiaro, F. Guinea, and P. San-Jose, *Topological π junctions from crossed andreev reflection in the quantum hall regime,* Physical Review Letters **120** (2018), 10.1103/physrevlett.120.116801.

[31] A. Mishchenko, J. S. Tu, Y. Cao, R. V. Gorbachev, J. R. Wallbank, M. T. Greenaway, V. E. Morozov, S. V. Morozov, M. J. Zhu, S. L. Wong, F. Withers, C. R. Woods, Y.-J. Kim, K. Watanabe, T. Taniguchi, E. E. Vdovin, O. Makarovsky, T. M. Fromhold, V. I. Fal'ko, A. K. Geim, L. Eaves, and K. S. Novoselov, *Twist-controlled resonant tunnelling in graphene/boron nitride/graphene heterostructures,* Nature Nanotechnology **9**, 808 (2014).

[32] Y. Cao, V. Fatemi, A. Demir, S. Fang, S. L. Tomarken, J. Y. Luo, J. D. Sanchez-Yamagishi, K. Watanabe, T. Taniguchi, E. Kaxiras, R. C. Ashoori, and P. Jarillo-Herrero, *Correlated insulator behaviour at half-filling in magic-angle graphene superlattices,* Nature **556**, 80 (2018).

[33] Y. Cao, V. Fatemi, S. Fang, K. Watanabe, T. Taniguchi, E. Kaxiras, and P. Jarillo-Herrero, *Unconventional superconductivity in magic-angle graphene superlattices,* Nature **556**, 43 (2018).

[34] R. Bistritzer and A. H. MacDonald, *Moire bands in twisted double-layer graphene,* Proceedings of the National Academy of Sciences **108**, 12233 (2011).

[35] M. Yankowitz, S. Chen, H. Polshyn, Y. Zhang, K. Watanabe, T. Taniguchi, D. Graf, A. F. Young, and C. R. Dean, *Tuning superconductivity in twisted bilayer graphene,* Science **363**, 1059 (2019).

[36] X. Lu, P. Stepanov, W. Yang, M. Xie, M. A. Aamir, I. Das, C. Urgell, K. Watanabe, T. Taniguchi, G. Zhang, A. Bachtold, A. H. MacDonald, and D. K. Efetov, *Superconductors, orbital magnets, and correlated states in magic angle bilayer graphene,* (2019), arXiv:1903.06513 .

[37] F. Wu, T. Lovorn, E. Tutuc, I. Martin, and A. H. MacDonald, *Topological insulators in twisted transition metal dichalcogenide homobilayers,* Phys. Rev. Lett. 122, 086402 (2019) (2018), arXiv:1807.03311 .

[38] H. Ochoa, F. Finocchiaro, F. Guinea, and V. I. Fal'ko, *Spin-valley relaxation and quantum transport regimes in two-dimensional transition-metal dichalcogenides,* Physical Review B **90** (2014).

[39] R. Kappera, D. Voiry, S. E. Yalcin, B. Branch, G. Gupta, A. D. Mohite, and M. Chhowalla, *Phase-engineered low-resistance contacts for ultrathin MoS2 tran-*

8

sistors, Nature Materials **13**, 1128 (2014).

[40] R. V. Gorbachev, A. K. Geim, M. I. Katsnelson, K. S. Novoselov, T. Tudorovskiy, I. V. Grigorieva, A. H. MacDonald, S. V. Morozov, K. Watanabe, T. Taniguchi, and L. A. Ponomarenko, *Strong coulomb drag and broken symmetry in double-layer graphene,* Nature Physics **8**, 896 (2012).

[41] Y. Huang, E. Sutter, N. N. Shi, J. Zheng, T. Yang, D. Englund, H.-J. Gao, and P. Sutter, *Reliable Exfoliation of Large-Area High-Quality Flakes of Graphene and Other Two-Dimensional Materials,* ACS Nano **9**, 10612 (2015).

[42] P. J. Zomer, M. H. D. Guimarães, J. C. Brant, N. Tombros, and B. J. van Wees, *Fast pick up technique for high quality heterostructures of bilayer graphene and hexagonal boron nitride,* Applied Physics Letters **105**, 013101 (2014-07-07), arXiv:1403.0399 .

[43] F. Pizzocchero, L. Gammelgaard, B. S. Jessen, J. M. Caridad, L. Wang, J. Hone, P. Bøggild, and T. J. Booth, *The hot pick-up technique for batch assembly of van der Waals heterostructures,* Nature Communications **7** (2016), 10.1038/ncomms11894.

[44] S. Masubuchi, M. Morimoto, S. Morikawa, M. Onodera, Y. Asakawa, K. Watanabe, T. Taniguchi, and T. Machida, *Autonomous robotic searching and assembly of two-dimensional crystals to build van der Waals superlattices,* Nature Communications **9**, 1413 (2018-04-12).

[45] A. Castellanos-Gomez, M. Buscema, R. Molenaar, V. Singh, L. Janssen, H. S. J. van der Zant, and G. A. Steele, *Deterministic transfer of two-dimensional materials by all-dry viscoelastic stamping,* 2D Materials **1**, 011002 (2014-04-04).

[46] M. Buscema, D. J. Groenendijk, G. A. Steele, H. S. van der Zant, and A. Castellanos-Gomez, *Photovoltaic effect in few-layer black phosphorus PN junctions defined by local electrostatic gating,* Nature Communications **5** (2014), 10.1038/ncomms5651.

[47] X. Ma, Q. Liu, D. Xu, Y. Zhu, S. Kim, Y. Cui, L. Zhong, and M. Liu, *Capillary-force-assisted clean-stamp transfer of two-dimensional materials,* Nano Letters **17**, 6961 (2017).

[48] A. Jain, P. Bharadwaj, S. Heeg, M. Parzefall, T. Taniguchi, K. Watanabe, and L. Novotny, *Minimizing residues and strain in 2d materials transferred from PDMS,* Nanotechnology **29**, 265203 (2018).

[49] C. Guo, J. Pan, H. Li, T. Lin, P. Liu, C. Song, D. Wang, G. Mu, X. Lai, H. Zhang, W. Zhou, M. Chen, and F. Huang, *Observation of superconductivity in 1t'-mos2 nanosheets,* J. Mater. Chem. C **5**, 10855 (2017).

[50] R. Kappera, D. Voiry, S. E. Yalcin, W. Jen, M. Acerce, S. Torrel, B. Branch, S. Lei, W. Chen, S. Najmaei, J. Lou, P. M. Ajayan, G. Gupta, A. D. Mohite, and M. Chhowalla, *Metallic 1t phase source/drain electrodes for field effect transistors from chemical vapor deposited MoS $_2$,* APL Materials **2**, 092516 (2014).

[51] J. Kang, W. Liu, and K. Banerjee, *High-performance MoS $_2$ transistors with low-*

8

resistance molybdenum contacts, Applied Physics Letters **104**, 093106 (2014).

[52] C. D. English, G. Shine, V. E. Dorgan, K. C. Saraswat, and E. Pop, *Improved Contacts to MoS $_2$ Transistors by Ultra-High Vacuum Metal Deposition,* Nano Letters **16**, 3824 (2016).

[53] Y. Chai, R. Ionescu, S. Su, R. Lake, M. Ozkan, and C. S. Ozkan, *Making one-dimensional electrical contacts to molybdenum disulfide-based heterostructures through plasma etching: One-dimensional electrical contacts to Mo disulfide-based heterostructures,* physica status solidi (a) **213**, 1358 (2016).

[54] R. Pisoni, Y. Lee, H. Overweg, M. Eich, P. Simonet, K. Watanabe, T. Taniguchi, R. Gorbachev, T. Ihn, and K. Ensslin, *Quantized conductance and broken symmetry states in MoS $_2$ van der Waals heterostructures,* arXiv preprint arXiv:1701.08619 (2017).

[55] S. Xu, Z. Wu, H. Lu, Y. Han, G. Long, X. Chen, T. Han, W. Ye, Y. Wu, J. Lin, J. Shen, Y. Cai, Y. He, F. Zhang, R. Lortz, C. Cheng, and N. Wang, *Universal low-temperature Ohmic contacts for quantum transport in transition metal dichalcogenides,* 2D Materials **3**, 021007 (2016).

[56] R. Pisoni, Z. Lei, P. Back, M. Eich, H. Overweg, Y. Lee, K. Watanabe, T. Taniguchi, T. Ihn, and K. Ensslin, *Gate-tunable quantum dot in a high quality single layer MoS2 van der waals heterostructure,* Applied Physics Letters **112**, 123101 (2018-03-19).

[57] R. Pisoni, A. Kormányos, M. Brooks, Z. Lei, P. Back, M. Eich, H. Overweg, Y. Lee, P. Rickhaus, K. Watanabe, T. Taniguchi, A. Imamoglu, G. Burkard, T. Ihn, and K. Ensslin, *Interactions and magnetotransport through spin-valley coupled landau levels in monolayer MoS2,* Physical Review Letters **121** (2018), 10.1103/physrevlett.121.247701.

[58] N. Papadopoulos, K. Watanabe, T. Taniguchi, H. S. J. van der Zant, and G. A. Steele, *Weak localization in boron nitride encapsulated bilayer MoS2,* Physical Review B **99** (2019), 10.1103/physrevb.99.115414.

[59] J. R. Schaibley, H. Yu, G. Clark, P. Rivera, J. S. Ross, K. L. Seyler, W. Yao, and X. Xu, *Valleytronics in 2D materials,* Nature Reviews Materials **1**, 16055 (2016).

[60] T. Cheiwchanchamnangij and W. R. L. Lambrecht, *Quasiparticle band structure calculation of monolayer, bilayer, and bulk MoS $_2$,* Physical Review B **85** (2012).

[61] S. Wu, J. S. Ross, G.-B. Liu, G. Aivazian, A. Jones, Z. Fei, W. Zhu, D. Xiao, W. Yao, D. Cobden, and X. Xu, *Electrical tuning of valley magnetic moment through symmetry control in bilayer MoS2,* Nature Physics **9**, 149 (2013).

[62] J. Lee, K. F. Mak, and J. Shan, *Electrical control of the valley Hall effect in bilayer MoS2 transistors,* Nature Nanotechnology **11**, 421–425 (2016).

[63] J. Klein, J. Wierzbowski, A. Steinhoff, M. Florian, M. Rösner, F. Heimbach, K. Müller, F. Jahnke, T. O. Wehling, J. J. Finley, and M. Kaniber, *Electric-Field Switchable Second-Harmonic Generation in Bilayer MoS2 by Inversion Symmetry Breaking,*

8

Nano Lett. **17**, 392 (2017).

[64] G. Bergmann, *Weak localization in thin films: A time-of-flight experiment with conduction electrons,* Physics Reports **107**, 1 (1984).

[65] S. Kawaji, *Weak localization and negative magnetoresistance in semiconductor two-dimensional systems,* Surface Science **170**, 682 (1986).

[66] F. V. Tikhonenko, D. W. Horsell, R. V. Gorbachev, and A. K. Savchenko, *Weak Localization in Graphene Flakes,* Physical Review Letters **100** (2008).

[67] H. Schmidt, I. Yudhistira, L. Chu, A. H. Castro Neto, B. Özyilmaz, S. Adam, and G. Eda, *Quantum Transport and Observation of Dyakonov-Perel Spin-Orbit Scattering in Monolayer MoS 2,* Physical Review Letters **116** (2016).

[68] A. T. Neal, H. Liu, J. Gu, and P. D. Ye, *Magneto-transport in MoS2: Phase Coherence, Spin–Orbit Scattering, and the Hall Factor,* ACS Nano **7**, 7077 (2013).

[69] Y. J. Zhang, W. Shi, J. T. Ye, R. Suzuki, and Y. Iwasa, *Robustly protected carrier spin relaxation in electrostatically doped transition-metal dichalcogenides,* Physical Review B **95** (2017).

[70] S. Hikami, A. I. Larkin, and Y. Nagaoka, *Spin-orbit interaction and magnetoresistance in the two dimensional random system,* Progress of Theoretical Physics **63**, 707 (1980).

[71] B. L. Altshuler, A. G. Aronov, and D. E. Khmelnitsky, *Effects of electron-electron collisions with small energy transfers on quantum localisation,* J. Phys. C: Solid State Phys. **15**, 7367 (1982).

[72] X. Cui, G.-H. Lee, Y. D. Kim, G. Arefe, P. Y. Huang, C.-H. Lee, D. A. Chenet, X. Zhang, L. Wang, F. Ye, F. Pizzocchero, B. S. Jessen, K. Watanabe, T. Taniguchi, D. A. Muller, T. Low, P. Kim, and J. Hone, *Multi-terminal transport measurements of MoS2 using a van der Waals heterostructure device platform,* Nature Nanotechnology **10**, 534 (2015).

[73] F. Pizzocchero, L. Gammelgaard, B. S. Jessen, J. M. Caridad, L. Wang, J. Hone, P. Bøggild, and T. J. Booth, *The hot pick-up technique for batch assembly of van der Waals heterostructures,* Nature Communications **7**, 11894 (2016).

[74] K. Wang, K. De Greve, L. A. Jauregui, A. Sushko, A. High, Y. Zhou, G. Scuri, T. Taniguchi, K. Watanabe, M. D. Lukin, H. Park, and P. Kim, *Electrical control of charged carriers and excitons in atomically thin materials,* Nature Nanotechnology **13**, 128 (2018).

[75] K. Kaasbjerg, T. Low, and A.-P. Jauho, *Scattering by atomic vacancies in monolayer MoS2: Midgap states, symmetry and screening,* arXiv preprint arXiv:1612.00469 (2016).

[76] S. V. Iordanskii, Y. B. Lyanda-Geller, and G. E. Pikus, *Weak localization in quantum wells with spin-orbit interaction,* ZhETF Pisma Redaktsiiu **60**, 199 (1994).

[77] W. Knap, C. Skierbiszewski, A. Zduniak, E. Litwin-Staszewska, D. Bertho, F. Kobbi,

8

J. L. Robert, G. E. Pikus, F. G. Pikus, S. V. Iordanskii, V. Mosser, K. Zekentes, and Y. B. Lyanda-Geller, *Weak antilocalization and spin precession in quantum wells,* Physical Review B **53**, 3912 (1996-02-15).

[78] Y. Du, A. T. Neal, H. Zhou, and P. D. Ye, *Weak localization in few-layer black phosphorus,* 2D Materials **3**, 024003 (2016).

[79] R. V. Gorbachev, F. V. Tikhonenko, A. S. Mayorov, D. W. Horsell, and A. K. Savchenko, *Weak Localization in Bilayer Graphene,* Physical Review Letters **98** (2007).

[80] L. Wang and M. W. Wu, *Electron spin relaxation due to D'yakonov-Perel' and Elliot-Yafet mechanisms in monolayer MoS 2 : Role of intravalley and intervalley processes,* Physical Review B **89** (2014), 10.1103/PhysRevB.89.115302.

[81] S. Liang, H. Yang, P. Renucci, B. Tao, P. Laczkowski, S. Mc-Murtry, G. Wang, X. Marie, J.-M. George, S. Petit-Watelot, A. Djeffal, S. Mangin, H. Jaffrès, and Y. Lu, *Electrical spin injection and detection in molybdenum disulfide multilayer channel,* Nature Communications **8**, 14947 (2017).

[82] Z. Wang, A. Molina-Sánchez, P. Altmann, D. Sangalli, D. De Fazio, G. Soavi, U. Sassi, F. Bottegoni, F. Ciccacci, M. Finazzi, L. Wirtz, A. C. Ferrari, A. Marini, G. Cerullo, and S. Dal Conte, *Intravalley spin–flip relaxation dynamics in single-layer ws2,* Nano Letters **18**, 6882 (2018).

[83] H. Yuan, M. S. Bahramy, K. Morimoto, S. Wu, K. Nomura, B.-J. Yang, H. Shimotani, R. Suzuki, M. Toh, C. Kloc, X. Xu, R. Arita, N. Nagaosa, and Y. Iwasa, *Zeeman-type spin splitting controlled by an electric field,* Nature Physics **9**, 563 (2013).

[84] A. Kormányos, V. Zólyomi, V. I. Fal'ko, and G. Burkard, *Tunable Berry curvature, valley and spin Hall effect in Bilayer MoS$_2$,* arXiv:1804.06830 [cond-mat] (2018).

[85] J. Lin, T. Han, B. A. Piot, Z. Wu, S. Xu, G. Long, L. An, P. Cheung, P.-P. Zheng, P. Plochocka, X. Dai, D. K. Maude, F. Zhang, and N. Wang, *Determining interaction enhanced valley susceptibility in spin-valley-locked MoS2,* Nano Letters **19**, 1736 (2019).

[86] H. Ochoa and R. Roldán, *Spin-orbit-mediated spin relaxation in monolayer MoS2,* Physical Review B **87**, 245421 (2013).

[87] A. Kormányos, V. Zólyomi, N. D. Drummond, and G. Burkard, *Spin-Orbit Coupling, Quantum Dots, and Qubits in Monolayer Transition Metal Dichalcogenides,* Physical Review X **4** (2014).

[88] L. Yang, N. A. Sinitsyn, W. Chen, J. Yuan, J. Zhang, J. Lou, and S. A. Crooker, *Long-lived nanosecond spin relaxation and spin coherence of electrons in monolayer MoS_2 and WS_2,* Nature Physics **11**, 830 (2015).

[89] K. Kaasbjerg, K. S. Thygesen, and K. W. Jacobsen, *Phonon-limited mobility in n -type single-layer MoS 2 from first principles,* Physical Review B **85** (2012), 10.1103/PhysRevB.85.115317.

8

[90] N. Ma and D. Jena, *Charge Scattering and Mobility in Atomically Thin Semiconductors,* Physical Review X **4** (2014), 10.1103/PhysRevX.4.011043.

[91] J. O. Island, R. Biele, M. Barawi, J. M. Clamagirand, J. R. Ares, C. Sánchez, H. S. J. van der Zant, I. J. Ferrer, R. D'Agosta, and A. Castellanos-Gomez, *Titanium trisulfide (TiS3): A 2D semiconductor with quasi-1D optical and electronic properties,* Scientific Reports **6**, 22214 (2016).

[92] N. Papadopoulos, R. Frisenda, R. Biele, E. Flores, J. R. Ares, C. Sánchez, H. S. J. van der Zant, I. J. Ferrer, R. D'Agosta, and A. Castellanos-Gomez, *Large birefringence and linear dichroism in TiS3 nanosheets,* Nanoscale **10**, 12424 (2018).

[93] A. Lipatov, P. M. Wilson, M. Shekhirev, J. D. Teeter, R. Netusil, and A. Sinitskii, *Few-layered titanium trisulfide (TiS3) field-effect transistors,* Nanoscale **7**, 12291 (2015).

[94] J. O. Island, M. Barawi, R. Biele, A. Almazán, J. M. Clamagirand, J. R. Ares, C. Sánchez, H. S. J. van der Zant, J. V. Álvarez, R. D'Agosta, I. J. Ferrer, and A. Castellanos-Gomez, *TiS $_3$ Transistors with Tailored Morphology and Electrical Properties,* Advanced Materials **27**, 2595 (2015).

[95] A. J. Molina-Mendoza, J. O. Island, W. S. Paz, J. M. Clamagirand, J. R. Ares, E. Flores, F. Leardini, C. Sánchez, N. Agraït, G. Rubio-Bollinger, H. S. J. van der Zant, I. J. Ferrer, J. J. Palacios, and A. Castellanos-Gomez, *High Current Density Electrical Breakdown of TiS3 Nanoribbon-Based Field-Effect Transistors,* Advanced Functional Materials **27**, 1605647 (2017).

[96] J. O. Island, M. Buscema, M. Barawi, J. M. Clamagirand, J. R. Ares, C. Sánchez, I. J. Ferrer, G. A. Steele, H. S. J. van der Zant, and A. Castellanos-Gomez, *Ultrahigh Photoresponse of Few-Layer TiS3 Nanoribbon Transistors,* Advanced Optical Materials **2**, 641 (2014).

[97] S. Liu, W. Xiao, M. Zhong, L. Pan, X. Wang, H.-X. Deng, J. Liu, J. Li, and Z. Wei, *Highly polarization sensitive photodetectors based on quasi-1D titanium trisulfide (TiS3),* Nanotechnology **29**, 184002 (2018).

[98] J. Dai and X. C. Zeng, *Titanium Trisulfide Monolayer: Theoretical Prediction of a New Direct-Gap Semiconductor with High and Anisotropic Carrier Mobility,* Angew. Chem. Int. Ed. **54**, 7572 (2015).

[99] E. Finkman and B. Fisher, *Electrical transport measurements in TiS3,* Solid State Communications **50**, 25 (1984).

[100] I. G. Gorlova and V. Y. Pokrovskii, *Collective conduction mechanism in a quasi-one-dimensional TiS3 compound,* Jetp Lett. **90**, 295 (2009).

[101] I. G. Gorlova, V. Y. Pokrovskii, S. G. Zybtsev, A. N. Titov, and V. N. Timofeev, *Features of the conductivity of the quasi-one-dimensional compound TiS3,* Journal of Experimental and Theoretical Physics **111**, 298 (2010).

[102] P. Monceau, N. P. Ong, A. M. Portis, A. Meerschaut, and J. Rouxel, *Electric Field Breakdown of Charge-Density-Wave\char22{}Induced Anomalies in Nb$\{\mathrm{Se}}_{3}$,* Phys. Rev. Lett. **37**, 602 (1976).

8

[103] C. Felser, E. W. Finckh, H. Kleinke, F. Rocker, and W. Tremel, *Electronic properties of ZrTe3,* J. Mater. Chem. **8,** 1787 (1998).

[104] C. Huang, E. Zhang, X. Yuan, W. Wang, Y. Liu, C. Zhang, J. Ling, S. Liu, and F. Xiu, *Tunable charge density wave in TiS 3 nanoribbons,* Chinese Phys. B **26,** 067302 (2017).

[105] M. Randle, A. Lipatov, A. Kumar, C.-P. Kwan, J. Nathawat, B. Barut, S. Yin, K. He, N. Arabchigavkani, R. Dixit, T. Komesu, J. Avila, M. C. Asensio, P. A. Dowben, A. Sinitskii, U. Singisetti, and J. P. Bird, *Gate-Controlled Metal–Insulator Transition in TiS 3 Nanowire Field-Effect Transistors,* ACS Nano (2018).

[106] H. Qiu, T. Xu, Z. Wang, W. Ren, H. Nan, Z. Ni, Q. Chen, S. Yuan, F. Miao, F. Song, G. Long, Y. Shi, L. Sun, J. Wang, and X. Wang, *Hopping transport through defect-induced localized states in molybdenum disulphide,* Nature Communications **4,** 2642 (2013).

[107] N. R. Pradhan, D. Rhodes, S. Memaran, J. M. Poumirol, D. Smirnov, S. Talapatra, S. Feng, N. Perea-Lopez, A. L. Elias, M. Terrones, P. M. Ajayan, and L. Balicas, *Hall and field-effect mobilities in few layered p-WSe$_2$ field-effect transistors,* Scientific Reports **5,** 8979 (2015).

[108] F. Iyikanat, H. Sahin, R. T. Senger, and F. M. Peeters, *Vacancy Formation and Oxidation Characteristics of Single Layer TiS3,* J. Phys. Chem. C **119,** 10709 (2015).

[109] J. I.-J. Wang, Y. Yang, Y.-A. Chen, K. Watanabe, T. Taniguchi, H. O. H. Churchill, and P. Jarillo-Herrero, *Electronic Transport of Encapsulated Graphene and WSe2 Devices Fabricated by Pick-up of Prepatterned hBN,* Nano Lett. **15,** 1898 (2015).

[110] X. Chen, Y. Wu, Z. Wu, Y. Han, S. Xu, L. Wang, W. Ye, T. Han, Y. He, Y. Cai, and N. Wang, *High-quality sandwiched black phosphorus heterostructure and its quantum oscillations,* Nature Communications **6** (2015), 10.1038/ncomms8315.

[111] Z. Wu, S. Xu, H. Lu, A. Khamoshi, G.-B. Liu, T. Han, Y. Wu, J. Lin, G. Long, Y. He, Y. Cai, Y. Yao, F. Zhang, and N. Wang, *Even–odd layer-dependent magnetotransport of high-mobility q-valley electrons in transition metal disulfides,* Nature Communications **7** (2016), 10.1038/ncomms12955.

[112] N. Kodama, T. Hasegawa, Y. Okawa, T. Tsuruoka, C. Joachim, and M. Aono, *Electronic States of Sulfur Vacancies Formed on a MoS2 Surface,* Jpn. J. Appl. Phys. **49,** 08LB01 (2010).

[113] I. S. Kim, V. K. Sangwan, D. Jariwala, J. D. Wood, S. Park, K.-S. Chen, F. Shi, F. Ruiz-Zepeda, A. Ponce, M. Jose-Yacaman, V. P. Dravid, T. J. Marks, M. C. Hersam, and L. J. Lauhon, *Influence of Stoichiometry on the Optical and Electrical Properties of Chemical Vapor Deposition Derived MoS2,* ACS Nano **8,** 10551 (2014).

[114] S.-S. Chee, C. Oh, M. Son, G.-C. Son, H. Jang, T. J. Yoo, S. Lee, W. Lee, J. Y. Hwang, H. Choi, B. H. Lee, and M.-H. Ham, *Sulfur vacancy-induced reversible doping of transition metal disulfides via hydrazine treatment,* Nanoscale **9,** 9333 (2017).

[115] K. Kaasbjerg, K. S. Thygesen, and A.-P. Jauho, *Acoustic phonon limited mobility in*

8

two-dimensional semiconductors: Deformation potential and piezoelectric scattering in monolayer mos$_2$ from first principles, Phys. Rev. B **87**, 235312 (2013).

[116] C. Kittel, *Introduction to Solid State Physics*, 8th ed. (Wiley, 2004).

[117] H. Ibach and H. Lüth, *Solid-State Physics: An Introduction to Principles of Materials Science*, 4th ed. (Springer-Verlag, 2009).

[118] N. R. Pradhan, D. Rhodes, S. Memaran, J. M. Poumirol, D. Smirnov, S. Talapatra, S. Feng, N. Perea-Lopez, A. L. Elias, M. Terrones, P. M. Ajayan, and L. Balicas, *Hall and field-effect mobilities in few layered* p*-WSe$_2$ field-effect transistors,* Scientific Reports **5**, 8979 (2015).

[119] D. C. Look, C. E. Stutz, J. R. Sizelove, and K. R. Evans, *On hall scattering factors for holes in GaAs,* Journal of Applied Physics **80**, 1913 (1996).

[120] G. Grüner, *The dynamics of charge-density waves,* Rev. Mod. Phys. **60**, 1129 (1988).

[121] S. Marianer and B. I. Shklovskii, *Effective temperature of hopping electrons in a strong electric field,* Physical Review B **46**, 13100 (1992).

[122] R. Kurita, *Current Modulation of Charge-Density-Wave Field-Effect Transistors with NbSe 3 Channel,* Journal of the Physical Society of Japan **69**, 2604 (2000).

[123] H. S. J. van der Zant, E. Slot, S. V. Zaitsev-Zotov, and S. N. Artemenko, *Negative Resistance and Local Charge-Density-Wave Dynamics,* Physical Review Letters **87** (2001).

[124] E. Slot, M. A. Holst, H. S. J. van der Zant, and S. V. Zaitsev-Zotov, *One-dimensional conduction in Charge-Density Wave nanowires,* Physical Review Letters **93** (2004).

[125] L. J. Li, E. C. T. O'Farrell, K. P. Loh, G. Eda, B. Özyilmaz, and A. H. Castro Neto, *Controlling many-body states by the electric-field effect in a two-dimensional material,* Nature **529**, 185 (2016).

[126] P. Monçeau, N. P. Ong, A. M. Portis, A. Meerschaut, and J. Rouxel, *Electric Field Breakdown of Charge-Density-Wave—Induced Anomalies in Nb Se 3,* Physical Review Letters **37**, 602 (1976).

[127] X. Xi, H. Berger, L. Forró, J. Shan, and K. F. Mak, *Gate Tuning of Electronic Phase Transitions in Two-Dimensional NbSe_{2},* Phys. Rev. Lett. **117**, 106801 (2016).

[128] F. Tremblay, M. Pepper, R. Newbury, D. Ritchie, D. C. Peacock, J. E. F. Frost, G. A. C. Jones, and G. Hill, *Activationless hopping of correlated electrons in n-type GaAs,* Physical Review B **40**, 3387 (1989).

[129] N. Papadopoulos, G. A. Steele, and H. S. J. van der Zant, *Efros-Shklovskii variable range hopping and nonlinear transport in 1T/1T'-MoS2,* Phys. Rev. B **96**, 235436 (2017).

[130] K. F. Mak, C. Lee, J. Hone, J. Shan, and T. F. Heinz, *Atomically Thin MoS_{2}: A New Direct-Gap Semiconductor,* Physical Review Letters **105**, 136805 (2010).

8

[131] O. Lopez-Sanchez, D. Lembke, M. Kayci, A. Radenovic, and A. Kis, *Ultrasensitive photodetectors based on monolayer MoS2,* Nature Nanotechnology **8**, 497 (2013).

[132] T. Cao, G. Wang, W. Han, H. Ye, C. Zhu, J. Shi, Q. Niu, P. Tan, E. Wang, B. Liu, and J. Feng, *Valley-selective circular dichroism of monolayer molybdenum disulphide,* Nature Communications **3**, 887 (2012).

[133] F. Wypych and R. Schöllhorn, *1t-MoS2, a new metallic modification of molybdenum disulfide,* Journal of the Chemical Society, Chemical Communications , 1386 (1992).

[134] S. J. Sandoval, D. Yang, R. F. Frindt, and J. C. Irwin, *Raman study and lattice dynamics of single molecular layers of MoS 2,* Physical Review B **44**, 3955 (1991).

[135] X. R. Qin, D. Yang, R. F. Frindt, and J. C. Irwin, *Real-space imaging of single-layer MoS 2 by scanning tunneling microscopy,* Physical Review B **44**, 3490 (1991).

[136] X. Qian, J. Liu, L. Fu, and J. Li, *Quantum spin Hall effect in two-dimensional transition metal dichalcogenides,* Science , 1256815 (2014).

[137] T. Hu, R. Li, and J. Dong, *A new (2 × 1) dimerized structure of monolayer 1t-molybdenum disulfide, studied from first principles calculations,* The Journal of Chemical Physics **139**, 174702 (2013).

[138] N. Imanishi, M. Toyoda, Y. Takeda, and O. Yamamoto, *Study on lithium intercalation into MoS2,* Solid State Ionics **58**, 333 (1992).

[139] Y. Katagiri, T. Nakamura, A. Ishii, C. Ohata, M. Hasegawa, S. Katsumoto, T. Cusati, A. Fortunelli, G. Iannaccone, G. Fiori, S. Roche, and J. Haruyama, *Gate-Tunable Atomically Thin Lateral MoS 2 Schottky Junction Patterned by Electron Beam,* Nano Letters **16**, 3788 (2016).

[140] A. N. Enyashin, L. Yadgarov, L. Houben, I. Popov, M. Weidenbach, R. Tenne, M. Bar-Sadan, and G. Seifert, *New Route for Stabilization of 1t-WS2 and MoS2 Phases,* The Journal of Physical Chemistry C **115**, 24586 (2011).

[141] Y.-C. Lin, D. O. Dumcenco, Y.-S. Huang, and K. Suenaga, *Atomic mechanism of the semiconducting-to-metallic phase transition in single-layered MoS2,* Nature Nanotechnology **9**, 391 (2014).

[142] G. Eda, T. Fujita, H. Yamaguchi, D. Voiry, M. Chen, and M. Chhowalla, *Coherent Atomic and Electronic Heterostructures of Single-Layer MoS 2,* ACS Nano **6**, 7311 (2012).

[143] J. S. Kim, J. Kim, J. Zhao, S. Kim, J. H. Lee, Y. Jin, H. Choi, B. H. Moon, J. J. Bae, Y. H. Lee, and S. C. Lim, *Electrical Transport Properties of Polymorphic MoS2,* ACS Nano **10**, 7500 (2016).

[144] A. Castellanos-Gomez, M. Buscema, R. Molenaar, V. Singh, L. Janssen, H. S. J. van der Zant, and G. A. Steele, *Deterministic transfer of two-dimensional materials by all-dry viscoelastic stamping,* 2D Materials **1**, 011002 (2014).

[145] D. Voiry, M. Salehi, R. Silva, T. Fujita, M. Chen, T. Asefa, V. B. Shenoy, G. Eda, and

8

M. Chhowalla, *Conducting MoS2 Nanosheets as Catalysts for Hydrogen Evolution Reaction,* Nano Letters **13**, 6222 (2013).

[146] V. F. Gantmakher, *Electrons and disorder in solids,* Oxford science publications No. 130 (Oxford University Press, Oxford : Oxford ; New York, 2005).

[147] N. F. Mott, *Conduction in non-crystalline materials: III. Localized states in a pseudogap and near extremities of conduction and valence bands,* Philosophical Magazine **19**, 835 (1969).

[148] A. L. Efros and B. I. Shklovskii, *Coulomb gap and low temperature conductivity of disordered systems,* Journal of Physics C: Solid State Physics **8**, L49 (1975).

[149] D. Joung and S. I. Khondaker, *Efros-Shklovskii variable-range hopping in reduced graphene oxide sheets of varying carbon sp^{2} fraction,* Physical Review B **86**, 235423 (2012).

[150] C.-I. Liu, B.-Y. Wu, C. Chuang, Y.-C. Lee, Y.-J. Ho, Y. Yang, R. E. Elmquist, S.-T. Lo, and C.-T. Liang, *Variable range hopping and nonlinear transport in monolayer epitaxial graphene grown on SiC,* Semiconductor Science and Technology **31**, 105008 (2016).

[151] B. Shklovskii, *HOPPING CONDUCTION IN SEMICONDUCTORS SUBJECTED TO A STRONG ELECTRIC FIELD.* Sov. Phys. Semiconductors **6**, 1964 (1973).

[152] A. V. Dvurechenskii, V. A. Dravin, and A. I. Yakimiv, *Activationless hopping conductivity along the states of the Coulomb gap in a-Si<Mn>,* JETP Letters **48**, 155 (1988).

[153] D. Yu, C. Wang, B. L. Wehrenberg, and P. Guyot-Sionnest, *Variable Range Hopping Conduction in Semiconductor Nanocrystal Solids,* Physical Review Letters **92** (2004).

[154] B. I. Shklovskii and A. L. Efros, *Electronic Properties of Doped Semiconductors* (Springer-Verlag, Berlin, 1984).

[155] S.-L. Li, K. Tsukagoshi, E. Orgiu, and P. Samorì, *Charge transport and mobility engineering in two-dimensional transition metal chalcogenide semiconductors,* Chem. Soc. Rev. **45**, 118 (2016).

[156] L. V. Keldysh, *Coulomb interaction in thin semiconductor and semimetal films,* JETP Letters: issues online **29**, 658 (1979).

[157] I. S. Beloborodov, A. V. Lopatin, and V. M. Vinokur, *Coulomb effects and hopping transport in granular metals,* Physical Review B **72**, 125121 (2005).

[158] D. Joung, L. Zhai, and S. I. Khondaker, *Coulomb blockade and hopping conduction in graphene quantum dots array,* Physical Review B **83**, 115323 (2011).

[159] L. Britnell, R. V. Gorbachev, R. Jalil, B. D. Belle, F. Schedin, A. Mishchenko, T. Georgiou, M. I. Katsnelson, L. Eaves, S. V. Morozov, N. M. R. Peres, J. Leist, A. K. Geim, K. S. Novoselov, and L. A. Ponomarenko, *Field-effect tunneling transistor based on vertical graphene heterostructures,* Science **335**, 947 (2012).

[160] J. Jang, H. M. Yoo, L. N. Pfeiffer, K. W. West, K. W. Baldwin, and R. C. Ashoori,

Full momentum- and energy-resolved spectral function of a 2d electronic system, Science **358**, 901 (2017).

[161] E. E. Vdovin, A. Mishchenko, M. T. Greenaway, M. J. Zhu, D. Ghazaryan, A. Misra, Y. Cao, S. V. Morozov, O. Makarovsky, A. Patanè, G. J. Slotman, M. I. Katsnelson, A. K. Geim, K. S. Novoselov, and L. Eaves, *Phonon-assisted resonant tunneling of electrons in graphene-boron nitride transistors,* Physical Review Letters **116** (2016), 10.1103/PhysRevLett.116.186603, arXiv:1512.02143 .

[162] S. de Vega and F. J. G. de Abajo, *Plasmon generation through electron tunneling in graphene,* ACS Photonics **4**, 2367 (2017).

[163] D. Ghazaryan, M. T. Greenaway, Z. Wang, V. H. Guarochico-Moreira, I. J. Vera-Marun, J. Yin, Y. Liao, S. V. Morozov, O. Kristanovski, A. I. Lichtenstein, M. I. Katsnelson, F. Withers, A. Mishchenko, L. Eaves, A. K. Geim, K. S. Novoselov, and A. Misra, *Magnon-assisted tunnelling in van der waals heterostructures based on CrBr3,* Nature Electronics **1**, 344 (2018).

[164] J. R. Wallbank, D. Ghazaryan, A. Misra, Y. Cao, J. S. Tu, B. A. Piot, M. Potemski, S. Pezzini, S. Wiedmann, U. Zeitler, T. L. M. Lane, S. V. Morozov, M. T. Greenaway, L. Eaves, A. K. Geim, V. I. Fal'ko, K. S. Novoselov, and A. Mishchenko, *Tuning the valley and chiral quantum state of Dirac electrons in van der Waals heterostructures,* Science **353**, 575 (2016), 27493182 .

[165] J. Eisenstein, L. Pfeiffer, and K. West, *Quantum hall spin diode,* Physical Review Letters **118** (2017), 10.1103/physrevlett.118.186801.

[166] K. Kim, N. Prasad, H. C. P. Movva, G. W. Burg, Y. Wang, S. Larentis, T. Taniguchi, K. Watanabe, L. F. Register, and E. Tutuc, *Spin-conserving resonant tunneling in twist-controlled WSe2-hBN-WSe2 heterostructures,* Nano Letters **18**, 5967 (2018).

[167] S. Becker, C. Karrasch, T. Mashoff, M. Pratzer, M. Liebmann, V. Meden, and M. Morgenstern, *Probing Electron-Electron Interaction in Quantum Hall Systems with Scanning Tunneling Spectroscopy,* Physical Review Letters **106** (2011), 10.1103/PhysRevLett.106.156805.

[168] U. Chandni, K. Watanabe, T. Taniguchi, and J. P. Eisenstein, *Signatures of phonon and defect-assisted tunneling in planar metal-hexagonal boron nitride-graphene junctions,* Nano Letters **16**, 7982 (2016).

[169] M. T. Greenaway, E. E. Vdovin, D. Ghazaryan, A. Misra, A. Mishchenko, Y. Cao, Z. Wang, J. R. Wallbank, M. Holwill, Y. Khanin, S. V. Morozov, K. Watanabe, T. Taniguchi, O. Makarovsky, T. M. Fromhold, A. Patanè, A. K. Geim, V. I. Fal'ko, K. S. Novoselov, and L. Eaves, *Tunnel spectroscopy of localised electronic states in hexagonal boron nitride,* Communications Physics **1** (2018), 10.1038/s42005-018-0097-1.

[170] B. Radisavljevic, A. Radenovic, J. Brivio, V. Giacometti, and A. Kis, *Single-layer MoS2 transistors,* Nature Nanotechnology **6**, 147 (2011).

[171] D. Ovchinnikov, A. Allain, Y.-S. Huang, D. Dumcenco, and A. Kis, *Electrical transport properties of single-layer WS2,* ACS Nano **8**, 8174 (2014).

8

[172] Y.-C. Lin, R. K. Ghosh, R. Addou, N. Lu, S. M. Eichfeld, H. Zhu, M.-Y. Li, X. Peng, M. J. Kim, L.-J. Li, R. M. Wallace, S. Datta, and J. A. Robinson, *Atomically thin resonant tunnel diodes built from synthetic van der waals heterostructures,* Nature Communications **6** (2015), 10.1038/ncomms8311.

[173] T. Georgiou, R. Jalil, B. D. Belle, L. Britnell, R. V. Gorbachev, S. V. Morozov, Y.-J. Kim, A. Gholinia, S. J. Haigh, O. Makarovsky, L. Eaves, L. A. Ponomarenko, A. K. Geim, K. S. Novoselov, and A. Mishchenko, *Vertical field-effect transistor based on graphene–WS$_2$ heterostructures for flexible and transparent electronics,* Nature Nanotechnology **8**, 100 (2013).

[174] A. V. Kretinin, Y. Cao, J. S. Tu, G. L. Yu, R. Jalil, K. S. Novoselov, S. J. Haigh, A. Gholinia, A. Mishchenko, M. Lozada, T. Georgiou, C. R. Woods, F. Withers, P. Blake, G. Eda, A. Wirsig, C. Hucho, K. Watanabe, T. Taniguchi, A. K. Geim, and R. V. Gorbachev, *Electronic properties of graphene encapsulated with different two-dimensional atomic crystals,* Nano Letters **14**, 3270 (2014).

[175] T. Dvir, F. Massee, L. Attias, M. Khodas, M. Aprili, C. H. L. Quay, and H. Steinberg, *Spectroscopy of bulk and few-layer superconducting NbSe2 with van der waals tunnel junctions,* Nature Communications **9** (2018), 10.1038/s41467-018-03000-w.

[176] X.-G. Li, Y.-P. Wang, J. N. Fry, X.-G. Zhang, and H.-P. Cheng, *Tunneling field-effect junctions with WS 2 barrier,* Journal of Physics and Chemistry of Solids (2017), 10.1016/j.jpcs.2017.12.005.

[177] A. Avsar, J. Y. Tan, T. Taychatanapat, J. Balakrishnan, G. Koon, Y. Yeo, J. Lahiri, A. Carvalho, A. S. Rodin, E. O'Farrell, G. Eda, A. H. C. Neto, and B. Özyilmaz, *Spin–orbit proximity effect in graphene,* Nature Communications **5** (2014), 10.1038/ncomms5875.

[178] A. Raja, A. Chaves, J. Yu, G. Arefe, H. M. Hill, A. F. Rigosi, T. C. Berkelbach, P. Nagler, C. Schüller, T. Korn, C. Nuckolls, J. Hone, L. E. Brus, T. F. Heinz, D. R. Reichman, and A. Chernikov, *Coulomb engineering of the bandgap and excitons in two-dimensional materials,* Nature Communications **8**, 15251 (2017).

[179] X.-X. Song, Z.-Z. Zhang, J. You, D. Liu, H.-O. Li, G. Cao, M. Xiao, and G.-P. Guo, *Temperature dependence of coulomb oscillations in a few-layer two-dimensional WS2 quantum dot,* Scientific Reports **5** (2015), 10.1038/srep16113.

[180] J. O. Island, G. A. Steele, H. S. J. van der Zant, and A. Castellanos-Gomez, *Thickness dependent interlayer transport in vertical MoS2josephson junctions,* 2D Materials **3**, 031002 (2016).

[181] L. Bretheau, J. I.-J. Wang, R. Pisoni, K. Watanabe, T. Taniguchi, and P. Jarillo-Herrero, *Tunnelling spectroscopy of Andreev states in graphene,* Nature Physics **13**, 756 (2017).

[182] M. T. Greenaway, E. E. Vdovin, D. Ghazaryan, A. Misra, A. Mishchenko, Y. Cao, Z. Wang, J. R. Wallbank, M. Holwill, Y. Khanin, S. V. Morozov, K. Watanabe, T. Taniguchi, O. Makarovsky, T. M. Fromhold, A. Patanè, A. K. Geim, V. I. Fal'ko, K. S. Novoselov, and L. Eaves, *Tunnel spectroscopy of localised electronic states in*

8

hexagonal boron nitride, Communications Physics **1** (2018), 10.1038/s42005-018-0097-1.

[183] J. M. Thijssen and H. S. J. V. der Zant, *Charge transport and single-electron effects in nanoscale systems,* physica status solidi (b) **245**, 1455 (2008).

[184] J. G. Simmons, *Generalized formula for the electric tunnel effect between similar electrodes separated by a thin insulating film,* Journal of Applied Physics **34**, 1793 (1963).

[185] D. Sarkar, X. Xie, W. Liu, W. Cao, J. Kang, Y. Gong, S. Kraemer, P. M. Ajayan, and K. Banerjee, *A subthermionic tunnel field-effect transistor with an atomically thin channel,* Nature **526**, 91 (2015).

[186] P. Gehring, J. K. Sowa, J. Cremers, Q. Wu, H. Sadeghi, Y. Sheng, J. H. Warner, C. J. Lambert, G. A. D. Briggs, and J. A. Mol, *Distinguishing Lead and Molecule States in Graphene-Based Single-Electron Transistors,* ACS Nano **11**, 5325 (2017).

[187] S. Zihlmann, P. Makk, S. Castilla, J. Gramich, K. Thodkar, S. Caneva, R. Wang, S. Hofmann, and C. Schönenberger, *Nonequilibrium properties of graphene probed by superconducting tunnel spectroscopy,* Physical Review B **99** (2019), 10.1103/physrevb.99.075419.

[188] E. D. Minot, Y. Yaish, V. Sazonova, and P. L. McEuen, *Determination of electron orbital magnetic moments in carbon nanotubes,* Nature **428**, 536 (2004).

[189] J. O. Island, M. Ostermann, L. Aspitarte, E. D. Minot, D. Varsano, E. Molinari, M. Rontani, and G. A. Steele, *Interaction-Driven Giant Orbital Magnetic Moments in Carbon Nanotubes,* Physical Review Letters **121** (2018), 10.1103/PhysRevLett.121.127704.

[190] I. Aharonovich, D. Englund, and M. Toth, *Solid-state single-photon emitters,* Nature Photonics **10**, 631 (2016).

[191] V. Perebeinos, *Two dimensions and one photon,* Nature Nanotechnology **10**, 485 (2015).

[192] C. Li, P. Zhou, and D. W. Zhang, *Devices and applications of van der waals heterostructures,* Journal of Semiconductors **38**, 031005 (2017).

[193] M. Gibertini, M. Koperski, A. F. Morpurgo, and K. S. Novoselov, *Magnetic 2d materials and heterostructures,* Nature Nanotechnology **14**, 408 (2019).

[194] C. R. Woods, L. Britnell, A. Eckmann, R. S. Ma, J. C. Lu, H. M. Guo, X. Lin, G. L. Yu, Y. Cao, R. V. Gorbachev, A. V. Kretinin, J. Park, L. A. Ponomarenko, M. I. Katsnelson, Y. N. Gornostyrev, K. Watanabe, T. Taniguchi, C. Casiraghi, H.-J. Gao, A. K. Geim, and K. S. Novoselov, *Commensurate–incommensurate transition in graphene on hexagonal boron nitride,* Nature Physics **10**, 451 (2014).

[195] M. Yankowitz, Q. Ma, P. Jarillo-Herrero, and B. J. LeRoy, *van der waals heterostructures combining graphene and hexagonal boron nitride,* Nature Reviews Physics **1**, 112 (2019).

8

[196] C. Jang, S. Adam, J.-H. Chen, E. D. Williams, S. D. Sarma, and M. S. Fuhrer, *Tuning the effective fine structure constant in graphene: Opposing effects of dielectric screening on short- and long-range potential scattering,* Physical Review Letters **101** (2008), 10.1103/physrevlett.101.146805.

[197] G. L. Yu, R. Jalil, B. Belle, A. S. Mayorov, P. Blake, F. Schedin, S. V. Morozov, L. A. Ponomarenko, F. Chiappini, S. Wiedmann, U. Zeitler, M. I. Katsnelson, A. K. Geim, K. S. Novoselov, and D. C. Elias, *Interaction phenomena in graphene seen through quantum capacitance,* Proceedings of the National Academy of Sciences **110**, 3282 (2013).

[198] A. W. Cummings, J. H. Garcia, J. Fabian, and S. Roche, *Giant spin lifetime anisotropy in graphene induced by proximity effects,* Physical Review Letters **119** (2017), 10.1103/physrevlett.119.206601.

[199] M. Gmitra and J. Fabian, *Proximity effects in bilayer graphene on monolayer WSe2 : Field-effect spin valley locking, spin-orbit valve, and spin transistor,* Physical Review Letters **119** (2017), 10.1103/physrevlett.119.146401.

[200] S. Omar and B. J. van Wees, *Spin transport in high-mobility graphene on WS2 substrate with electric-field tunable proximity spin-orbit interaction,* Physical Review B **97** (2018), 10.1103/physrevb.97.045414.

[201] I. Žutić, A. Matos-Abiague, B. Scharf, H. Dery, and K. Belashchenko, *Proximitized materials,* Materials Today **22**, 85 (2019).

[202] S. Jung, N. Myoung, J. Park, T. Y. Jeong, H. Kim, K. Watanabe, T. Taniguchi, D. H. Ha, C. Hwang, and H. C. Park, *Direct probing of the electronic structures of single-layer and bilayer graphene with a hexagonal boron nitride tunneling barrier,* Nano Letters **17**, 206 (2016).

[203] J. Yin, S. Slizovskiy, Y. Cao, S. Hu, Y. Yang, I. Lobanova, B. A. Piot, S.-K. Son, S. Ozdemir, T. Taniguchi, K. Watanabe, K. S. Novoselov, F. Guinea, A. K. Geim, V. Fal'ko, and A. Mishchenko, *Dimensional reduction, quantum hall effect and layer parity in graphite films,* Nature Physics **15**, 437 (2019).

[204] Y. Zhang, V. W. Brar, F. Wang, C. Girit, Y. Yayon, M. Panlasigui, A. Zettl, and M. F. Crommie, *Giant phonon-induced conductance in scanning tunnelling spectroscopy of gate-tunable graphene,* Nature Physics **4**, 627 (2008).

[205] A. Mishchenko, J. S. Tu, Y. Cao, R. V. Gorbachev, J. R. Wallbank, M. T. Greenaway, V. E. Morozov, S. V. Morozov, M. J. Zhu, S. L. Wong, F. Withers, C. R. Woods, Y.-J. Kim, K. Watanabe, T. Taniguchi, E. E. Vdovin, O. Makarovsky, T. M. Fromhold, V. I. Fal'ko, A. K. Geim, L. Eaves, and K. S. Novoselov, *Twist-controlled resonant tunnelling in graphene/boron nitride/graphene heterostructures,* Nature Nanotechnology **9**, 808 (2014).

[206] C. Ast, *Extracting the rashba splitting from scanning tunneling microscopy measurements,* Journal of Electron Spectroscopy and Related Phenomena **201**, 30 (2015).

[207] Z. Wang, D.-K. Ki, J. Y. Khoo, D. Mauro, H. Berger, L. S. Levitov, and A. F.

Morpurgo, *Origin and magnitude of 'designer' spin-orbit interaction in graphene on semiconducting transition metal dichalcogenides,* Physical Review X **6** (2016), 10.1103/physrevx.6.041020.

[208] B. Yang, M. Lohmann, D. Barroso, I. Liao, Z. Lin, Y. Liu, L. Bartels, K. Watanabe, T. Taniguchi, and J. Shi, *Strong electron-hole symmetric rashba spin-orbit coupling in graphene/monolayer transition metal dichalcogenide heterostructures,* Physical Review B **96** (2017), 10.1103/physrevb.96.041409.

[209] T. Völkl, T. Rockinger, M. Drienovsky, K. Watanabe, T. Taniguchi, D. Weiss, and J. Eroms, *Magnetotransport in heterostructures of transition metal dichalcogenides and graphene,* Physical Review B **96** (2017), 10.1103/physrevb.96.125405.

[210] M. Gmitra, D. Kochan, P. Högl, and J. Fabian, *Trivial and inverted dirac bands and the emergence of quantum spin hall states in graphene on transition-metal dichalcogenides,* Physical Review B **93** (2016), 10.1103/physrevb.93.155104.

[211] J. O. Island, X. Cui, C. Lewandowski, J. Y. Khoo, E. M. Spanton, H. Zhou, D. Rhodes, J. C. Hone, T. Taniguchi, K. Watanabe, L. S. Levitov, M. P. Zaletel, and A. F. Young, *Spin-orbit driven band inversion in bilayer graphene by van der waals proximity effect,* (2019), arXiv:1901.01332 .

[212] M. Yankowitz, J. Xue, D. Cormode, J. D. Sanchez-Yamagishi, K. Watanabe, T. Taniguchi, P. Jarillo-Herrero, P. Jacquod, and B. J. LeRoy, *Emergence of super-lattice dirac points in graphene on hexagonal boron nitride,* Nature Physics **8**, 382 (2012).

[213] Z.-G. Chen, Z. Shi, W. Yang, X. Lu, Y. Lai, H. Yan, F. Wang, G. Zhang, and Z. Li, *Observation of an intrinsic bandgap and landau level renormalization in graphene/boron-nitride heterostructures,* Nature Communications **5** (2014), 10.1038/ncomms5461.

[214] A. F. Young, C. R. Dean, L. Wang, H. Ren, P. Cadden-Zimansky, K. Watanabe, T. Taniguchi, J. Hone, K. L. Shepard, and P. Kim, *Spin and valley quantum hall ferromagnetism in graphene,* Nature Physics **8**, 550 (2012).

[215] J. Kondo, *Resistance minimum in dilute magnetic alloys,* Progress of Theoretical Physics **32**, 37 (1964).

[216] G. W. Burg, N. Prasad, K. Kim, T. Taniguchi, K. Watanabe, A. H. MacDonald, L. F. Register, and E. Tutuc, *Strongly enhanced tunneling at total charge neutrality in double-bilayer graphene- WSe2 heterostructures,* Physical Review Letters **120** (2018), 10.1103/physrevlett.120.177702.

[217] B. Fallahazad, H. C. P. Movva, K. Kim, S. Larentis, T. Taniguchi, K. Watanabe, S. K. Banerjee, and E. Tutuc, *Shubnikov–de Haas Oscillations of High-Mobility Holes in Monolayer and Bilayer WSe 2 : Landau Level Degeneracy, Effective Mass, and Negative Compressibility,* Physical Review Letters **116** (2016), 10.1103/Phys-RevLett.116.086601.

8

ACKNOWLEDGMENTS

I believe that you know that this is the point where this thesis comes to an end and it is the right moment to thank all those who contributed in making this possible, but also in making the last four years at the group of M.E.D and later on at the department of Quantum Nanoscience, fun and interesting.

I will start with the person that made all this possible. The creator of M.E.D and Quantum Nanoscience, Prof. Dr. Herre S. J. van der Zant. **Herre**, thank you for giving me the job and not firing me after 'losing' 600 L of helium on one of the first cooling down. I feel grateful that I was your student, because of your experience, because you accepted me in your lab and also made accessible to me anything that I needed. I also want to thank you for your meticulous corrections on my writings. I am grateful for your guidance and your transmittable relaxed way of seeing things. You are a true ‘δασκαλος’ (teacher).

Having one supervisor is not enough. I am happy that I had two supervisors with complimentary skills. **Gary**, you always amaze me with your knowledge on many different topics on physics, but especially on technical matters. Even more impressive is your ability to manage the enormously expanding Steele-lab group. You always want to investigate difficult but interesting topics. I feel lucky that my supervisor has all these skills and qualities and is such a role model (some people get scared though). I want to thank you especially, for helping me heal my publish-or-perish anxiety and made me finally see experimental physics as an exploration of the unknown and not a hunt for many publications. Lastly, I thank you because when I decided to stir the research on quantum transport physics, you accepted and got even excited, and made it more fun than it could be.

I want to thank all the committee members **Ferdinand**, **Peter**, **Justin**, **Marcus** and **Riccardo** for taking part in the assessment of this thesis and joining the lovely Dutch Ph.D. defense ceremony.

It is funny how fate works. During my interview, I met a young fella, who by the way I met also on my first day at work. This fellow, became my best friend in this land and during the exploration of the 'flatlands'. **Dejan** thank you for helping me with many of my struggles with my research and in life. Thank you for sharing your wisdom on how to joyfully navigate a Ph.D., conference visits and administration challenges included. If it weren't for you I would never have had the opportunity to be part of the great M.E.D. gang for the first 2 years and gain so many friends for life, you are the glue that sticks us all together still. I also have to thank you for giving me a platform to show off and improve my BBQ skills in your backyard as well as keep up with the yearly Rakia intake. Keep being kind with chivalry, and throw more often your dirty jokes. It was a great journey brat!

Do not underestimate his origins. He enjoys beer, fun and music more than the Southern people. We started almost together and I was finding him in the lab looking

at my data and asking me question about them. **Holger** is genuinely curious and his critical thinking helped me understand my problem more than I could imagine. During nights with spirits he would bring a conversation to the point that would sound like a Ph.D. defense ceremony. Pal you made experiments as well as nights with fire in the forest more fun and interesting. Good luck with your next steps in you career and life.

Next I would like to thank my students, both talented on different aspects. Although they worked on different projects than the ones written here, they helped me develop as a person and taught me that good supervision needs patience and management. **Elise** thank you for being a great student and doing all the work with the metal-organic perovskites it was fun working with you. Good luck with the internship and your future career. **Daan** thank you also for being my student in your bachelor project, you surprised me many times with your skills on measurements and electronic equipment, and I realized that you can be a successful experimental researcher.

Joshua I still remember the day that Herre asked for your opinion on my first project, as well as when you were trying to exfoliate boron nitride for your Josephson junctions. I was happy that we collaborated and you assisted me in a few projects. I was not surprised by your amazing results from your work in Santa Barbara. You understand and love science like no other. You gave me two advises from which one pushed me in the direction of transport measurements at low temperatures and the other made me realize that a publication is not as tough as it seems (especially in the world of 2D materials). I am sure that as a group leader and later on as professor you will do great things.

When you first meet him you can not understand half of what he says. You see, his super-Italian accent makes it very difficult. Always relaxed, he is the king of the molecules. **Riccardo**, thank you for the great moments in Delft, Groningen, Madrid and Rome. It was great fun to work with you in the lab, I still miss it! I am happy that we managed to have a few papers together too. I will never forget how fast you welcomed me in the gang in M.E.D, as well as how great host you were in Madrid.

Max I took care of your ANIMAL man. Thank you for helping me with many experiments in the beginning and also being the responsible one with the fridge. I admire your vision and the way you see things with pragmatism. I am happy that we have an annual tradition and we can see each other even though we do not work together anymore.

In the history of science, there were some couples that changed the course of history, see for example Marie and Pierre Curie as well as Mildred and Gene Dresselhaus. **Dirk** and **Mafalda**, are at the same level of intelligence and it is a problem of the academic world that is not able to keep them. Guys thank you for helping me with operating the dilution-fridge, as well as assisting me in measurements and problems of scientific nature. Special thanks for sharing the apartment and your cat with us. Enjoy life outside academia!

In the beginning I was introducing myself as the new **Michele** so people could understand the projects that I was working. Michele is only one, and if you do not know, he started the 2D magic in the M.E.D department along with Andres Castellanos-Gomez. Michele thank you for the suggestions and the papers in the beginning. Some of my publications and the ideas happened thanks to you. I am happy that you came back to Delft and that we interacted even more now, at the end of my Ph.D.

Andres thank you for welcoming me in your new lab in Madrid. I was amazed with

what we managed to do in such a sort time with limited resources. You have the ability to get things done anywhere with any amount of resources.

Srijit introduced me the van der Waals pick-up technique and helped a lot with the fabrication and the physics of 2D materials. Thank for all these years and I am very happy that I join your new lab for a short period.

The guy even turned brewing beer into a scientific experiment. **Pascal** thank you for assisting me with the physics of quantum dots, for performing experiments together and 'testing' beers. I really hope that someday you will become a group leader and explore science cause this makes you happy. You have skills and charisma to help others. Actually you remind me a bit of Gary...

I wish that in the end we turn out to be distant cousins from the Ottoman period. **Emre**, thank you first of all for hosting us and showing us around in Boston. I am proud of you and I will tell to my kid about his 'uncle' in Harvard University. Also, thank you for your advises on the papers, work and life. Finally thank you for providing material and inspiration for your defense-song that became our top-hit. Be kind to the mice and to yourself.

Is this thesis part of a bigger plan? Maybe; Who knows...**Santiago**, thank you for your unconventional way of thinking and your bold attitude towards authority. You are a true entrepreneur. Thank you for organizing journal clubs and the graphene lunch. Also, thank you for the parties, dinners and the amazingly funny conversations.

For the last two years something is missing in the QN corridors. We are becoming doctors of philosophy but philosophical discussions have been reduced around here. **Rocco** the Gaudenzi the dottore, the lover of philosophy and initiator of long conversations that change people's perspectives and sometimes even days. Even acknowledgments in the thesis have been transformed after him...Rocco thank you for the good times and for showing us how original ideas can result in great scientific papers. I am happy that you followed your dream with the postdoc and that you are starting a family.

People envy him because he is the most talented among us. From playing guitar, piano and violin to coding experimental setups, volleyball and partying like no one else. **Giordano** thank you for all the good moments that we shared in the M.E.D. Thank you for the music, the codes, advises and the games. Somehow people were staying late at work and had more fun back then and you had a role in that. It could be my nostalgia. Kyoto is lucky to have you.

During my Ph.D I worked in a few setups but in the beginning the person who gave most of the introduction to the setups and suffered my impatience and my sloppiness was **Vera**. Thank you for the patience and being meticulous with showing me things in the beginning. I am happy that we were under the same 'umbrella' of 2D materials and that you helped with some many things. I wish you the success in the rest of your Ph.D.

I was afraid that Italians around M.E.D became extinct. Luckily there is always an Italian physicist in some lab. He is the new generation and also talented with great experimental skills (especially on fixing bicycles). **Iacopo** thank you for the conversations about NV centers and teaching us about the cool stuff that your new lab is about to do. Also thank you for teaching the newcomers about beers at Teeepeee cafe and making the QN more fun.

I had the pleasure to have a good office-mate the last years that is very meticulous,

precise and fun to be around him. Felix thank you for the good moments in the office, the discussions on the JJs and the dinners. Good luck with your last year! I also want to thank my other nice office-mates **Lorenzo**, **Su-huyn**, **Igor** and lastly **Magda**.

Joeri thank you for the good moments and having also you there sharing IPAs, discussions and electronic music enthusiasm. Thank you also for the beautiful *Python* script for plots. Good luck in Copenhagen!

Marc I will miss your contagious laugh! You amaze me how well you understand things. Thank you for the beers and the discussions.

Nandini thank you for the wonderful conversations, the opportunity to visit your home country and attend your amazing wedding, for your great cooking skills. I am happy you were part of MED, but to be honest I am happy that we became closer after that. I enjoyed working along with you, you surprised me how fast you became skilled with the exfoliation (h-BN!). I admire your persistence and I am very proud that even after a difficult period in your Ph.D. you found a way to use your love for science in a different field and managed to thrive in it.

Yildiz thank you our discussions and bringing my spirits up, as well as for any help. You have a great way around people. You brought a vibe from the south that was missing.

Thierry thank your for the help with Frosti, I hope that it will work again and that you will do great experiments in the future. **Alexandra** thank you for advises related to work (fridge, magnet, fabrication etc). **Martin** and **Makars**. Other people take time to realize what is a Ph.D. but for you, it came natural. Thank you for the contribution on the new crystals, PDMS stamps, photoluminescence measurements. You will do great, enjoy it. **Mikael** we did not overlap a lot, but I am happy for the few months that we were together in the lab. I miss your positive and fun attitude, as well as your wooden toys. **Sabina** thank for the discussions on the boron nitride. **Maria** thank you for the chocolate, the funny discussions and the tips about Basel and academia!

Brecht thank you for the Dutch translations and for all the good times.

I want to acknowledge Yaroslav that helped me with discussions on many scientific topics that concern this thesis (weak localization, Efros-Shklovskii model and Coulomb blockade). I want to thank the P.Is: **Andrea, Sonia, Sander, Simon, Teun, Toeno, Kobus, Jian-Rong, Akira, Yuli and Anton**, for creating a great environment in the QN department, as well as in the group meetings.

During this Ph.D. I had great technical support: Special thanks to **Tino** for being crazy and answering to my requests with beautiful designs. Also, thanks to Ronald and **Mascha** for making our requests possible. **Allard** thank you for the help with the AFMs. I want to thank the clean room staff: **Ewan, Charles, Marko, Marc, Anja, Arnold, Eugene, Ruff and Pauline**. I should also acknowledge staff from Qutech that helped me a lot by providing helium and equipment **Remco, Marc and Raymond**. I want to thank our wonderful office support: **Etty, Maria, Dorine, Marije, Marijke, Erika and Heleen**.

I want to thank old and young students and people in the department who helped having a nice atmosphere: **Nicola, Joris, Robin, Julien, Anastasia, Irina, Thomas** (thanks for the borrels!), **Gaurav, Joao, Richard, Andreas, Stephanie, Rasa, Luigi, Miguel, Marteen, Klaus** (thank you for introducing me to yoga). I want to thank my very good friend **Leonardo Vicarrelli** for making me his para-nymph and showing me the lovely Pisa. The Steele-lab gang: **Martijn, Mario, Marios, Hadi, Christian, Sarwan, Byoung-moo,**

Daniel, Ines and Fatemeh. Also, people from my second-but-feels-like-first, the Zant-Lab: Damien, Alfredo, Davide, Diana, Ignacio.

I want to thank the clean room manufacturers **Bruno, Nodar, Moritz, David Thoen, Iman, Willemijn, David and others** for helping me with recipes and answering to my questions in the clean room.

Lastly, i want to thank my **family**. I want to thank my **parents** that supported me though all my academic years and helped me reach this point in my career, avoiding (major) bad decisions that would have otherwise changed the course of my life. Special thanks to the most important person in my life, my lovely wife **Andrea, Hajdi, Agapoula** for her support all these years. You motivated me to become a better person and scientist. You helped me keep a balance with work and life and created a home for us. Without you none of this would be possible, and if it would, it wouldn't matter that much.

8

CURRICULUM VITÆ

Nikos PAPADOPOULOS

03-09-1987   Born in Thessaloniki, Greece.

EDUCATION

2002–2005   High School
             1st High School, Alexandria, Greece

2005–2013   B.Sc. in Physics
             Aristotle University, Thessaloniki Greece
Thesis: Raman spectroscopy of graphene grown with chemical
             vapor deposition on copper substrates
Supervisor: Dr. J. Arvanitidis

2013–2015   M.Sc. in Materials Physics and Technology
             Aristotle University, Thessaloniki Greece
Thesis: Raman spectroscopic studies of alkali metal fullerides
Supervisor: Dr. J. Arvanitidis

2015–2019   Ph.D. in Physics
             Delft University of Technology
             Delft, The Netherlands
Thesis: Mesoscopic transport in 2D materials and heterostructures
Promotors: Prof. Dr. H. S. J. van der Zant and Prof. Dr. G. A. Steele

LIST OF PUBLICATIONS

10. **N. Papadopoulos**, , K. Watanabe, T. Taniguchi, H. S. J. van der Zant, G. A. Steele, *Landau level spectroscopy of h-BN/WSe$_2$/graphene/h-BN/graphite/h-BN tunneling van der Waals heterostructures*, in preparation.

9. **N. Papadopoulos**, P. Gehring, K. Watanabe, T. Taniguchi, H. S. J. van der Zant, G. A. Steele, *Tunneling spectroscopy of localized states of WS$_2$ barriers in vertical van der Waals heterostructures*, in preparation.

8. R. Frisenda, **N. Papadopoulos** et al., *Symmetry breakdown in franckeite: spontaneous strain, rippling and interlayer moiré pattern*, in preparation.

7. **N. Papadopoulos**, E. Flores, K. Watanabe, T. Taniguchi, J. R. Ares, C. Sánchez, I. J. Ferrer, A. Castellanos-Gomez, G. A. Steele, H. S. J. van der Zant, *Multi-terminal electronic transport in boron nitride encapsulated TiS$_3$ nanosheets*, ACS Nano, under peer review.

6. F. Ghasemi, R. Frisenda, E. Flores, **N. Papadopoulos**, R. Biele, D. Perez de Lara, H. S. J. van der Zant, K. Watanabe, T. Taniguchi, R. D'Agosta, J. R. Ares, C. Sánchez, I. J. Ferrer, A. Castellanos-Gomez, *Tunable photodetectors via in situ thermal conversion of TiS$_3$ to TiO$_2$*, ACS Applied Materials and Interfaces, under peer review.

5. **N. Papadopoulos**, K. Watanabe, T. Taniguchi, H. S. J. van der Zant, G. A Steele, *Weak localization in boron nitride encapsulated bilayer MoS$_2$*, Physical Review B **99**, 115414 (2019).

4. **N. Papadopoulos**, J. O. Island, H. S. J. van der Zant, G. A. Steele, *Investigating Laser-Induced Phase Engineering in MoS$_2$ Transistors*, IEEE Transactions on Electron Devices **65**, 4053-4058 (2018).

3. **N. Papadopoulos**, R. Frisenda, R. Biele, E. Flores, J. R. Ares, C. Sánchez, H. S. J. van der Zant, I. J Ferrer, R. D'Agosta, A. Castellanos-Gomez, *Large birefringence and linear dichroism in TiS$_3$ nanosheets*, Nanoscale **10**, 14424-14429 (2018).

2. **N. Papadopoulos**, G. A. Steele, H. S. J. van der Zant, *Efros-Shklovskii variable range hopping and nonlinear transport in 1T/1T′-MoS$_2$*, Physical Review B **96**, 235436 (2017).

1. K. Filintoglou, **N. Papadopoulos**, J. Arvanitidis, D. Christofilos, O. Frank, M. Kalbac, J. Parthenios, G. Kalosakas, C. Galiotis, K. Papagelis, *Raman spectroscopy of graphene at high pressure: Effects of the substrate and the pressure transmitting media*, Physical Review B **88**, 045418 (2013).